UNIVERSITY OF CALIFORNIA, SAN DIEGO

Development and Application of Ocean Color Algorithms for Estimating Particulate Organic Carbon in the Southern Ocean from Satellite Observations

A dissertation submitted in partial satisfaction of the requirements for the degree Doctor of Philosophy

in

Oceanography

by

David Benjamin Allison

Committee in charge:

Dariusz Stramski, Chair
Sarah T. Gille
Ralph F. Keeling
B. Gregory Mitchell
Kimberly A. Prather

2010

The Dissertation of David Benjamin Allison is approved, and it is acceptable in quality and form for the publication on microfilm and electronically.

Chair

University of California, San Diego

2010

DEDICATION

Dedicated to Jen.

Dedicated to Jax.

Dedicated to Deanna.

Dedicated to *Mountain Dew*.

TABLE OF CONTENTS

LIST OF FIGURES

LIST OF TABLES

ACKNOWLEDGEMENTS

I would like to thank the committee members, each of whom played a key role in seeing me through this process.

Chapter 1, in full, has been submitted for publication as it may appear in *Journal of Geophysical Research, Oceans* 2010, Allison, David B., Stramski, Dariusz, Mitchell, B. Greg. The dissertation author was the primary investigator and author of this paper.

Chapter 3, in full, is a reprint of material as it appears in *Journal of Geophysical Research*, 115, C06002, doi:10.1029/2009JC005347, Allison, David B., Stramski, Dariusz, Mitchell, B. Greg. The dissertation author was the primary investigator and author of this paper.

VITA

1998	Bachelor of Science, San Diego State University
2001	Master of Science, San Diego State University
2010	Doctor of Philosophy, University of California, San Diego

PUBLICATIONS

Moreno, Ignacio, J. A. Davis, K. G. D'Nelly, and D. B. Allison (1998), Transmission and phase measurement for polarization eigenvectors in twisted-nematic liquid crystal spatial light modulators. *Optical Engineering*, 37, 3048.

Davis, Jeffrey A., D. B. Allison, K. G. D'Nelly, M. L. Wilson, and I. Moreno (1999), Ambiguities in measuring the physical parameters for twisted-nematic liquid crystal spatial light modulators. *Optical Engineering*, 38, 705.

Stramska, M., D. Stramski, S. Kaczmarek, D. B. Allison, and J. Schwarz (2006), Seasonal and regional differentiation of bio-optical properties within the north polar Atlantic. *J. Geophys. Res*, 111, C08003, doi:10.1029/2005JC003293.

Allison, D. B., D. Stramski, and B. G. Mitchell (2010), Seasonal and interannual variability of particulate organic carbon within the Southern Ocean from satellite ocean color observations, *J. Geophys. Res*., 115, C06002, doi:10.1029/2009JC005347.

FIELDS OF STUDY

Major Field: Oceanography

ABSTRACT OF THE DISSERTATION

Development and Application of Ocean Color Algorithms for Estimating Particulate Organic Carbon in the Southern Ocean from Satellite Observations

by

David Benjamin Allison

Doctor of Philosophy in Oceanography

University of California, San Diego, 2010

Professor Dariusz Stramski, Chair

Empirical algorithms have been developed for estimating surface concentration of particulate organic carbon (POC) from remotely-sensed ocean color in the Southern Ocean using field data POC, spectral remote-sensing reflectance, $R_{rs}(\lambda)$, and the inherent optical properties (IOPs) of seawater. Several algorithm formulations have been considered. The best algorithm performance was obtained for the power function fit POC (mg m^{-3}) = 189.29 $[R_{rs}(443)/R_{rs}(555)]^{-0.87}$ with mean bias of 3%, normalized mean square error 7%, and determination coefficient 0.93. Analysis of match-up

comparisons between satellite-derived and *in situ* POC support application of this algorithm in the Southern Ocean.

The bio-optical relationships on which the POC algorithms are based exhibit significant variability mainly due to differing particulate assemblages. To quantify the sources of this variability, Mie scattering modeling and empirical data were used to calculate IOPs, POC, and chlorophyll-*a* content for 21 representative classes of particles. These classes represent colloids, organic detritus, minerals, and various plankton species. By using this reductionist approach, 38 different bulk models of seawater were constructed and analyzed. The utility of this approach in advancing an understanding of variability in the POC algorithms is shown; for example, the relationship between POC and particulate backscattering is investigated.

The POC retrieval algorithm based on the reflectance band ratio was applied to SeaWiFS satellite data to demonstrate seasonal and interannual variability in POC in the Southern Ocean (south of 35^{o}S) from 1997 through 2007. Typically the surface POC concentrations range from 30 to 120 mg m^{-3} while the monthly means range from 70-80 mg m^{-3}. The seasonal maximum stock of POC (0.6 Pg) integrated within the top 100 m of the ocean occurs in December. The seasonal range of area-normalized POC is 5.5 - 6.6 g m^{-2}. The region south of 55^{o}S provides a dominant contribution to the accumulation of POC during the productive period of the season. During the austral spring, the area-normalized POC accumulates in these high-latitude waters at rates from about 0.2 to 0.7 g m^{-2} month^{-1}. The comparison of these rates with large-scale satellite-based estimates of net primary production indicates that only a small fraction (<10%) of production accumulates as POC.

Introduction

The global climate pattern is a complex system dependant on processes ranging from solar heating to concentrations of atmospheric gases. Current concern about the increased injection and levels of the greenhouse gas carbon dioxide (CO_2) into the atmosphere necessitates an understanding of the global carbon cycle and budget. The oceans are a source and sink of carbon in the form of dissolved gases and suspended particles. Estimates of global carbon reservoirs and fluxes have been compiled most recently by *Houghton* [2007], who attempted to separate the natural and anthropogenic reservoirs and fluxes between the oceans, atmosphere, and land.

The current estimate of atmospheric carbon in the form of CO_2 is about 780 PgC [*Houghton,* 2007]. Oceanic carbon can be divided into: Dissolved Inorganic Carbon (DIC) occurring mainly as bicarbonate HCO_3^-; Dissolved Organic Carbon (DOC) which contributes to Color Dissolved Organic Matter (CDOM); and Particulate Organic Carbon (POC) occurring in marine biota. The total reservoir of carbon in the ocean is about 38,000 PgC with the majority occurring in the intermediate and deep waters at 36,300 PgC for DIC and 975 PgC for DOC [*Houghton,* 2007]. The surface ocean contains 25 PgC DIC, 700 PgC DOC, and only 3 PgC as POC [*Houghton,* 2007]. The large difference (~50x) in total carbon between the atmosphere and ocean is due to the chemical buffering of CO_2 by the chemistry of seawater. Less than 1% of the DIC in the ocean is dissolved CO_2 [*Siegenthaler and Sarmiento,* 1993].

The flux of carbon between the surface ocean and the atmosphere is controlled by the physical processes of air-sea gas exchange. This process depends upon the gradient of CO_2 partial pressures (ρCO_2) between the ocean and atmosphere and is largely a function of chemical processes within the ocean, although episodic biological events can draw down surface CO_2 concentrations. This input flux from the atmosphere (~92 PgC $year^{-1}$) is approximately balanced by ventilation of CO_2 to the atmosphere (~90 PgC $year^{-1}$) [*Houghton,* 2007]. The turnover time for inorganic carbon in the surface ocean is on the order of 10 years.

In the euphotic zone of the ocean (the upper 100-150 m), photosynthetic primary producers (phytoplankton) convert dissolved carbon to organic matter that is stored in POC (living and detrital particles) and DOC. Collectively, photosynthetic phytoplankton in the ocean account for about 40% of the total carbon fixed per year (Net Primary Production, NPP) on Earth. The transport of POC from the surface ocean via sinking is part of the biological pump, which provides a mechanism for the transport of carbon to intermediate and deep waters as well as to bottom sediments. Estimates of the rates of primary production and respiration among living organisms in the surface ocean are ~48 PgC $year^{-1}$ and ~37 PgC $year^{-1}$ with the excess (~11 PgC $year^{-1}$) being transported to the deep ocean as detritus (POC) [*Houghton,* 2007]. The removal of POC from surface waters to deep waters effectively removes carbon from the air-sea system for time scales on the order of the turnover time of the deep oceans, about 3000-4000 years. In steady state this falling POC is recycled at depth into DOC and transported back to surface waters via upwelling events. Burial of carbon within the sediments (~0.01 PgC $year^{-1}$) removes carbon for even longer periods but is

episodic and limited to coastal margins [*Houghton,* 2007]. The magnitude of the POC reservoir in the surface oceans is small, about 3 PgC, compared to other carbon reservoirs, but it has been estimated that without the biological pump atmospheric CO_2 would be significantly higher.

The Southern Ocean is one of the most productive oceanographic regions and accounts for 20% of the total ocean area on Earth. During the peak of the austral summer (December-February), primary production can fix over 1gC m^{-2} day^{-1}. It has been proposed that the biological pump is only at 50% of its maximum efficiency with respect to the potential sequestration of CO_2 in the Southern Ocean [*Falkowski et al*, 1998]. In addition, large areas of the Southern Ocean do not utilize all of the available macronutrients such as nitrogen and lead to so-called High Nutrient Low Chlorophyll (HNLC) areas. A leading hypothesis for this lack of utilization is iron limitation, supported by recent field work such as the SOFEX cruises. Climate models suggest that global warming will increase the transport of aeolian dust to this region, which could increase the utilization of these macronutrients and affect the biological pump.

Understanding and monitoring the current POC reservoirs and fluxes is important for predicting future levels of carbon both in the oceans and the atmosphere. Satellite remote sensing provides an effective and powerful way to monitor such a large range of spatial and temporal scales inaccessible by traditional oceanographic means, especially in large remote areas such as the Southern Ocean. Therefore, development, validation, and application of algorithms to estimate POC dynamics from satellite observations across the oceanic basin on annual and interannual time scales is of primary importance and is the topic of this dissertation.

The dissertation is organized into three chapters addressing each of the tasks behind a successful POC algorithm. The first chapter details the development and validation of a satellite POC algorithm from empirical relationships derived from *in situ* data. The second chapter investigates the natural variability seen in the empirical relationships by employing a reductionist model of the fundamental optical and biochemical constituents. Finally, the third chapter applies the newly developed POC algorithm to satellite data for the Southern Ocean to analyze the temporal and spatial variability in the surface POC for 10 years from 1997-2007. Each of these chapters is organized as stand-alone work with a complete introduction, body of work, and conclusions.

The concentration of chlorophyll-*a*, the primary pigment in phytoplankton, has been the basic remote-sensing data product derived routinely since the first satellite ocean color mission in 1970s, yet it is carbon, not chlorophyll, which is typically of greatest interest to the study of biogeochemical cycles. Empirical POC algorithms are developed because other, more advanced approaches such as semi-analytical inversions of ocean color have not yet proven to provide more reliable results or perform consistently better than the simple empirical approaches. The amount of simultaneously-collected field data of POC and optical quantities, especially ocean reflectance, which are required for the development of empirical algorithms, is very limited. In contrast, relatively large amounts of field data have been collected over the years to allow the development of empirical chlorophyll algorithms. As part of the research focus of this dissertation, field data were collected in the Southern Ocean to bolster existing databases. With these data, in Chapter 1, several formulations of

algorithm were developed that utilize wavebands available on current satellite ocean color sensors, in particular SeaWiFS (Sea-viewing Wide Field-of view Sensor). The algorithms were then evaluated using a match-up data set consisting of field data obtained under sunny conditions in conjunction with coincident satellite observations with SeaWiFS. In addition to the data used in the development of the algorithm, ancillary data were investigated to provide insights into the sources of variability in the algorithms. These data included the inherent optical properties (IOPs) of seawater, specifically the backscattering and absorption coefficients of particulate and dissolved components of water, which were collected in parallel to reflectance and POC measurements. These investigations naturally led to the topic for the next chapter in this dissertation, the modeling of the empirical relationships behind the POC algorithm with a reductionist approach to provide a more rigorous understanding of the biochemical and optical relationships.

The bio-optical relationships, including those forming a basis of ocean color remote sensing algorithms, are known to exhibit significant regional and temporal variability in the ocean. This variability and its limited understanding have been a major obstacle for achieving consistently good performance of remote sensing algorithms. A major source of such variability is thought to be associated with variations in particulate assemblages, both in composition and relative abundances of various particle classes. Unfortunately, the present understanding of how different particle classes contribute to bulk concentrations of seawater constituents such as POC and to bulk ocean optical properties is very limited. This is because the natural particulate assemblages have been traditionally described in terms of a few broadly

defined classes such as phytoplankton and non-phytoplankton particles. This traditional description is a great oversimplification of reality.

In Chapter 2 a reductionist approach [*Stramski et al*., 2001; 2004] is applied to assist in advancing the understanding of bio-optical relationships in terms of the detailed composition of particulate assemblages. Priority is placed on the bio-optical relationships involving POC and inherent optical properties of seawater. The research considers 21 classes of particles found in ocean waters which cover the size range from 0.015 μm to 200 μm, such as colloids, heterotrophic bacteria, organic detritus, mineral particles, and several groups of phytoplankton from picoplankton through microplankton size range. The particle classes were defined to reflect their potentially distinctive optical and biochemical roles in the ocean. Optical and biochemical properties were determined via Mie modeling and empirical relationships for each particle class. Representative bulk models of mixtures of particle classes, 38 in total, were created by assigning total particle counts for each particle class based on particle counts observed in the ocean. Bulk optical and biochemical properties were then calculated for each model and compared against field measurements from the Southern Ocean to gain insight into particle class contribution to observed bulk properties in the region of primary interest to this study.

In Chapter 3 the best performing POC algorithm based on the reflectance band ratio was applied to SeaWiFS data to examine the seasonal and interannual variability in POC within the surface waters of the Southern Ocean during a period from September 1997 through December 2007. Monthly composite maps of the surface POC concentration for the entire Southern Ocean (south of 35°S) were generated.

Estimates of the monthly average standing stock of POC and the water column integrated stock of POC for the regions within the Southern Ocean were calculated. Finally, the temporal standing stock of POC and the month-to-month change in POC were analyzed for regions within the Southern Ocean. The analysis of these satellite-derived results shows the significance of the application of remote sensing of POC to advancing knowledge about the dynamics of this oceanic carbon pool and the potentially broader impact of this knowledge to the study of carbon cycle and budget.

References

Falkowski, P. G., R. T. Barber, V. Smetacek (1998), Biogeochemical Controls and Feedbacks on Ocean Primary Production, *Science*, 281, 200-206.

Houghton, R.A. 2007. Balancing the global carbon budget. *Annual Review of Earth and Planetary Sciences* 35:313-347.

Siegenthaler, U. & J. L. Sarmiento (1993), Atmospheric carbon dioxide and the ocean, *Nature*, 365, 119-125

Stramski, D., A. Bricaud, and A. Morel (2001), Modeling the inherent optical properties of the ocean based on the detailed composition of planktonic community, *Appl. Opt.*, *40*, 2929-2945.

Stramski, D., E. Boss, D. Bogucki, and K. J. Voss (2004), The role of seawater constituents in light backscattering in the ocean, *Prog. Oceanogr.*, 61, 27-56.

Chapter 1. Empirical Ocean Color Algorithms for Estimating Particulate Organic Carbon in the Southern Ocean

1.0. Abstract

We have examined empirical algorithms for estimating surface concentration of particulate organic carbon (POC) from remotely-sensed ocean color in the Southern Ocean using field data of POC, spectral remote-sensing reflectance, $R_{rs}(\lambda)$, and the inherent optical properties of seawater collected during a number of cruises. Several algorithm formulations have been considered, including direct relationships between POC and the blue-to-green band ratios of reflectance and a single wavelength two-step algorithm that consists of relationships linking reflectance to the backscattering coefficient and POC to the particulate backscattering coefficient at 555 nm. The best error statistics among the algorithms tested were obtained for the power function fit POC (in mg m^{-3}) = 189.29 $[R_{rs}(443)/R_{rs}(555)]^{-0.87}$. This simple band-ratio algorithm is based on 85 pairs of field data and shows a small mean bias of about 3%, the normalized mean square error of 27%, and the determination coefficient of 0.93. These error statistics as well as the analysis of match-up comparisons of satellite-derived POC and *in situ* POC determinations support the prospect for reasonably good performance of this algorithm in the Southern Ocean. The two-step empirical algorithm operating at 555 nm shows inferior error statistics of the regression fits and match-up comparisons compared with the band-ratio algorithm.

1.1. Introduction

One of the principal goals of optical remote sensing of ocean color is to enhance an understanding of ecosystem dynamics and biogeochemical cycles within the upper ocean, which has implications to understanding the ocean's role in climate change. Current satellite missions with ocean color capabilities, such as SeaWiFS (Sea-viewing Wide Field-of-View Sensor), MODIS (Moderate Resolution Imaging Spectroradiometer), and MERIS (Medium Resolution Imaging Spectrometer), have provided a means for routine observations of large-scale, global distributions of biogeochemically important oceanic processes and variables continuously over a number of years with a temporal resolution of the order of days. Future missions, if accomplished with sufficient quality of sensor performance and overlap with current missions, would provide highly desirable continuity of uninterrupted time series of ocean color data for ocean biogeochemistry and climate research.

The investigations utilizing satellite ocean color data contribute in many ways to understanding variability related to biological and biogeochemical processes, and efforts have recently increased to broaden the assortment of data products that can be derived from ocean color [see *Yoder and Kennelly*, 2006; *McClain*, 2008 for reviews]. Whereas the concentration of chlorophyll-*a*, the primary pigment in phytoplankton, has been the basic data product derived routinely since the first ocean color mission in 1970s, it is carbon, not chlorophyll, which is typically of greatest interest to the study of biogeochemical cycles. The particulate organic carbon (POC) in the upper ocean represents one of the carbon stocks of substantial interest. The particulate matter containing carbon plays, for example, a central role in oceanic biological pump [*Volk*

and Hoffert, 1985; *Longhurst and Harrison*, 1989] and carbon-based estimation of primary production [*Behrenfeld et al*., 2005]. The POC stock in the upper ocean is highly variable and its large-scale distributions and temporal variations are poorly characterized, however. This is primarily because conventional oceanographic sampling has been both temporally and spatially sparse.

Recent advances in algorithm development for estimating surface concentration of POC from satellite measurements of ocean color promise rapid expansion of information for understanding distributions and variability of this carbon pool in the surface ocean [*Stramski et al.*, 1999; *Loisel et al*., 2001; *Mishonov et al*., 2003; *Stramska and Stramski*, 2005; *Gardner et al*., 2006; *Pabi and Arrigo*, 2006; *Stramski et al*., 2008; *Son et al*., 2009; *Stramska*, 2009]. In this study our interest is focused on empirical algorithms because other, more advanced approaches such as semi-analytical inversions of ocean color have not yet proven to provide more reliable results or perform consistently better than the simple empirical approaches. The amount of simultaneously collected field data of POC and optical quantities, especially ocean reflectance, which are required for the development of empirical algorithms is, however, still very limited. A small number of studies exist in which such adequate data sets, albeit of limited size, were used for the POC algorithm development [*Stramski et al.*, 1999; *Stramska and Stramski*, 2005; *Pabi and Arrigo*, 2006; *Stramski et al*., 2008]. This situation remains in contrast with relatively large amounts of field data, which have been collected over the years to allow the development of empirical chlorophyll algorithms [e.g., *O'Reilly et al.,* 1998; 2000].

In addition to the limitation of the amount of field data available for the POC algorithm development, the geographic coverage of these data has also been restricted. It is generally known that the performance of ocean color algorithms can be better if algorithms are established and applied on a regional basis, compared with the performance of a single algorithm applied indiscriminately to the entire global ocean. Several studies proposed the partitioning of the world's oceans into provinces based on criteria involving bio-optical properties *[Platt and Sathyendranath*, 1988; *Mueller and Lange*, 1989; *Esaias et al*., 2000; *Hooker et al*., 2000]. An important case of regional differences in bio-optical relationships was suggested by comparisons of polar waters and lower latitudes [*Mitchell and Holm-Hansen*, 1991; *Mitchell*, 1992; *Dierssen and Smith*, 2000; *Sathyendranath et al*., 2001]. The extent to which these differences are significant remains, however, an open question [*Marrari et al*., 2006]. Therefore, the collection and analysis of new datasets consisting of simultaneous field measurements of POC and optical variables from various marine environments, including polar regions that have been largely under sampled in the past, are of vital importance for improving the capability to estimate POC from ocean color.

In this study we use field data collected on several cruises in the Southern Ocean to develop empirical algorithms that relate surface concentration of POC to remote-sensing reflectance, R_{rs}, within the Southern Ocean. Our specific objectives are to explore several formulations of algorithm, which utilize wavebands available on current satellite ocean color sensors, in particular SeaWiFS, and to evaluate the algorithms using a match-up data set consisting of field data obtained under sunny conditions in conjunction with coincident satellite observations with SeaWiFS. One

of the algorithms based on the blue-to-green band ratio of reflectance was recently applied to satellite observations of the Southern Ocean over a 10-year period, which demonstrates the broader significance of remote sensing of POC for ocean biogeochemistry [*Allison et al*., 2010]. For providing insights into the sources of variability in the band-ratio algorithms, in this study we also analyze the field data of the inherent optical properties (IOPs) of seawater, specifically the backscattering and absorption coefficients of particulate and dissolved components of water, which were collected in parallel to reflectance and POC measurements.

1.2. Methods and Data

1.2.1. Field Measurements for Algorithm Development and Validation

Optical and POC measurements were made during several oceanographic cruises within three regions of the Southern Ocean; in the waters near Antarctic Peninsula and South Shetland Islands, the Antarctic Polar Frontal Zone (PFZ) within the Pacific sector, and the Ross Sea (Figure 1.1). The stations were located in high-latitude waters south of 50°S, and most stations were south of 60°S. For the POC algorithm development, field data from six cruises spanning a time period from 1997 through 2006 are used. These cruises include: (i) the U.S. Joint Global Ocean Flux Study (JGOFS) cruise NBP9711 in the Ross Sea in November-December of 1997 (we use a symbol NBP97 for data from this cruise); (ii) two JGOFS cruises REV9801 and REV9802 in the PFZ region which took place from January through March 1998 (symbol for data REV98); (iii) two cruises under the NOAA Fisheries' U.S. Antarctic Marine Living Resources (AMLR) Program in the region of South Shetland Islands

and Antarctic Peninsula during the January-March period in 2004 and 2006 (symbols AMLR04 and AMLR06); and (iv) one cruise sponsored by National Science Foundation during the 2004 AMLR season (symbol for data LMG04). During each cruise vertical profiles of optical data were collected from several instruments either mounted on the ship's CTD/rosette system for simultaneous *in situ* measurements with discrete water sampling or deployed shortly before or after the CTD/rosette cast. These deployments of the CTD/rosette and optical instruments constitute a common station. Data collected at the common station are considered "coincident in time and space" for the purposes of development of the POC algorithms. We restrict the algorithm development to the use of POC and optical data collected at near-surface depths (< 10 m) within open water stations where it is reasonable to assume that optical properties and suspended particles are dominated by plankton microorganisms and plankton-derived organic matter. In bio-optical studies such waters have been customarily referred to as Case 1 waters [Morel and Prieur, 1977; Gordon and Morel, 1983].

For the validation of the algorithms by means of match-up comparisons of coincident satellite and *in situ* data (see section 1.2.5 for methodological details), we use field data from AMLR cruises in 2000, 2001, 2002, and 2007, in addition to field data from the six cruises listed above. The AMLR cruise in 2007 provided only one match-up data point, however. These four additional AMLR cruises that were not used in the algorithm development provide about 40% of data for our match-up comparisons of remote-sensing reflectances and 50% of data for the match-up comparisons of POC.

1.2.2. *In situ* Radiometric Measurements

Measurements of spectral downwelling irradiance, Ed(z, λ), and upwelling radiance in the nadir direction, $L_u(z, \lambda)$ (where z is depth and λ light wavelength *in vacuo*), were made within the upper water column with several calibrated radiometers (Biospherical Instruments, Inc.) at a number of wavebands in the visible and ultraviolet spectral regions. The radiometric measurements and data processing were consistent with methods recommended in NASA protocols [*Mueller et al*., 2003] and more detailed description of our measurements is given in *Allison et al*. [in press]. The final data product from these measurements used in this study is the spectral remote sensing-reflectance defined as $R_{rs}(\lambda) = L_w(\lambda)/E_s(\lambda)$, where $L_w(\lambda)$ is the water-leaving radiance from the nadir direction just above the water surface and $E_s(\lambda)$ is the downwelling plane irradiance incident on the surface. For the purposes of POC algorithm development, our interest in this study is focused on the $R_{rs}(\lambda)$ values from the blue and green spectral regions.

1.2.3. POC Determinations

For the determinations of POC concentration, water samples obtained from CTD/rosette casts were filtered onto precombusted 25-mm Whatman glass-fiber filters (GF/F). Our procedure is detailed in *Allison et al*. [2010] and POC was determined by high temperature combustion of sample filters *via* standard CHN analysis [*Parsons et al*., 1984; *Knap et al*., 1996]. For the development of the POC algorithms in this study, we only consider data collected at near-surface depths (< 10 m).

1.2.4. Measurements of the Inherent Optical Properties (IOPs) of Seawater

The spectral backscattering coefficient, $b_b(z, \lambda)$ was determined from *in situ* measurements with one of several Hydroscat-6 sensors (HobiLabs, Inc.), each with six wavebands in the visible range from 440 to 676 nm. For vertical profiling, the Hydroscat-6 instrument was mounted on an optical package and lowered by the ship's winch. Data were processed with a method described originally by *Maffione and Dana* [1997] with refinements presented in *Boss and Pegau* [2001]. Those and some additional refinements used in processing of our data are described in *Stramski et al*. [2008]. However, because there is no single widely accepted protocol for processing backscattering data, we here provide some details. The coefficient b_b is considered to be the sum of contributions from pure water backscattering, b_{bw}, and particle backscattering, $b_{bp,}$ and the pure water scattering values are required as input for data processing. Theoretical estimates of pure water scattering available in the literature show some differences [*Morel*, 1974; *Shifrin*, 1988; *Buiteveld et al*., 1994]. We applied the values calculated from the formulas described in *Buiteveld et al*. [1994], which was recently recommended by *Twardowski et al*. [2007]. These original formulas allow the scattering calculations as a function of water temperature T at salinity $S = 0$, but the adjustment for seawater salinity can be made using the multiplicative factor of 1 + 0.3 S/37 [*Twardowski et al*., 2007]. We made such calculations for each station where our backscattering measurements were taken, using measured values of T and S. We note that processing of backscattering measurements with pure water values of *Buiteveld et al*. [1994] with salinity adjustment yields generally a lower percent contribution of b_{bw} and higher percent contribution of b_{bp} to

the total backscattering coefficient, b_b, when compared with the use of pure seawater scattering values of *Morel* [1974]. The latter values were usually used in the past in this type of data processing. These differences are discussed in some detail in *Twardowski et al*. [2007] and *Stramski et al*. [2008].

The processing of Hydroscat-6 data also involves the conversion of the particle volume scattering function measured with Hydroscat-6 at a backscattering angle centered at about 140^{o} to the particle backscattering coefficient. We used a value of 1.13 for the conversion parameter, χ [*Dana and Maffione*, 2002]. In addition, the so-called "sigma" correction of the backscattering coefficient was made with the beam attenuation data collected simultaneously (described below). This correction involved the use of a second-order polynomial function of the beam attenuation coefficient.

After calculation of the sigma-corrected backscattering coefficient, the profile data of $b_b(z, \lambda)$ were inspected for possible large anomalies and the questionable data were rejected. Then, the data were binned to 1 m intervals, and the up-casts and down-casts were averaged to create a single resultant vertical profile for the station. The near-surface data (at depths less than ~5 m) were usually discarded because of significant signal fluctuations at these shallow depths. Subsurface values of the backscattering coefficient (from below ~5 m) were extrapolated upwards to the surface to obtain valid data within the near-surface layer. For any depth z, our final $b_b(\lambda)$ values at Hydroscat-6 wavebands were used to fit a power function, $b_b(\lambda) \propto \lambda^{-\gamma}$, where γ is the spectral slope parameter of backscattering coefficient.

There are two main reasons for performing the power function fit. First, as the Hydroscat-6 wavebands do not necessarily coincide with the SeaWiFS wavebands,

this fit provides the $b_b(\lambda)$ values at wavelengths corresponding to nominal center wavelengths of SeaWiFS bands. Second, the use of the spectral fit offers an advantage of smoothing out potential positive and negative uncertainties in the measured data at individual spectral channels. These uncertainties may be associated with positive and negative biases in manufacturer's calibration at different spectral channels or dissimilar temporal drifts in the spectral calibration factors between the time of pre- or post-cruise calibration and actual measurements during the cruise. In addition, a power function may also smooth out some environmental effects such as the presence of relatively rare large particles that may occasionally affect one of the spectral channels, and not other channels, at a particular depth during the cast. We also note that the use of power function fit is reasonable under typical oceanic conditions because $b_b(\lambda)$ is expected to be generally a smooth function of λ. This is because in typical oceanic situations in the absence of intense phytoplankton blooms, $b_{bw}(\lambda)$ which itself is a power function of λ, makes large or dominant contribution to $b_b(\lambda)$.

The spectral beam attenuation coefficient of suspended particles, $c_p(z,\lambda)$, required for "sigma" correction of backscattering, was measured at two wavelengths (488 and 660 nm) with C-Star beam transmissometers (WetLabs, Inc) mounted either on the same optical package as the Hydroscat-6 or on the CTD/rosette system. The pure water calibration of beam attenuation data was made using the measurement of the clearest water encountered on a given cruise at depths of 250-300 m. The profiles of $c_p(z, \lambda)$ were processed with a similar method as the backscattering data for binning and determining the surface values. Also, for each depth z, the final $c_p(\lambda)$ values at C-

Star wavebands were used to fit a power function, $c_p(\lambda) \propto \lambda^{-\eta}$, where η is the spectral slope parameter of particulate beam attenuation. From this function, the $c_p(\lambda)$ values at wavelengths required for "sigma" correction of Hydroscat-6 data were obtained. Accurate measurements of beam attenuation at as little as two wavelengths were shown to provide a good basis for determinations at other wavelengths [*Boss et al*., 2001]. This approach was deemed satisfactory for "sigma" correction as the correction introduces only a small change (a maximum of a few percent) in the backscattering estimates for the examined waters.

The spectral particulate absorption coefficient, $a_p(\lambda)$, was measured with a filter-pad technique using a Varian Cary 1E, Varian Cary 100, or Perkin Elmer Lambda 18 spectrophotometer [*Mitchell et al*., 2002]. Discrete water samples were collected from CTD/rosette casts and filtered onto the 25-mm GF/F filters. The spectrophotometric measurements on the filters were made in the transmittance mode on freshly collected samples on board the ship. The data were acquired in the spectral range from 300 to 800 nm with a 1 nm interval and the correction for the pathlength amplification factor was made following *Mitchell* [1990]. After the $a_p(\lambda)$ measurement, the GF/F filter was treated with 100% methanol to remove phytoplankton pigments, and the spectrophotometric measurements were then taken on the "bleached" filters to determine the spectral absorption coefficient of non-algal (detrital) particles, $a_d(\lambda)$ [*Kishino et al*., 1985]. Assuming that the total particulate absorption, $a_p(\lambda)$, is the sum of the detrital absorption, $a_d(\lambda)$, and phytoplankton absorption, $a_{ph}(\lambda)$, the latter was calculated as $a_{ph}(\lambda) = a_p(\lambda) - a_d(\lambda)$.

Samples of seawater were also filtered through 0.2 μm Nuclepore filters. The filtrate was collected in acid-washed combusted glass bottles for analysis of the spectral absorption coefficient of soluble matter, $a_s(\lambda)$, also referred in the literature to as $a_{CDOM}(\lambda)$ where CDOM stands for the colored dissolved organic matter. The term "soluble" accounts for the fact that dissolved inorganic constituents, in addition to dissolved organic matter, may contribute considerably to absorption in the far ultraviolet [*Shifrin,* 1988]. The determinations of $a_s(\lambda)$ were made following the procedure described in *Mitchell et al*. [2002]. Briefly, the $a_s(\lambda)$ spectra between 250 and 750 nm were measured on board the ship with a spectrophotometer on freshly prepared samples of seawater filtrate (Nuclepore 0.2 μm pore size) in 10 cm quartz cuvettes. The $a_s(\lambda)$ spectra were corrected for an offset measured at 650 (±5) nm, which can be attributed mainly to scattering effects. The exponential fit was made to these $a_s(\lambda)$ spectra and a blank spectrum was subtracted from the exponential fit to achieve the final $a_s(\lambda)$ values. The blank spectrum was obtained from a measurement of standard purified deionized water (Milli-Q).

In this study we use only near-surface estimates of $b_b(\lambda)$, $b_{bp}(\lambda)$, $a_p(\lambda)$, $a_{ph}(\lambda)$, $a_d(\lambda)$, $a_s(\lambda)$, as well as the total absorption coefficient, $a(\lambda) = a_w(\lambda) + a_p(\lambda) + a_s(\lambda)$, for the blue and green spectral wavebands. The pure water absorption values, $a_w(\lambda)$, were taken from *Pope and Fry* [1997].

1.2.5. Satellite Data and Methodology for Algorithm Validation

To analyze the performance of the POC algorithms, the *in situ* data of reflectance and POC were compared to the closest satellite "match-ups". This match-up, as defined in more detail below, represents the closest spatial and temporal satellite and *in situ* data pair. For this analysis the Level 2 Merged Local Area Coverage (MLAC) and Global Area Coverage (GAC) standard SeaWiFS data products of normalized-water leaving radiance, $nL_w(\lambda)$, were obtained from the NASA Ocean Color Web (http://oceancolor.gsfc.nasa.gov /ftp.html) for the entire SeaWiFS mission to date (September 1997 through September 2009). These data result from SeaWiFS Reprocessing 5.2. Because our POC algorithm requires $R_{rs}(\lambda)$ as input, the values of satellite estimates of $nL_w(\lambda)$ were first converted to $R_{rs}(\lambda)$. This conversion was made using the relationship $R_{rs}(\lambda) = nL_w(\lambda) / F_o(\lambda)$, where $F_o(\lambda)$ is the extraterrestrial solar constant. The values of $F_o(\lambda)$ were taken from *Thuillier et al*. [2003]. After determining the satellite estimates of $R_{rs}(\lambda)$, the band-ratio and two-step single wavelength POC algorithms were applied to produce the satellite estimate for the POC match-up comparisons.

A match-up is defined as the closest spatial and temporal MLAC satellite pixel within a certain threshold to a given *in situ* measurement. Specifically, for each *in situ* measurement which occurs at a surveyed latitude and longitude location on a given date (see previous discussion on station criteria) the closest, non-flagged, satellite pixel was selected. If this pixel met the temporal constraint of +/- 6 hours and spatial constraint of +/- 4 km with respect to the time and location of *in situ* station, it was

considered a successful match-up. The surrounding *m* x *n* pixels were then selected to form a statistical representation of the satellite data. We evaluated 3 x 3, 5 x 5, and 9 x 9 boxes of pixels. It was determined that the 3x3 pixel ensemble represented the best aggregate selection. In our analysis, the satellite value for the match-up is then the average of all non-flagged pixels within the 3 x 3 collection. In addition to the +/- 6-hour temporal window, we also examined more restrictive temporal criteria. Whereas the use of the +/- 3-hour temporal window reduced the number of match-up data points, the resultant data patterns of match-up comparisons were not significantly different from those produced by the analysis with the +/- 6-hour temporal window. In our final dataset for match-up comparisons, the average time difference between the satellite and *in situ* measurements is in the range 2.45 - 2.50 hours, depending on whether we compare reflectances or POC. The standard deviation for this time difference is 1.54 - 1.61 hours, so the majority of our match-ups actually fall within +/- 4-hour window. We also note that our final match-up dataset includes data corresponding to the satellite viewing angle less than 58^{o} and the solar zenith angle less than 65^{o}. Although not identical, our match-up selection criteria are similar to those used in a recent study of global dataset by *Bailey and Werdell* [2006].

In addition to using the MLAC data for the match-ups, GAC data was also investigated. Because the resultant MLAC match-up was the average of the 3x3 pixels it can be argued that the GAC best pixel match-up could also be used because it represents a low-pass filtered version of the MLAC data with the filter being every 4th pixel. The benefit of using the GAC data is the true global availability of these data. For example, we found that the relationship between GAC best pixel and the MLAC

3x3 pixel average for the band-ratio $R_{rs}(443)/R_{rs}(555)$ is very good; a linear regression has a slope of 0.99 and the correlation coefficient $R = 0.98$. This result was obtained for 42 observations, which correspond to locations and times of our *in situ*-satellite reflectance match-ups, and suggests that the GAC data could be considered as adequate as the MLAC data for the match-up validation analysis. The results of match-up analysis presented in this paper in section 1.3.3 are, however, based on the standard approach utilizing MLAC data.

1.3. Results and Discussion

1.3.1. Reflectance Band-ratio Algorithms for POC

Our basic approach for developing POC algorithms utilizes empirical relationships between surface POC concentration and the blue-to-green (BG) band-ratio of remote-sensing reflectance, $R_{rs}(\lambda_B)/R_{rs}(555)$. The rationale for such relationships is similar to that used in the estimation of chlorophyll-*a* concentration from reflectance band-ratio algorithms. Variations in the BG reflectance ratio are expected to be driven largely by variations in the green-to-blue ratio of the absorption coefficient of seawater, which are in turn associated with variations in the particulate pool comprising all kinds of POC-containing particles, including phytoplankton, heterotrophic organisms, and organic detritus. All these particle types show higher absorption in the blue than in the green spectral region, so their effect on the BG reflectance ratio is qualitatively similar. The variations in the BG ratio as a function of POC concentration are expected to be fairly regular in most open ocean waters where organic matter is the dominant optical component of seawater and the different

types of organic particles exhibit a significant degree of covariation. Example illustration of characteristic variations in remote-sensing reflectance, $R_{rs}(\lambda)$, associated with differences in POC concentration is presented in Figure 1.2 using data from the Southern Ocean. The variation in $R_{rs}(\lambda)$ with increasing POC is much larger in the blue spectral region than in the green.

Figure 1.3 shows several versions of band-ratio algorithm obtained with our field data. We examined the following band ratios: $R_{rs}(443)/R_{rs}(555)$, $R_{rs}(490)/R_{rs}(555)$, $R_{rs}(510)/R_{rs}(555)$, and the maximum band ratio, *MBR*, that represents the largest of the three ratios considered. The ratio $R_{rs}(443)/R_{rs}(555)$ was most frequently the largest (55%) and $R_{rs}(510)/R_{rs}(555)$ was least frequently the largest (15%) amongst the three ratios considered. We tested two equations for relating POC with reflectance ratio; the power function and a function that has the form of the current Ocean Chlorophyll 4 (OC4) algorithm [*O'Reilly et al*., 2000]. These equations along with the best fit parameters and error statistics are given in Table 1.1. The formulas for calculating the error statistics are given in Table 1.2. We note that all regression analyses used in the development of POC algorithms in this study (Figures 1.3 and 1.7, Tables 1.1, 1.3, and 1.4) are based on the ordinary least squares Model I regression technique, which is suitable for the analysis of experimental data whose aim is to provide predictive relationships between two variables [*Sokal and Rohlf*, 1995]. We also note that the wavelengths of 443, 490, 510, and 555 nm used in our study are consistent with the wavebands of the satellite SeaWiFS sensor [*McClain et al*., 2004], and these bands are also currently used in the

NASA algorithm for estimating chlorophyll-*a* concentration in the global ocean [*O'Reilly et al.*, 1998; 2000].

Comparison of the error statistics in Table 1.1 suggests that the performance of the examined band-ratio algorithms will be quite similar. Some differences can be expected, however. The mean normalized bias, *MNB*, which characterizes the systematic error of the regression fit was found to be consistently lower for the simple power function fits compared with the OC4-like function fits. Example differences are shown in Table 1.1 for the algorithm based on *MBR*. The differences between the fits obtained with these two functions, albeit generally small, are also seen in Figure 1.3. Overall, for our data set the simple power functions of POC versus $R_{rs}(443)/R_{rs}(555)$ or POC vs. $R_{rs}(490)/R_{rs}(555)$ were found to have slightly better error statistics than the other functions tested. Our analysis suggests that the power function POC = 189.29 $[R_{rs}(443)/R_{rs}(555)]^{-0.870}$ is presently the best choice for the applications in the Southern Ocean. For our data set consisting of 85 measurements, this algorithm is characterized by *MNB* of about 3% and the normalized root mean square error, *NRMS*, of about 27%. This algorithm has been applied in our recent study of seasonal and interannual variability in POC within the Southern Ocean on the basis of a 10-year time series observations with SeaWiFS [*Allison et al*., 2010].

Our estimates of the best fit power functions show some differences when compared with similar analysis of POC and reflectance measurements in other oceanic regions [*Stramska and Stramski*, 2005; *Stramski et al*., 2008]. For example, the power function POC = 203.2 $[R_{rs}(443)/R_{rs}(555)]^{-1.034}$ was obtained with the field data from the tropical and subtropical waters of the eastern South Pacific and eastern Atlantic

Oceans [*Stramski et al.*, 2008]. The difference between the fitted parameters for this low latitude data set and the present Southern Ocean data set is large enough to suggest that some variability in the band-ratio algorithms can exist within the open waters of the global ocean. In particular, the 95% confidence intervals for the slope parameters for the two compared power function fits do not overlap. Whereas the question of the extent to which the regional differences in the open ocean are significant requires further studies, the greatest challenges are expected in coastal environments which generally are optically more complex than open ocean waters. In this study, we restricted the algorithm development to the use of surface POC and optical data from open water stations where it is reasonable to assume that optical properties and suspended particles are dominated by organic matter. Data from near-coastal stations visited on the AMLR cruises were excluded from our analysis due to potentially large input of terrigenous material. We also note that some data included in our analysis were collected during an intense bloom of *Phaeocystis antarctica* in the Ross Sea where POC was significantly higher than typical open water concentrations (see the NBP97 data points for POC > 800 mg m^{-3} in Figure 1.3).

The comprehensive suite of optical measurements taken on our cruises in the Southern Ocean allows us to provide insight on how the inherent optical properties (IOPs) of seawater drive the variations in the BG ratio of reflectance. Specifically, we analyze how the variations in different IOP components associated with particulate and soluble water constituents affect the variations in the BG reflectance ratio, which is ultimately used as a predictor of POC from remote-sensing algorithms. It is noteworthy that although a general relationship between the ocean reflectance and the

absorption and backscattering coefficients has long been recognized and the reflectance band-ratio algorithms have long been used in ocean color applications, the analysis of simultaneously collected field data of reflectance and the backscattering and absorption coefficients of particulate and soluble components, has been exceptionally rare within the context of such algorithms [*Reynolds et al*., 2001]. This type of analysis is significant for advancing quantitative understanding of the effects of the various component IOPs as the drivers of the main trend as well as the sources of common scatter of data points in the empirical band-ratio algorithms.

Radiative transfer modeling has shown that $R_{rs}(\lambda)$ is approximately proportional to the backscattering coefficient of seawater, $b_b(\lambda)$, and inversely proportional to the absorption coefficient of seawater, $a(\lambda)$ [e.g., *Gordon et al.,* 1975; *Gordon and Morel*, 1983; *Morel and Prieur*, 1977]:

$$R_{rs}(\lambda) \propto \frac{b_b(\lambda)}{a(\lambda)} \tag{1.1}$$

For the band ratio involving the blue waveband centered at λ_B and the green waveband centered at 555 nm, we obtain an approximate relationship:

$$\frac{R_{rs}(\lambda_B)}{R_{rs}(555)} \cong \frac{b_b(\lambda_B)}{b_b(555)} \frac{a(555)}{a(\lambda_B)} \tag{1.2}$$

where the factor of proportionality in Equation 1.1 is assumed to be the same for λ_B and 555 nm. This is a reasonable assumption for the purpose of our discussion. Using the additive property of IOPs we can partition the total absorption and backscattering coefficients of seawater into contributions associated with a few major classes of

water constituents, which are amenable to measurement or derivation from measurement:

$$a(\lambda) = a_w(\lambda) + a_s(\lambda) + a_{ph}(\lambda) + a_d(\lambda) \quad (1.3)$$

$$b_b(\lambda) = b_{bp}(\lambda) + b_{bw}(\lambda) \quad (1.4)$$

where the subscript *w* denotes pure seawater, *s* the soluble matter, *ph* the phytoplankton, and *d* the non-phytoplankton particulate matter (often referred to as detrital matter that generally includes contributions from organic detritus, minerogenic particles, and heterotrophic organisms). The total suspended particulate matter (*p*) is the sum of phytoplankton and detrital components (*ph*+*d*). Substituting this partitioning of IOPs into Equation 1.2 yields:

$$\frac{R_{rs}(\lambda_B)}{R_{rs}(555)} \cong \left[\frac{b_{bw}(\lambda_B) + b_{bp}(\lambda_B)}{b_{bw}(555) + b_{bp}(555)}\right]\left[\frac{a_w(555) + a_s(555) + a_{ph}(555) + a_d(555)}{a_w(\lambda_B) + a_s(\lambda_B) + a_{ph}(\lambda_B) + a_d(\lambda_B)}\right] \quad (1.5)$$

Having introduced these relationships, we will first look at the dependence of the reflectance band ratio on the total IOP coefficients using our field data from the Southern Ocean (Figure 1.4). For illustrative purposes, we choose λ_B = 443 nm but the consideration of other blue wavelengths would yield qualitatively similar results. As expected from Equation 1.2, the product [$b_b(443)/b_b(555)$] [$a(555)/a(443)$] is a good determinant of $R_{rs}(443)/R_{rs}(555)$. This is readily apparent as the data points in Figure 1.4a generally fall along the 1:1 line. Some scatter in the data around this line is understandable as, in addition to measurement uncertainties, Equation 1.1 is not an exact relationship with a constant factor of proportionality. Figure 1.4a supports the notion that the POC algorithm based on the relationship between POC and

$R_{rs}(443)/R_{rs}(555)$ is founded on the relationship between POC and the IOP ratio, $[b_b(443)/b_b(555)]$ $[a(555)/a(443)$.

Figure 1.4 also displays the band ratio $R_{rs}(443)/R_{rs}(555)$ vs. $b_b(443)/b_b(555)$ (Figure 1.4b) and $R_{rs}(443)/R_{rs}(555)$ vs. $a(555)/a(490)$ (Figure 1.4c). These data show that whereas $R_{rs}(443)/R_{rs}(555)$ varies 40-fold (from about 0.2 to over 7), the backscattering band ratio $b_b(443)/b_b(555)$ has weak variability, ~1.8-fold in the range from 1.25 to 2.25 (Figure 1.4b). In contrast, we see a relatively large >10-fold variation from about 0.3 to 3.3 in the absorption band ratio $a(555)/a(443)$ (Figure 1.4c). Thus the variation in the green-to-blue absorption ratio is the primary source for the variation in the blue-to-green band ratio of ocean reflectance in our data set. This result indicates that the ability to estimate POC from the blue-to-green band ratio of reflectance derives primarily from the relationship between POC and the green-to-blue ratio of total absorption coefficient.

Given the importance of the absorption coefficient, it is instructive to analyze the roles of particulate and soluble components of absorption. This analysis can be done by considering the relationships between $R_{rs}(443)/R_{rs}(555)$ and the absorption band ratio formed by either the particulate or soluble components present in seawater (Figure 1.5). This figure indicates that suspended particulate matter is a very important determinant of the relationship between $R_{rs}(443)/R_{rs}(555)$ and $a(555)/a(443)$, and hence a very important factor underlying the ability to estimate POC from $R_{rs}(443)/R_{rs}(555)$. The relationship $R_{rs}(443)/R_{rs}(555)$ vs. $a_{w+p}(555)/a_{w+p}(443)$ (Figure 1.5a) is good and although it is somewhat steeper than the 1:1 line, there is a good resemblance to the relationship $R_{rs}(443)/R_{rs}(555)$ vs.

$a(555)/a(443)$. For brevity, we here use the symbol a_{w+p} to indicate the sum of the absorption coefficients of pure water and particles, $a_w + a_p$. Similarly abbreviated symbols are used for other absorption components.

Within the suspended particulate matter, it is the phytoplankton component that appears to be the stronger determinant than detritus of the relationship $R_{rs}(443)/R_{rs}(555)$ vs. $a(555)/a(443)$ in our data set. The relationship $R_{rs}(443)/R_{rs}(555)$ vs. $a_{w+ph}(555)/a_{w+ph}(443)$ is good and it is characterized by somewhat steeper slope than the 1:1 line (Figure 1.5b). In contrast, the relationship involving the detrital absorption component, $R_{rs}(443)/R_{rs}(555)$ vs. $a_{w+d}(555)/a_{w+d}(443)$, shows larger scatter in the data points and generally smaller slope (Figure 1.5c). The result that the band ratio $a_{w+ph}(555)/a_{w+ph}(443)$ is a major IOP component driving the variation in $R_{rs}(443)/R_{rs}(555)$, is consistent with the observation that phytoplankton dominate the total particulate absorption in our data set across the entire range of measured POC (Figure 1.6).

The analysis of the role of absorption by soluble matter (Figure 1.5d) shows the largest scatter in data points and the lowest correlation amongst the plots presented in Figure 1.5. This indicates that the variability in the band ratio of soluble absorption can be an important source of "noise" in the relationship between the reflectance band ratio and IOPs, and hence in the POC band-ratio algorithm. Nevertheless, the comparison of Figures 1.4c and 1.5a shows that regardless of whether the contribution of soluble absorption is included or neglected, the degree of correlation between the reflectance band ratio and absorption band ratio remains similar.

1.3.2. Single-Wavelength Two-step Algorithm for POC

In addition to band-ratio algorithms, we examined a single-wavelength two-step algorithm for estimating POC from ocean reflectance. This algorithm uses a single waveband in the green spectral region and is based on the approach proposed originally by *Stramski et al*. [1999]. The present version of the algorithm consists of two empirical relationships, $R_{rs}(555)$ vs. $b_b(555)$ and POC vs. $b_{bp}(555)$ (Figure 1.7). When applied to remotely-sensed data from satellite observations, the algorithm operates in such a way that $b_b(555)$ is first calculated from satellite-derived $R_{rs}(555)$ and then POC is calculated from $b_{bp}(555) = b_b(555) - b_{bw}(555)$.

One reason for exploring the two step algorithms is based on fundamental concepts relating the optical properties of the ocean to constituents of seawater. Whereas the IOPs of seawater depend solely on seawater constituents, the ocean reflectance which is an apparent optical property (AOP), depends on both the IOPs and the ambient light field. The two-step algorithm involves separate relationships, first to link the IOP and water constituent concentration (i.e., b_b and POC in our study), and second to link AOP and IOP (i.e., R_{rs} and b_b in our study). The linkage between R_{rs} and b_b has justification in radiative transfer theory. Thus, each step of the two-step algorithm has an improved mechanistic basis compared with a direct relationship between reflectance and water constituent concentration. Another important reason for why we are interested in empirical approaches for POC estimation other than those based on the BG reflectance band ratio is associated with traditional estimation of chlorophyll-*a* concentration from the band-ratio algorithms. Naturally, if the same reflectance band ratios are used as input to both POC and

chlorophyll-*a* algorithms, then both estimated variables are unrealistically forced to always covary. In contrast, other approaches to POC algorithms, such as the single-wavelength two-step POC algorithm examined in this study, have the potential for decoupling the estimation of POC from the band ratio based estimation of chlorophyll-*a*.

The relationship which provides a means for estimating $b_b(555)$ from $R_{rs}(555)$ shows strong correlation between these variables for our Southern Ocean data set (Figure 1.7a). However, a few data points that were collected during an intense bloom of *Phaeocystis antarctica* in the Ross Sea (NBP97 cruise) show significant departure from the trend line. During this bloom, the concentrations of POC exceeded 800 mg m^{-3} and chlorophyll-*a* was as high as 12.5 mg m^{-3}. These bloom data were excluded from the calculation of the final regression equation for $b_b(555)$ vs. $R_{rs}(555)$.

The data of POC vs. $b_{bp}(555)$, representing the second relationship of the two-step algorithm, show significant scatter (Figure 1.7b). This result is consistent with the expectation that the POC-specific backscattering coefficient in the ocean can exhibit considerable variation due to variability in composition and size distribution of particulate matter [*Stramski et al*., 2004]. We note, for example, that the small-sized detrital particles were likely less abundant relative to larger particles and phytoplankton cells in the Ross Sea compared with the PFZ region [*Reynolds et al*., 2001]. This could be a main reason for the fact that the data from the Ross Sea (NBP97 cruise) show consistently lower values of $b_{bp}(555)$ at any given POC, if compared to data from other regions of the Southern Ocean examined in this study.

Given these differences, we have tested the relationship POC vs. $b_{bp}(555)$ separately for the data sets from different cruises. These tests showed that whereas the Ross Sea regression (NBP97) is significantly different, the other regression lines from the PFZ in the Pacific sector (REV98) and from the region off Antarctic Peninsula (AMLR04, LMG04, and AMLR06) are similar to one another. Therefore, for determining the final equations that link POC to $b_{bp}(555)$, we determined two regressions; one based on the combined data set from REV98, AMLR04, LMG04, and AMLR06 (solid line in Figure 1.7b), and the other based on the NBP97 data (dashed line in Figure 1.7b). This clear differentiation between the NBP97 and other cruises in Figure 1.7b supports a notion that regional/seasonal approaches are often required for establishing acceptable bio-optical relationships. Such approaches are based on the assumption that characteristic parameters or relationships can be quasi-constant on regional and seasonal scales [*Platt and Sathyendranath*, 1988; *Mueller and Lange*, 1989].

The equations of the two-step algorithms, the best fit parameters, and error statistics are provided in Table 1.3. The statistical parameters of step 1 and step 2 equations have reasonably good values. However, the aggregate error statistics calculated from the composite formula of the two-step algorithm caution against the use of this algorithm (Table 1.4). The aggregate errors are significantly larger compared with those for the step 1 and step 2 equations considered separately. For example, MNB is about 11% and NRMS over 40% for the composite two-step algorithm based on the data collected on all cruises except NBP97. For the NBP97 data the errors are higher.

We also calculated the differences between the predicted POC from the reflectance band-ratio algorithm and the predicted POC from the composite formulation of the two-step algorithm. In these calculations, we used the field data of reflectance obtained at 65 stations excluding the Ross Sea. The $R_{rs}(443)/R_{rs}(555)$ ratio was used as input to the band-ratio algorithm (see Table 1.1) and $R_{rs}(555)$ was used as input to the composite two-step algorithm in which the coefficients D_1 and D_2 were obtained with data from all cruises except for NBP97 (see Table 1.3). The POC concentrations predicted from the two-step algorithm were found to be higher, on average, by nearly 9% than those predicted from the band-ratio algorithm. This result is consistent with higher values of MNB for the two-step algorithm compared with the band-ratio algorithms. The NRMS and RMSE errors are also higher for the two-step algorithm. In addition, whereas we observed regional differentiation in the step 2 relationship of the single-wavelength algorithm, the band-ratio algorithms are expected to be less susceptible to regional differentiation.

1.3.3. Validation of POC algorithms

Figure 1.8 compares the match-up observations of remote-sensing reflectances, $R_{rs}(443)$ and $R_{rs}(555)$, as well as the band ratio $R_{rs}(443)/R_{rs}(555)$, obtained from *in situ* and satellite measurements using the match-up criteria described in section 1.2.5. The error parameters and the associated formulas used in the calculations of the errors for these match-up data sets are listed in Table 1.5. These error parameters are the same or similar to those presented recently in the validation analysis of SeaWiFS data products of water-leaving radiances and chlorophyll *a* concentration by *Bailey and*

Werdell [2006]. In particular, the median of the ratio of satellite-derived value to *in situ* value for a given variable, *MR*, provides a measure of overall bias in satellite data relative to *in situ* data. The semi-interquartile range, *SIQR*, calculated for the satellite to *in situ* ratio indicates the spread of these data. The overall degree of agreement between the satellite and *in situ* measurements is provided by the median value of the absolute percent difference, *MPD*, between the satellite and *in situ* data, and also by the root mean square deviation, RMSD, between these data. The correlation coefficient, *R*, and the slope of the linear regression of satellite versus *in situ* data are also listed in Table 1.5, which provide additional information on how well the satellite retrievals agree with the *in situ* measurements over their dynamic range. In this analysis we used the Model II regression method, in which the functional relationship is estimated by the slope of the major (principal) axis of the bivariate dataset. This method is suitable for estimating the functional relationship between the *X* and *Y* variables when both variables are subject to measurement error, are expressed in the same units of measurement, and there is no purpose to derive a predictive relationship [*Sokal and Rohlf*, 1995].

The satellite-derived reflectance $R_{rs}(443)$ tends to overestimate the *in situ*-derived values with a median bias of +6.7% (*MR* = 1.067). The match-up data set for $R_{rs}(443)$ shows a satisfactory average trend but the scatter in the data points is large and the correlation is moderate (Figure 1.8a). For $R_{rs}(555)$, most of *in situ* data fall within a relatively small range of values, which is not well matched by satellite data (Figure 1.8b). Whereas the *MR* at 555 nm is slightly lower than unity indicating minimal median bias, most of other statistical parameters indicate poor comparisons at

this waveband. The blue-to-green band ratio $R_{rs}(443)/R_{rs}(555)$ shows, however, relatively good match-up comparisons (Figure 1.8c). The median bias is +6.5% and the correlation is quite high with *R* nearly 0.8. The slope of linear regression is 10% higher than unity. Although there is a significant spread of data, these match-up results for $R_{rs}(443)/R_{rs}(555)$ are encouraging for the application of the band-ratio algorithm for estimating POC.

The analysis of match-up data from various oceanic regions by *Bailey and Werdell* [2006] showed a bias toward underestimation of normalized water-leaving radiances. For example, for their global data set consisting of 629 match-up data points at 443 nm and 555 nm, the median bias was -8.5%. Our much smaller data set from the Southern Ocean does not show such trend toward a negative bias. However, the errors characterizing the spread of data (*SIQR*) and the overall agreement between the satellite and *in situ* match-ups (*MPD*) in our data set are higher compared with the global data set analyzed by *Bailey and Werdell* [2006]. The differences are most significant at the 555 nm waveband. The previous global and present Southern Ocean match-up comparisons indicate that the primary data products derived from satellite ocean color measurements, the normalized water-leaving radiances or remote-sensing reflectances, are typically within 10% to over 20% of the coincident *in situ* determinations. The correct interpretation of these discrepancies must account not only for the uncertainties in the characterization of satellite instrument that measures top-of-atmosphere (TOA) radiances [*Barnes et al*., 1999; *Hooker and McClain*, 2000] and atmospheric correction algorithm that estimates the water-leaving radiances from the TOA radiances [*Gordon*, 1997; *Antoine and Morel*, 1999], but also for the

uncertainty in the *in situ* radiometric measurements, which can play a significant role in these match-up comparisons [*Hooker and Maritorena*, 2000].

Comparisons of satellite-derived POC and *in situ* POC determinations are shown in Figure 1.9 for the POC band-ratio algorithm utilizing $R_{rs}(443)/R_{rs}(555)$ as input (Figure 1.9a) and for the single-wavelength two-step algorithm which utilizes $R_{rs}(555)$ as input (Figure 1.9b). The median bias of satellite POC derived from the band-ratio algorithm is about +15% and the *MPD* error is 32% (Table 1.5). There is a reasonable trend and correlation between the satellite-derived and *in situ* POC values over their dynamic range. The *R* value is 0.6 and the slope of the linear regression is about 1.1, the latter being about the same as the slope for the band ratio $R_{rs}(443)/R_{rs}(555)$. While interpreting these comparisons, it must be stressed, however, that the agreement between the satellite-derived POC and *in situ* POC data cannot be expected to exceed the accuracy of the empirical relationships that form the "in-water" POC algorithm itself. For example, whereas the *RMSE* for our POC band-ratio algorithm shown in Figure 1.3a is about 34 mg m^{-3} (see Table 1.1), the *RMSD* for the match-up data shown in Figure 1.9a is ~45 mg m^{-3} (see Table 1.5).

The match-up POC data for the band-ratio algorithm (Figure 1.9a) show considerably better agreement than those for the single-wavelength two-step algorithm (Figure 1.9b). This is explained largely by results shown in Figure 1.8 where the match-up comparisons for $R_{rs}(443)/R_{rs}(555)$ are better than those for $R_{rs}(555)$. In addition, the error parameters for the single-wavelength algorithm are higher compared with the band-ratio algorithm (see Tables 1.1, 1.3, and 1.4). As a result, the match-ups for the single-wavelength algorithm show relatively poor agreement

associated primarily with large spread in data points (Figure 1.9c). For example, the median bias is about +27%, *MPD* is 50%, and *R* is only ~0.2. Although our match-up analysis does not provide a definite verification of the POC algorithms in the Southern Ocean, these results clearly favor the application of the band-ratio algorithm and caution against the use of the single-wavelength two-step algorithm at the present time.

1.4. Conclusions

In this paper we have explored the empirical algorithms for estimating surface concentration of POC from remote-sensing reflectance in the Southern Ocean. Several algorithm formulations have been tested using field data collected during a number of cruises between 1997 and 2006. The simple power function relating POC to the blue-to-green reflectance ratio, $R_{rs}(443)/R_{rs}(555)$, promises the best performance among the algorithms tested. The best fit regression function of the band-ratio algorithm based on 85 pairs of field data shows a small mean bias of about 3%, the normalized mean square error of 27%, and the determination coefficient of 0.93. In practice of remote sensing applications, one has to recognize a compromise between acceptable margin of error in satellite data product and scientific benefits from use of satellite observations. The accuracy of the proposed POC algorithm in open ocean waters is expected to be comparable to the accuracy of standard empirical chlorophyll-*a* algorithms, which are also based on the blue-to-green band ratios of reflectance or normalized water-leaving radiance. As the present study is focused on the Southern Ocean, the proposed POC algorithm should be most suited to regional or basin-scale

applications within that part of the global ocean. The benefits from the application of this algorithm to the study of seasonal and interannual variability of POC within the Southern Ocean have been demonstrated in *Allison et al*. [in press]. Regional differences in the algorithm parameterization are likely to occur as suggested by comparisons of the present Southern Ocean algorithms with similar algorithms developed recently with field data from lower latitudes within the eastern South Pacific and eastern Atlantic [*Stramski et al*., 2008]. Further studies with more data are needed to assess the significance of these differences.

It is generally recognized that the best way to validate ocean color algorithms is to compare algorithm-derived satellite data product with *in situ* measurements made at the same time and location. Typically the difficulty in validating the algorithms is caused by the low percentage of usable ship-based stations for such satellite vs. *in situ* match-up comparisons, especially in high latitude waters. In addition, the results of match-up comparisons for data products such as POC are affected not only by imperfect performance of the POC algorithm itself, but also by other factors such as uncertainties in satellite sensor characterization and performance, atmospheric correction, and *in situ* measurements. Despite these limitations, our initial validation results support the use of the $R_{rs}(443)/R_{rs}(555)$ band-ratio algorithm as the primary algorithm for estimating POC from ocean color remote sensing in the Southern Ocean. The application of the single-wavelength two-step algorithm which utilizes $R_{rs}(555)$ as input, is not recommended at the present time. However, further efforts to establish POC algorithms that do not use the blue-to-green band ratio are desirable, especially

in view of potential benefits from decoupling the POC data product and standard chlorophyll-*a* data product derived from empirical band-ratio algorithms.

Chapter 1, in full, has been submitted for publication as it may appear in *Journal of Geophysical Research, Oceans* 2010, Allison, David B., Stramski, Dariusz, Mitchell, B. Greg. The dissertation author was the primary investigator and author of this paper.

1.5. Acknowledgments

This work was funded by NASA Ocean Biology and Biogeochemistry Program (Grant NNG04GO02G awarded to D.S), NSF Chemical Oceanography Program (OCE-0324680 to D.S.), NASA (G2004-2983 to B.G.M), NSF (ANT0444134 to B.G.M), NASA and NSF (NAG5-7100 and OPP 98-023836 to D.S. and B.G.M.) as part of the US JGOFS Antarctic Environment Southern Ocean Process Study, NSF Graduate Student Fellowship (awarded to D.B.A.), the NOAA Fisheries' U.S. Antarctic Marine Living Resources (AMRL) Program, and the NASA SIMBIOS program. We are grateful to Rick Reynolds, Mati Kahru, Haili Wang, and John Wieland for their invaluable contributions to the execution of our field program and data processing. We also thank the SeaWiFS Project and the NASA's Goddard Earth Sciences Data and Information Services Center DAAC (NASA's Ocean Color Website) for the production and distribution of ocean color data. The technical staff of Antarctic Support Associates, scientists, officers, and crews of the R/V *Nathaniel B. Palmer*, R/V *Roger Revelle*, R/V *Yuzhmorgeologiya*, and R/V *Laurence M. Gould* are acknowledged for providing logistical support and their help onboard during the field work. The analysis of samples for particulate organic carbon was made at Marine Science Institute Analytical Laboratory, University of California Santa Barbara.

1.6. Figures

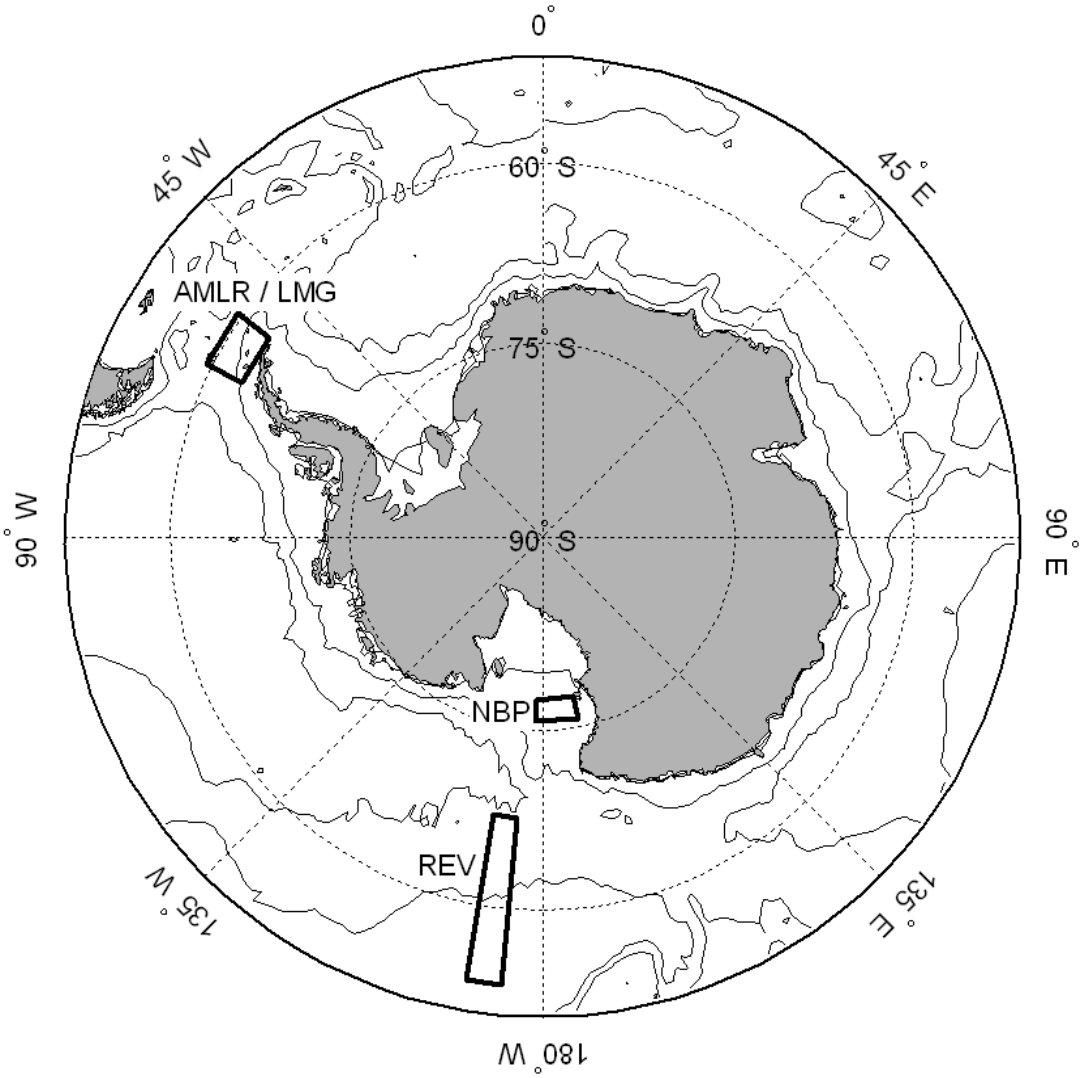

Figure 1.1. Three main areas within the Southern Ocean (indicated by boxes) where the optical and POC measurements used in the development and validation of POC algorithms were made. The AMLR/LMG, REV, and NBP symbols next to the boxes refer to cruises in these areas (see text for details).

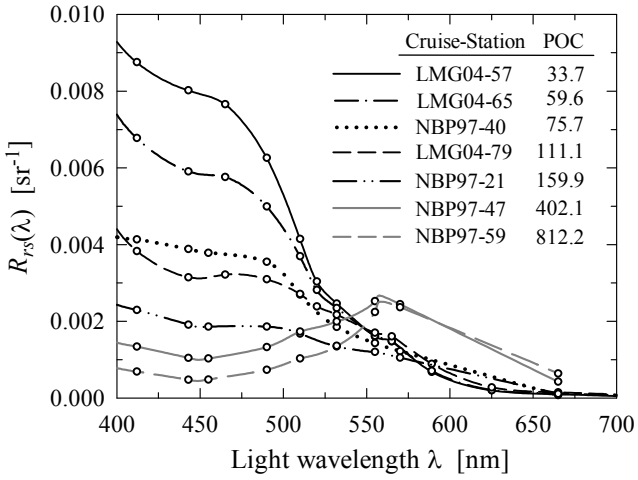

Figure 1.2. Example spectra of remote-sensing reflectance, $R_{rs}(\lambda)$, measured on different cruises in the Southern Ocean at stations with different levels of surface particulate organic carbon (POC). The name of the cruise/station and the POC concentrations are indicated. The open circles indicate discrete wavebands at which the radiometric measurements were taken.

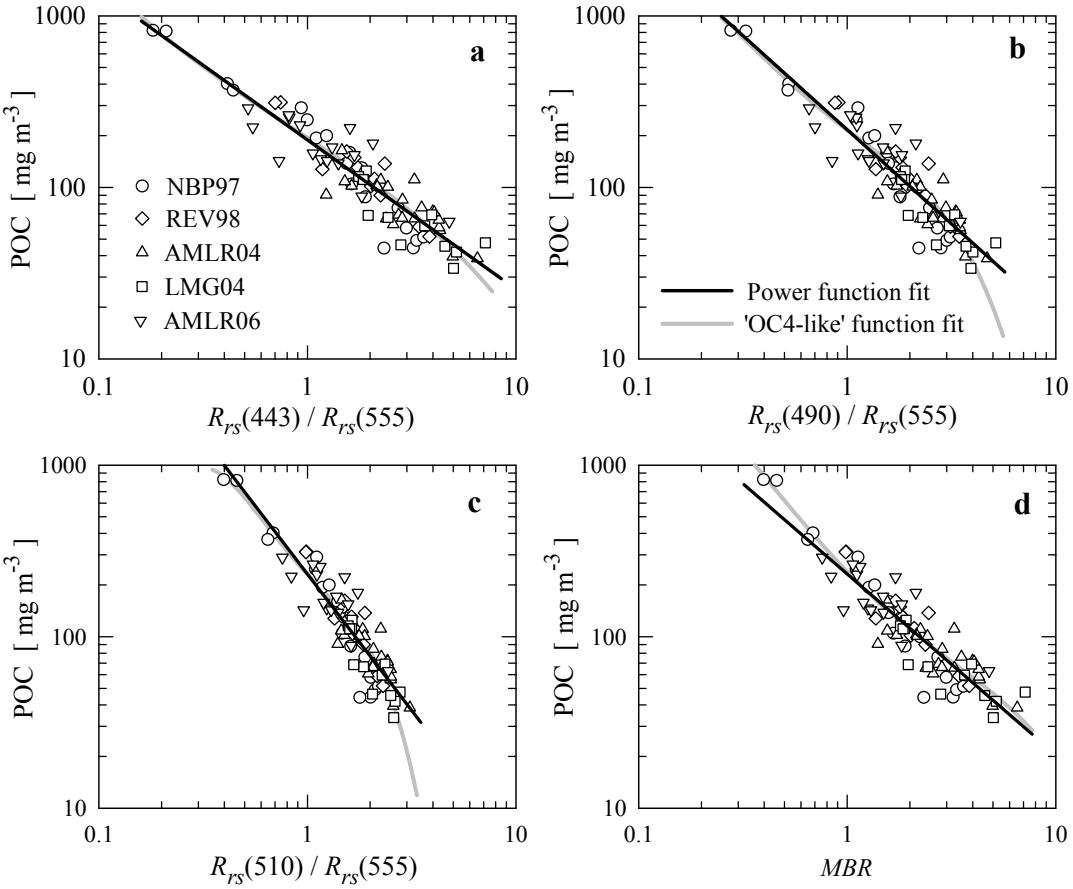

Figure 1.3. Relationships between surface concentration of particulate organic carbon, POC, and the blue-to-green band ratio of remote-sensing reflectance, $R_{rs}(\lambda_B)/R_{rs}(555)$. The light wavelength λ_B is 443 nm (panel a), 490 nm (b), and 510 nm (c). MBR (panel d) is the maximum band ratio which refers to the maximum value of the three band ratios considered. The data points from several cruises are shown by different symbols as indicated in panel (a). The power function fits to all data (solid black lines) and the "OC4-like" function fits (solid grey lines) are also shown (see Table 1.1 for regression coefficients and error statistics).

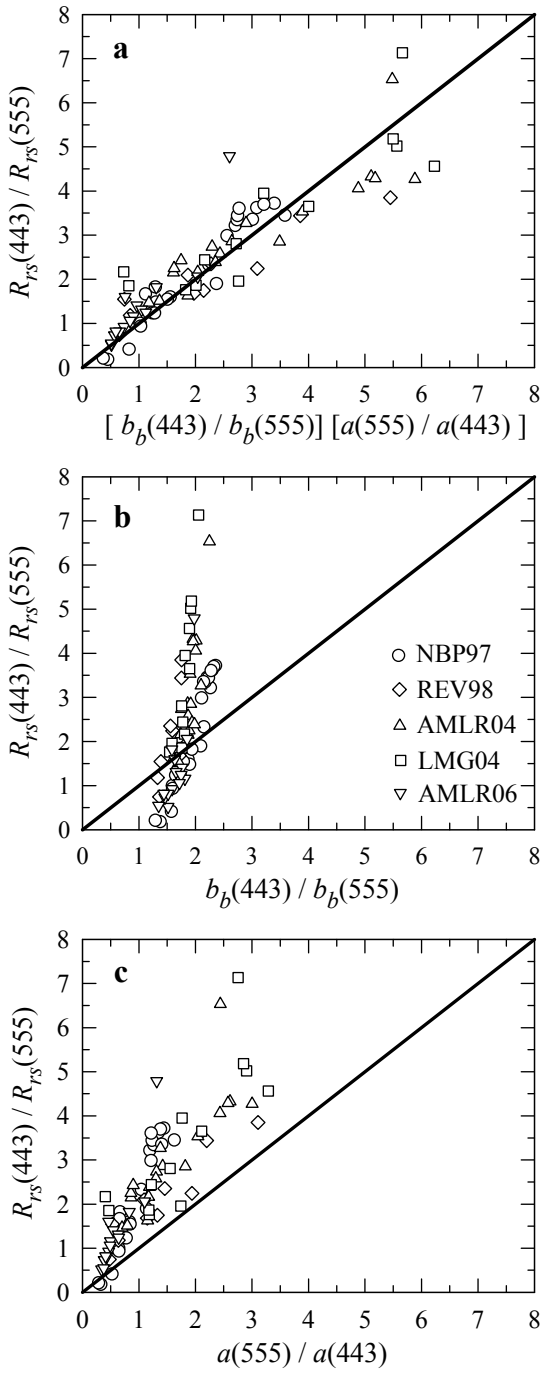

Figure 1.4. Relationships for the blue-to-green reflectance ratio, $R_{rs}(443)/R_{rs}(555)$ versus (a) the product of the backscattering ratio and the absorption ratio, $[b_b(443)/b_b(555)]$ $[a(555)/a(443)]$, (b) the backscattering ratio, $b_b(443)/b_b(555)$, and (c) the absorption ratio, $a(555)/a(443)$. The data obtained in surface waters on different cruises and the 1:1 line are shown.

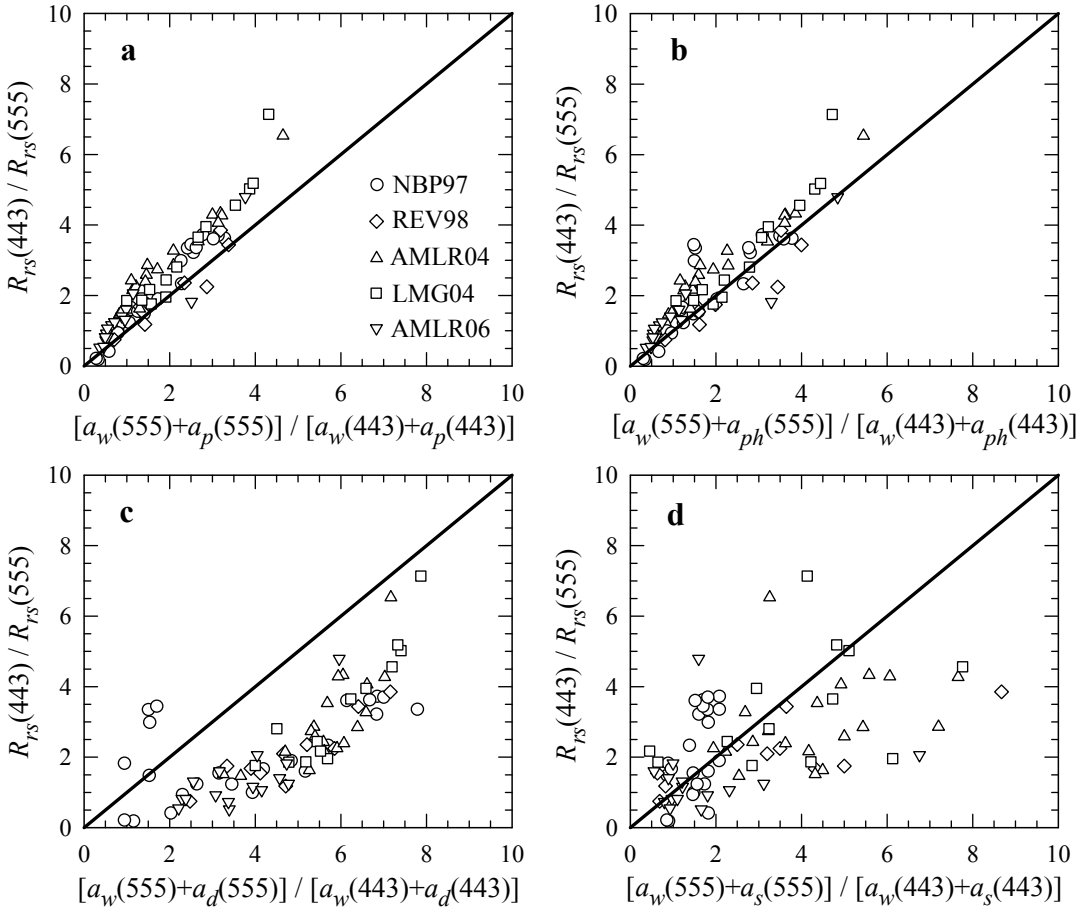

Figure 1.5. Relationships for the blue-to-green reflectance ratio, $R_{rs}(443)/R_{rs}(555)$ versus (a) the band ratio of absorption due to pure water and total particulate matter, $[a_w(555) + a_p(555)]/[a_w(443) + a_p(443)]$, (b) the band ratio of absorption due to pure water and phytoplankton, $[a_w(555) + a_{ph}(555)]/[a_w(443) + a_{ph}(443)]$, (c) the band ratio of absorption due to pure water and non-phytoplankton particles, $[a_w(555) + a_d(555)]/[a_w(443) + a_d(443)]$, and (d) the band ratio of absorption due to pure water and soluble matter, $[a_w(555) + a_s(555)]/[a_w(443) + a_s(443)]$. The data obtained in surface waters on different cruises and the 1:1 line are shown.

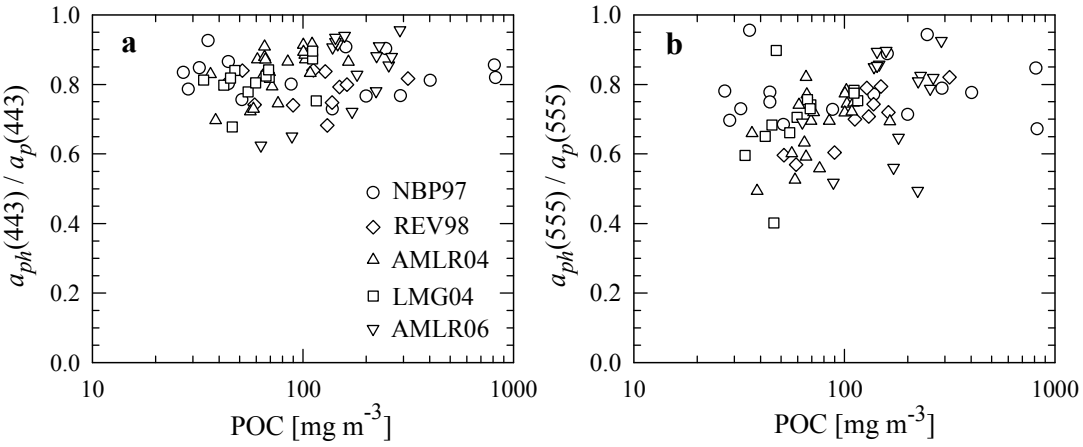

Figure 1.6. The contribution of phytoplankton absorption to total particulate absorption at a light wavelength of (a) 443 nm and (b) 555 nm, across the entire range of measured POC. The data obtained in surface waters on different cruises are shown.

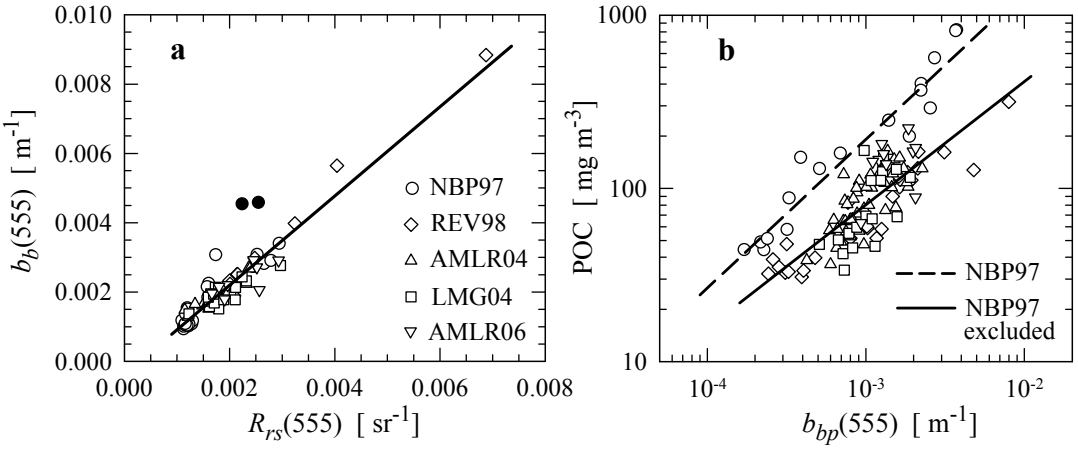

Figure 1.7. (a) Relationship between surface values of the backscattering coefficient, $b_b(555)$, and remote-sensing reflectance, $R_{rs}(555)$. (b) Relationship between surface concentration of particulate organic carbon, POC, and particulate backscattering coefficient, $b_{bp}(555)$. The data from different cruises and the best fit regression lines are shown. Panel (a) shows the linear fit (solid line). Two outlying data points (solid circles) collected on the NBP97 cruise in the Ross Sea during intense bloom of *Phaeocystis antarctica* were excluded from the regression analysis. Panel (b) shows the power function fit for two data sets, one from all cruises combined with the exception of NBP97 (solid line) and the other from the NBP97 cruise only (dashed line) (see Table 1.3 for regression coefficients and error statistics).

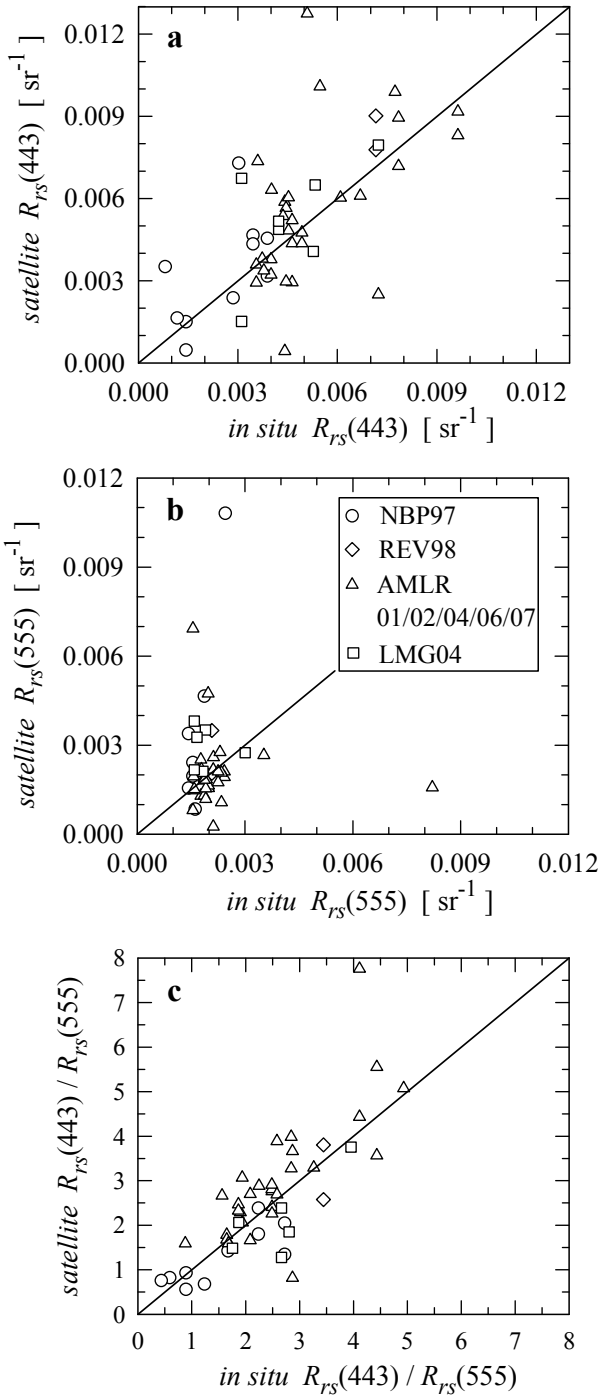

Figure 1.8. Scatter plots showing match-up comparisons of SeaWiFS-derived and *in situ* data for (a) remote-sensing reflectance R_{rs} at 443 nm, (b) remote sensing-reflectance R_{rs} at 555 nm, and (c) band ratio of remote-sensing reflectance, $R_{rs}(443)/R_{rs}(555)$. The match-up data points from different cruises are indicated by different symbols with all AMLR cruises grouped together. The 1:1 line is also shown.

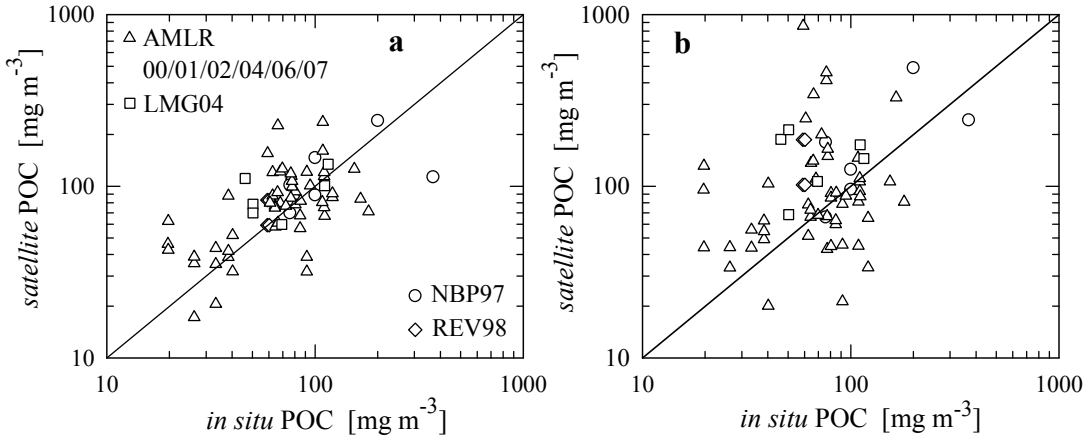

Figure 1.9. Scatter plots showing match-up comparisons of SeaWiFS-derived and *in situ* data of POC. In panel (a) the satellite-derived POC was determined from the POC band-ratio algorithm, which utilizes satellite-derived $R_{rs}(443)/R_{rs}(555)$ as input to the algorithm. In panel (b) the satellite POC was determined from the single-wavelength two-step algorithm utilizing satellite-derived $R_{rs}(555)$ as input. The match-up data points from different cruises are indicated by different symbols with all AMLR cruises grouped together. The 1:1 line is also shown.

1.7. Tables

Table 1.1. Summary of fitted equations and error statistics for the band-ratio POC algorithms depicted in Figure 1.3. Power functions POC = $A\,X^B$ (where X is the blue-to-green band ratio of remote-sensing reflectance, $R_{rs}(\lambda_B)/R_{rs}(555)$ or *MBR*, POC is in mg m^{-3}, and A and B are regression coefficients) were fitted by least squares linear regression analysis using $\log_{10}$-transformed data of POC and $R_{rs}(\lambda_B)/R_{rs}(555)$ or MBR. The light wavelength λ_B is either 443, 490, or 510 nm and *MBR* is the maximum band ratio which refers to the maximum value of the three band ratios considered. All regression coefficients and statistical parameters have been recalculated to represent the non-transformed data. For comparison, the error statistics are also shown for the following function: $\mathrm{POC} = 10^{p_1 + p_2 \log_{10}(MBR) + p_3[\log_{10}(MBR)]^2 + p_4[\log_{10}(MBR)]^3 + p_5[\log_{10}(MBR)]^4}$, as such formulation is currently used in the Ocean Chlorophyll 4 (OC4) algorithm [see *O'Reilly et al.*, 2000]. The coefficients of this fit were obtained by nonlinear regression. R^2 is the determination coefficient, *RMSE* the root mean square error, *MNB* the mean normalized bias, *NRMS* the normalized root mean square error, and N the number of observations (see Table 1.2 for statistical formulas).

POC = $A\,X^B$:

X	*A*	*B*	R^2	*RMSE* [mg m^{-3}]	*MNB* [%]	*NRMS* [%]	*N*
$R_{rs}(443)/R_{rs}(555)$	189.29	-0.870	0.933	34.46	3.22	27.33	85
$R_{rs}(490)/R_{rs}(555)$	216.54	-1.097	0.915	38.64	3.43	27.81	85
$R_{rs}(510)/R_{rs}(555)$	232.20	-1.590	0.899	42.12	3.48	28.09	85
MBR	231.68	-1.054	0.851	51.29	3.66	29.13	85

$\mathrm{POC} = 10^{p_1 + p_2 \log_{10}(MBR) + p_3[\log_{10}(MBR)]^2 + p_4[\log_{10}(MBR)]^3 + p_5[\log_{10}(MBR)]^4}$ where the fitted coefficients are $p_1 = 2.379$, $p_2 = -1.264$, $p_3 = 0.4669$, $p_4 = 0.1569$, and $p_5 = -0.4541$:

R^2	*RMSE* [mg m^{-3}]	*MNB* [%]	*NRMS* [%]	*N*
0.924	37.32	6.43	28.68	85

Table 1.2. Equations used for calculating error statistics shown in Tables 1.1, 1.3, and 1.4. P_i is the variable predicted from the regression fit, for example the predicted POC concentration (in mg m^{-3}), O_i the measured variable, for example the measured POC concentration (in mg m^{-3}), $\overline{O}$ the mean value of measured variable, R^2 the determination coefficient, *RMSE* the root mean square error (for POC variable the units of this error are mg m^{-3}), *MNB* the mean normalized bias (in percent), *NRMS* the normalized root mean square error (in percent), *N* the number of observations, and *m* the number of coefficients in the fit. In the formula for R^2, the numerator is the sum of squares due to error and the denominator is the sum of squares about the mean.

Determination coefficient	$R^2 = 1 - \dfrac{\sum_{i=1}^{N}(P_i - O_i)^2}{\sum_{i=1}^{N}(O_i - \overline{O})^2}$
Root mean square error	$RMSE = \left[\dfrac{1}{N-m}\sum_{i=1}^{N}(P_i - O_i)^2\right]^{1/2}$
Mean normalized bias	$MNB = \dfrac{1}{N}\sum_{i=1}^{N}\left(\dfrac{P_i - O_i}{O_i}\right)100\%$
Normalized root mean square error	$NRMS = \left[\dfrac{1}{N-1}\sum_{i=1}^{N}\left(\dfrac{P_i - O_i}{O_i} - \dfrac{MNB}{100}\right)^2\right]^{1/2} 100\%$

Table 1.3. Summary of fitted equations and error statistics for the two-step POC algorithm depicted in Figure 1.7. Least squares linear regression analysis was applied to calculate the coefficients C_1, C_2, D_1, and D_2. For the step 2 relationship, the regression analysis was applied to $\log_{10}$-transformed data of POC and $b_{bp}(555)$. The regression coefficients and statistical parameters have been recalculated to represent the non-transformed data. R^2 is the determination coefficient, *RMSE* the root mean square error, *MNB* the mean normalized bias, *NRMS* the normalized root mean square error, and *N* the number of observations (see Table 1.2 for statistical formulas). $b_b(555)$, $b_{bp}(555)$, and $b_{bw}(555)$ are in m^{-1}, POC is in mg m^{-3}, and $R_{rs}(555)$ in sr^{-1}.

Step 1 equation: $b_b(555) = C_1 R_{rs}(555) + C_2$

	C_1	C_2	R^2	*RMSE* [m^{-1}]	*MNB* [%]	*NRMS* [%]	*N*
All cruises*	1.2871	-0.0003793	0.922	0.0002977	1.10	13.64	83

*Except for two NBP97 stations with intense bloom of *Phaeocystis* and POC > 800 mg m^{-3} (see text and Figure 1.7 for more details).

Step 2 equation: $\text{POC} = D_1 b_{bp}(555)^{D_2}$ where $b_{bp}(555) = b_b(555) - b_{bw}(555)$

	D_1	D_2	R^2	*RMSE* [mg m^{-3}]	*MNB* [%]	*NRMS* [%]	*N*
All cruises except for NBP97	10970.5	0.7117	0.566	31.95	4.68	32.03	98
NBP97	71992.6	0.8582	0.841	102.61	4.29	32.00	18

Table 1.4. Summary of aggregate error statistics for the composite representation of the two-step POC algorithm depicted in Figure 1.7. The composite formulation of the algorithm is: POC = D_1 [C_1 $R_{rs}(555)$ + C_2 - $b_{bw}(555)$]^{D_2}. The coefficients C_1 and C_2 of the step 1 equation and the coefficients D_1 and D_2 of the step 2 equation are given in Table 1.3. POC is in mg m^{-3}, $R_{rs}(555)$ in sr^{-1}, $b_{bw}(555)$ in m^{-1}, R^2 is the determination coefficient, *RMSE* the root mean square error, *MNB* the mean normalized bias, *NRMS* the normalized root mean square error, and *N* the number of observations (see Table 1.3 for statistical formulas). Fifty one observations include measurements taken at stations that were used in the development of step 1 equation, step 2 equation, or both equations, and where $R_{rs}(555)$ and POC were measured. Because of variations in water temperature and salinity, the values of pure seawater backscattering, $b_{bw}(555)$, vary slightly in our data set around the average value of 0.0008565 m^{-1} (standard deviation = 3.688 x 10^{-6} m^{-1}, N = 159). This average value was used in the calculations of error statistics for the composite representation of the two-step algorithm.

	R^2	*RMSE* [mg m^{-3}]	*MNB* [%]	*NRMS* [%]	*N*
All cruises except for NBP97	0.450	39.38	11.44	43.63	51
NBP97	0.488	82.01	19.78	51.17	18

Table 1.5. Summary of error statistics for the match-up data sets of *in situ* and satellite-derived variables shown in Figures 1.8 and 1.9. For the POC variable, the error statistics are shown for match-ups with satellite retrievals of POC derived from two algorithms; first, a band-ratio algorithm utilizing satellite-derived $R_{rs}(443)/R_{rs}(555)$ (see section 1.3.1 for details), and second, a single-wavelength two-step algorithm utilizing satellite-derived $R_{rs}(555)$ (see section 1.3.2 for details). The value of *R* is the correlation coefficient between the satellite and *in situ* data and the slope represents a slope of the principal axis of Model II linear regression. The *MR* is the median ratio of satellite to *in situ* values and *SIQR* is the semi-interquartile range for this ratio calculated as $SIQR = (Q_3 - Q_1)/ 2$, where Q_1 is the 25th percentile and Q_3 is the 75th percentile. The *MPD* is the median absolute percent difference calculated as the median of the individual absolute percent differences $PD_i = 100 |Y_i - X_i| / X_i$ where Y_i is the satellite-derived value and the X_i is the *in situ* value. The *RMSD* is the root mean square deviation between the satellite and *in situ* values calculated as $RMSD = [N^{-1} \sum(Y_i - X_i)^2]^{1/2}$, with the summation from $i = 1$ to N. N is the overall number of match-up observations and the values in parenthesis indicate the number of *in situ* observations for which satellite match-ups were identified. Some *in situ* observations were matched with 2 or 3 satellite observations, which correspond to consecutive satellite overpasses over the area of *in situ* station and pass our match-up criteria (see section 1.2.5 for details).

Variable	*R*	*Slope*	*MR*	*SIQR*	*MPD* [%]	*RMSD*	*N*
$R_{rs}(443)$	0.636	1.155	1.067	0.195	20.65	0.00209 sr^{-1}	49 (33)
$R_{rs}(555)$	0.016	1.381	0.982	0.258	22.48	0.00197 sr^{-1}	48 (33)
$R_{rs}(443)/R_{rs}(555)$	0.776	1.106	1.065	0.208	19.89	0.863	48 (33)
POC (band-ratio algorithm)	0.604	1.097	1.147	0.256	32.43	44.7 mg m^{-3}	72 (44)
POC (two-step algorithm)	0.193	2.502	1.277	0.635	50.08	140.7 mg m^{-3}	68 (41)

1.8. References

Allison, D. B., D. Stramski, and B. G. Mitchell (2010), Seasonal and interannual variability of particulate organic carbon within the Southern Ocean from satellite ocean color observations, *J. Geophys. Res.,*115, C06002, doi:10.1029/2009JC005347.

Antoine, D. and A. Morel (1999), A multiple scattering algorithm for atmospheric correction of remotely sensed ocean colour (MERIS instrument): principle and implementation for atmospheres carrying various aerosols including absorbing ones, *Int. J. Remote Sens.*, *20*, 1875-1916.

Bailey, S. W. and P. J. Werdell (2006), A multi-sensor approach for the on-orbit validation of ocean color satellite data products, *Remote Sens. Environ*., *102*, 12-23.

Barnes, R. A., R. E. Eplee, Jr., F. S. Patt, and C. R. McClain (1999), Changes in the radiometric sensitivity of SeaWiFS determined from lunar and solar-based measurements, *Appl. Opt*., *38*, 4649-4664.

Behrenfeld, M. J., E. Boss, D. A. Siegel, and D. M. Shea (2005), Carbon-based ocean productivity and phytoplankton physiology from space, *Global Biogeochem. Cycles*, *19*, GB1006, doi:10.1029/2004GB002299.

Boss, E. and W. S. Pegau (2001), The relationship of light scattering at an angle in the backward direction to the backscattering coefficient, *Appl. Opt., 40*, 5503–5507.

Boss, E., M. S. Twardowski, and S. Herring (2001), Shape of the particulate beam attenuation spectrum and its inversion to obtain the shape of the particulate size distribution, *Appl. Opt., 40*, 4885-4893.

Buiteveld, H., J. H. M. Hakvoort, and M. Donze (1994), The optical properties of pure water, in: *Ocean Optics XII*, *Proc. SPIE, 2258*, edited by: Jaffe, J. S., pp. 174-183, SPIE, Bellingham, Washington.

Dana, D. R. and R. A. Maffione (2002), Determining the backward scattering coefficient with fixed-angle backscattering sensors - Revisited, Ocean Optics XVI, Santa Fe, New Mexico, 18-22 November.

Dierssen, H. M. and R. C. Smith (2000), Bio-optical properties and remote sensing ocean color algorithms for Antarctic Peninsula waters, *J. Geophys. Res., 105 (C11)*, 26301-26312.

Esaias, W. E., R. L. Iverson, and K. Turpie (2000), Ocean province classification using ocean colour data: observing biological signatures of variations in physical dynamics, *Global Change Biol.*, *6*, 39-55.

Gardner, W. D., A. V. Mishonov, and M. J. Richardson (2006), Global POC concentrations from *in-situ* and satellite data, *Deep-Sea Res., Part II, 53*, 718-740.

Gordon, H. R. (1997), Atmospheric correction of ocean color imagery in the Earth Observing System era, *J. Geophys. Res*., *102 (D14)*, 17081-17106.

Gordon, H. R., O. B. Brown, and M. M. Jacobs (1975), Computed relationships between the inherent and apparent optical properties of a flat, homogenous ocean, *Appl. Opt*. 14: 417- 427.

Gordon, H. R. and A. Morel (1983), *Remote assessment of ocean color for interpretation of satellite visible imagery - A review. Lecture notes on coastal and estuarine studies*, 114 pp., Springer-Verlag, New York.

Hooker, S. B. and S. Maritorena (2000), An evaluation of oceanographic radiometers and deployment methodologies, *J. Atmos. Oceanic Tech.*, *17*, 811-830.

Hooker, S. B. and C. R. McClain (2000), The calibration and validation of SeaWiFS data, *Prog. Oceanogr.*, *45*, 427-465.

Hooker, S. B., N. W. Rees, and J. Aiken (2000), An objective methodology for identifying oceanic provinces, *Prog. Oceanogr*., *45*, 313-338.

Kishino, M., M. Takahashi, N. Okami, and S. Ichimura (1985), Estimation of the spectral absorption coefficients of phytoplankton in the sea, *Bull. Mar. Sci., 37*, 634-642.

Knap, A., A. Michaels, A. Close, H. Ducklow, and A. Dickson, Eds. (1996), Protocols for the Joint Global Ocean Flux Study (JGOFS) Core Measurements, JGOFS Report Nr. 19 (Reprint of the IOC Manuals and Guides No. 29, UNESCO, Paris, 1994), 170 pp.

Loisel, H., E. Bosc, D. Stramski, K. Oubelkheir, and P.-Y. Deschamps (2001), Seasonal variability of the backscattering coefficient in the Mediterranean Sea based on satellite SeaWiFS imagery, *Geophys. Res. Lett.*, *28*, 4203-4206.

Longhurst, A. R. and W. G. Harrison (1989), The biological pump: Profiles of plankton production and consumption in the upper ocean, *Prog. Oceanogr., 22*, 47-122.

Maffione, R. A. and D. R. Dana (1997), Instruments and methods for measuring the backward-scattering coefficient of ocean waters, *Appl. Opt., 36*, 6057-6067.

Marrari, M., C. Hu, and K. Daly (2006), Validations of SeaWiFS chlorophyll *a* concentrations in the Southern Ocean: A revisit, *Remote Sens. Environ*., *105*, 367-375.

McClain, C. R. (2009), A decade of satellite ocean color observations, *Annu. Rev. Mar. Sci., 1*, 19-42.

McClain, C. R., G. C. Feldman, and S. B. Hooker (2004), An overview of the SeaWiFS project and strategies for producing a climate research quality global ocean bio-optical time series, *Deep-Sea Res., Part II, 51*, 5-42.

Mitchell, B. G. (1990), Algorithm for determining the absorption coefficient of aquatic particulates using the quantitative filter technique (QFT), in *Ocean Optics X*, *Proc. SPIE, 1302*, edited by R. W. Spinrad, pp. 137-148, SPIE, Bellingham, Washington.

Mitchell, B. G. (1992), Predictive bio-optical relationships for polar oceans and marginal ice zones, *J. Mar. Syst*., *3*, 91-105.

Mitchell, B. G. and O. Holm-Hansen (1991), Bio-optical properties of Antarctic Peninsula waters: Differentiation from temperate ocean models, *Deep-Sea Res*., *Part A*, *38*, 1009-1028.

Mitchell, B. G., M. Kahru, J. Wieland, and M. Stramska (2002), Determination of spectral absorption coefficients of particles, dissolved material and phytoplankton for discrete water samples, in *Ocean Optics Protocols for Satellite Ocean Color Sensor Validation. Revision 3*, J. L. Mueller and G. S. Fargion (eds.), NASA Technical Memorandum, 2002-21004/Rev3, Vol. 2, NASA Goddard Space Center Greenbelt, Maryland, 231-257.

Mishonov, A. V., W. D. Gardner, and M. J. Richardson (2003), Remote sensing and surface POC concentration in the South Atlantic, *Deep Sea Res., Part II, 50*, 2997–3015.

Morel, A. (1974), Optical properties of pure water and pure sea water, in *Optical Aspects of Oceanography*, edited by N. G. Jerlov and E. Steeman-Nielsen, pp. 1-24, Academic Press, New York.

Morel, A. and L. Prieur (1977), Analysis of variations in ocean color, *Limnol Oceanogr., 22*, 709-722.

Mueller, J. L. and R. E. Lange (1989), Biooptical provinces of the northeast Pacific Ocean – A provisional analysis, *Limnol. Oceanogr., 34*, 1572-1586.

Mueller, J. L., G. S. Fargion, and C. R. McClain, Eds. (2003), Ocean Optics Protocols for Satellite Ocean Color Sensor Validation, Revision 4, Volume III: Radiometric Measurements and Data Analysis Protocols, *NASA/TM-2003-211621/Rev4-Vol. III*, 78 pp., NASA Goddard Space Flight Center, Greenbelt, Maryland.

O'Reilly, J. E, S. Maritorena, B. G. Mitchell, D. A. Siegel, K. L. Carder, S. A. Garver, M. Kahru, and C. R. McClain (1998), Ocean color chlorophyll algorithms for SeaWiFS, *J. Geophys. Res., 103*, 24937 - 24953.

O'Reilly, J. E., S. Maritorena, D. A. Siegel, M. C. O'Brien, D. Toole, B. G. Mitchell, M. Kahru, F. P. Chavez, P. Strutton, G. F. Cota, S. B. Hooker, C. R. McClain, K. L. Carder, F. Müller-Karger, L. Harding, A. Magnuson, D. Phinney, G. F. Moore, J. Aiken, K. R. Arrigo, R. Letelier, and M. Culver (2000), Ocean color chlorophyll *a* algorithms for SeaWiFS, OC2 and OC4: Version 4, *NASA Tech. Memo*, *2000-206892, vol. 11*, 9-27.

Pabi, S., and K. R. Arrigo (2006), Satellite estimation of marine particulate carbon in waters dominated by different phytoplankton taxa, *J. Geophys. Res., 110*, C10018, doi:10.1029/ 2005JC003137.

Parsons, T. R., Y. Maita, and C. M. Lalli (1984), *A Manual of Chemical and Biological Methods for Seawater Analysis*, 173 pp., Pergamon Press, Oxford, UK.

Platt, T. and S. Sathyendranath (1988), Oceanic primary production: estimation by remote sensing at local and regional scales, *Science*, *241*, 1613-1620.

Pope, R. M. and E. S. Fry (1997), Absorption spectrum (380-700 nm) of pure water. II. Integrating cavity measurements, *Appl. Opt., 36*, 8710-8723.

Reynolds, R. A., D. Stramski, and B. G. Mitchell (2001), A chlorophyll-dependent semianalytical reflectance model derived from field measurements of absorption and backscattering coefficients within the Southern Ocean, *J. Geophys. Res.*, *106*, 7125-7138.

Sathyendranath, S., G. Cota, V. Stuart, H. Maass, and T. Platt (2001), Remote sensing of phytoplankton pigments: a comparison of empirical and theoretical approaches, *Int. J. Remote Sens.*, *22*, 249-273.

Shifrin, K. (1988), *Physical Optics of Ocean Waters*, 285 pp., Am. Inst. Phys., New York.

Sokal, R. R. and F. J. Rohlf (1995), *Biometry: The Principles and Practice of Statistics in Biological Research*, 3rd edition, 887 pp., W. H. Freeman and Co., New York.

Son, Y. B., W. D. Gardner, A. V. Mishonov, M. J. Richardson (2009), Multispectral remote-sensing algorithms for particulate organic carbon (POC): The Gulf of Mexico, *Remote Sens. Environ., 113*, 50-61.

Stramska, M. (2009), Particulate organic carbon in the global ocean derived from SeaWiFS ocean color, *Deep-Sea Res., Part I, 56*, 1459-1470.

Stramska, M. and D. Stramski (2005), Variability of particulate carbon concentration in the north polar Atlantic based on ocean color observations with Sea-viewing Wide Field-of-view Sensor (SeaWiFS), *J. Geophys. Res*., *110*, C10018, doi:10.1029/2004JC002762.

Stramski, D., E. Boss, D. Bogucki, and K. J. Voss (2004), The role of seawater constituents in light backscattering in the ocean, *Prog. Oceanogr.*, *61*, 27-55.

Stramski, D., R. A. Reynolds, M. Babin, S. Kaczmarek, M. R. Lewis, R. Röttgers, A. Sciandra, M. Stramska, M. S. Twardowski, B. A. Franz, and H. Claustre (2008), Relationships between the surface concentration of particulate organic carbon and optical properties in the eastern South Pacific and eastern Atlantic Oceans, *Biogeosciences*, *5*, 171-201.

Stramski, D., R. A. Reynolds, M. Kahru, and B. G. Mitchell (1999), Estimation of particulate organic carbon in the ocean from satellite remote sensing, *Science, 285*, 239-242.

Thuillier, G., M. Herse, P. C. Simon, D. Labs, H. Mandel, D. Gillotay, and T. Foujols (2003), The solar spectral irradiance from 200 to 2400 nm as measured by the SOLSPEC spectrometer from the ATLAS 1-2-3 and EURECA missions, *Sol. Phys*, *214*, 1–22.

Twardowski, M. S., H. Claustre, S. A. Freeman, D. Stramski, and Y. Huot (2007) Optical backscattering properties of the "clearest" natural waters, *Biogeosciences, 4*, 1041-1058.

Volk, T. and M. I. Hoffert (1985), Ocean carbon pumps: Analysis of relative strengths and efficiencies in ocean-driven atmospheric CO_2 changes, in *The Carbon Cycle and Atmospheric CO_2: Natural Variations Archean to Present*, *Geophys. Monogr. Ser.*, vol. 32, edited by E. T. Sundquist and W. S. Broecker, pp. 99–110, AGU, Washington, D. C.

Yoder, J. A. and M. A. Kennelly (2006) What have we learned about ocean variability from satellite ocean color imagers?, *Oceanography, 19(1)*, 152-171.

Chapter 2. Analysis of the Contributions of Particle Classes to the Bulk Particulate Organic Carbon, Chlorophyll-*a*, and Optical Properties of Seawater

2.0. Abstract

Previous work has suggested the ability to estimate the particulate organic carbon (POC) concentration in oceanic waters from the measured inherent and apparent ocean optical properties such as particulate backscattering coefficient (b_{bp}), particulate beam attenuation coefficient (c_p), and remote-sensing reflectance R_{rs}. The relationships providing a basis for this estimation have been shown to exhibit significant variability generally related to spatial and temporal differences in bio-optical properties of seawater within the world's oceans. A major source of this variability is thought to be the differing particulate assemblages, both in terms of composition and relative abundances. There is limited information on the relationship between the major contributing classes of particles to bulk POC and those that dominate inherent and apparent ocean optical properties. We have used a combination of Mie scattering modeling and data from previous laboratory experiments to calculate carbon and chlorophyll-*a* content as well as spectral absorption, scattering, and backscattering coefficients for 21 representative classes of particles, each of which plays a distinctly different role in marine optics and biochemistry. These classes represent colloids, organic detritus, minerals, and various plankton species or groups ranging from heterotrophic bacteria and photoautotrophic cyanobacteria to nano- and microphytoplankton. The particle classes cover a particle size range from 0.015 μm to

200 μm, which represents most optically significant particles in the open ocean. By using a reductionist model of particle class properties, 38 bulk models of seawater were constructed and analyzed. These bulk models differ from one another in terms of detailed composition of the various particle classes.

The utility of this approach in advancing an understanding of variability in the critical bio-optical relationships underlying POC algorithms is shown, for example, the relationship between POC and particulate backscattering and the relationship between POC and the blue-to-green band ratio of backscattering and absorption coefficients. In contrast to traditional approaches in which seawater has been parameterized in an overly simplified manner using only a few broadly defined categories of water constituents, the reductionist approach presented here provides insights into the sources of bio-optical variability with unprecedented detail by quantifying the relative contributions of each of the particle classes to bulk POC, chlorophyll-*a*, and optical properties of seawater. For example, our model simulations also suggest the general significance of colloidal particles and minerals to backscattering and the significant contributions to POC from the phytoplankton, detritus, bacteria, and colloid particle classes.

2.1. Introduction

The bio-optical relationships, including those forming a basis of ocean color remote sensing algorithms, are known to exhibit significant regional and temporal variability in the ocean. This variability, and its limited understanding, have been a major obstacle for achieving consistently good performance of remote sensing

algorithms. As an example, our previous work showed significant regional differences in the relationship between particulate organic carbon (POC) concentration and optical backscattering, one of the candidate relationships for remote sensing of POC [*Stramski et al*., 1999]. A major source of such variability is thought to be associated with variations in particulate assemblages, both in terms of composition and relative abundances of various particle classes. Unfortunately, the present understanding of how different particle classes contribute to bulk concentrations of seawater constituents such as POC and to bulk ocean optical properties is very limited. This is because the natural particulate assemblages have been traditionally described in terms of a few broadly defined classes such as phytoplankton and non-phytoplankton particles. This traditional description is a great oversimplification of reality.

Here we apply a reductionist approach [*Stramski et al*., 2001; 2004] for advancing our understanding of bio-optical relationships in terms of the detailed composition of particulate assemblages. Much of our attention is focused on the bio-optical relationships involving POC and inherent optical properties of seawater. We consider 21 classes of particles found in ocean waters which cover the size range from 0.015 μm to 200 μm, such as colloids, heterotrophic bacteria, organic detritus, mineral particles, and several groups of phytoplankton from picoplankton through microplankton size range. The particle classes were defined to reflect their potentially distinctive optical and biochemical roles in the ocean. Optical and biochemical properties were determined via Mie modeling and empirical relationships for each particle class. Representative bulk models of mixtures of particle classes, 38 in total, were created by assigning total particle counts for each particle class based on particle

counts observed in the ocean. Bulk optical and biochemical properties were then calculated for each model and compared against field measurements from the Southern Ocean to gain insight into particle class contribution to observed bulk properties in the region of primary interest to this study.

2.2. Methods

2.2.1. Overview

Current ocean color remote-sensing algorithms typically employ a reflectance band ratio relationship of a blue-to-green spectral band [*O'Reilly et al*., 1998] to estimate in-water constituents such as particulate organic carbon (POC) or chlorophyll-*a* (Chl) concentrations. Radiative transfer modeling has shown that the spectral remote-sensing reflectance $R_{rs}(\lambda)$ is proportional to the spectral backscattering coefficient of seawater, $b_b(\lambda)$, and is inversely proportional to the spectral absorption coefficient of seawater, $a(\lambda)$ [*e.g.*, *Gordon and Morel*, 1983]:

$$R_{rs}(\lambda) \propto \frac{b_b(\lambda)}{a(\lambda)} \tag{2.1}$$

where λ is light wavelength in vacuo. The coefficients $a(\lambda)$ and $b_b(\lambda)$ are the inherent optical properties (IOPs) of seawater, which are totally dependent upon seawater composition. The total IOPs of a water body are the sum of the relevant bulk IOPs associated with each of the various components of a water body. For example, the total absorption coefficient $a(\lambda)$ in units m^{-1} is the sum of the absorption coefficients of the pure water $a_w(\lambda)$, soluble or colored dissolved organic matter $a_{CDOM}(\lambda)$, and individual (k) particle components $a_{p,k}(\lambda)$ which include colloids, organic detritus,

minerals, and various plankton species or groups ranging from heterotrophic bacteria and photoautotrophic cyanobacteria to nano- and microphytoplankton.

$$a(\lambda) = a_w(\lambda) + a_{CDOM}(\lambda) + \sum_k a_{p,k}(\lambda) \qquad (2.2)$$

The other IOPs, the scattering coefficient $b(\lambda)$, the backscattering coefficient $b_b(\lambda)$, the beam attenuation coefficient $c(\lambda)$, and the volume scattering function $\beta(\Psi,\lambda)$, all have similar relationships to their constituent parts. For example, the total backscattering coefficient $b_b(\lambda)$ is the sum of the backscattering coefficients of the pure water $b_{bw}(\lambda)$, bubbles $b_{bbub}(\lambda)$, and individual particle components $b_{bp,k}(\lambda)$ including bacteria, phytoplankton, detritus, and minerals in the water.

$$b_b(\lambda) = b_{bw}(\lambda) + b_{bbub}(\lambda) + \sum_k b_{bp,k}(\lambda) \qquad (2.3)$$

This approach of describing the bulk IOPs in terms of the detailed composition of seawater (*i.e.*, a significant number of distinctly different water constituents) can be referred to as the reductionist approach [*Stramski et al.*, 2001].

The focus in the present analysis is on examining the roles of different particle types as primary drivers of bulk seawater IOPs in open ocean waters. Scattering by bubbles is not considered in the present modeling because the dynamic effects of bubbles on optics are poorly characterized and our primary interest is on the effects of particles . The absorption coefficient by CDOM is modeled with an empirical relationship as a function of the chlorophyll-*a* concentration. All particulate components are defined and modeled as described below.

2.2.2. Modeling IOPs of particle classes

Modeling the IOPs of specific types of marine particles allows for a detailed examination of the contribution of the various particle classes to the total bulk properties of seawater. A member of each constituent class can be modeled optically with a relative particle size distribution (PSD) and complex index of refraction (m) of particles relative to water. Single particle optical efficiencies, $Q_i(\lambda)$, can be calculated using the Mie theory solution to Maxwell's electromagnetic equations for a homogenous sphere [*Bohren and Huffman*, 1983]. The optical cross section, $\sigma_i(\lambda)$, at a given wavelength λ, of a single particle of diameter D and complex index of refraction m is then

$$\sigma_i(\lambda) = Q_i(\lambda, m(\lambda), D) \cdot \frac{\pi D^2}{4} \tag{2.4}$$

where the subscript i represents either the absorption, scattering, backscattering, or attenuation optical property. For example, the single particle cross section for absorption $\sigma_a(\lambda) = Q_a(\lambda,m,D)\pi D^2/4$.

For a polydisperse group of particles of a single class with size distribution $N(D)dD$, the optical efficiency Q_i and particle diameter D are replaced by a representative "average" value for the entire group of particles. The $N(D)dD$ indicates the number of particles within the size bin $D + dD$ per unit volume of water. The representative optical cross section for the class is then

$$\overline{\sigma_{i,k}}(\lambda) = \overline{Q_{i,k}}(\lambda, m(\lambda), \overline{D_k}) \cdot \frac{\pi \overline{D_k}^2}{4} \tag{2.5}$$

where the overbar indicates that this is the average property for the representative particle of this class. The bulk IOP for a given (k^{th}) particle class can then be calculated as the product of the "average" optical cross section $\overline{\sigma_{i,k}}(\lambda)$ for that class and the total number of particles of that class per unit volume of water, N_k. For example, the bulk absorption coefficient for a particular species of phytoplankton $a_{p,k}(\lambda)$ in units m^{-1} is

$$a_{p,k}(\lambda) = \overline{\sigma_{a,k}}(\lambda) \cdot N_k \tag{2.6}$$

Note, the conventional nomenclature for the absorption coefficient of phytoplankton is $a_{ph,k}(\lambda)$. In the current work, all particle class optical properties will be referred to with the subscripts *p* for particle and *k* for class index. Thus, for any phytoplankton class included in our model, $a_{ph,k}(\lambda)$, is referred to simply as $a_{p,k}(\lambda)$, just like other non-phytoplankton particle classes.

Other particle class-specific IOPs can be calculated in similar fashion. Total bulk IOPs of seawater can then be constructed by accumulation, for example, as indicated in Equation 2.2, of all constituent classes each with a set of representative optical properties dependent on the size distribution and complex index of refraction. The approach for generating bulk models is described below in section 2.2.4.

2.2.3. Modeling POC and Chl for particle classes

There is considerable evidence to suggest that POC is related to measurable optical properties. This evidence comes from both field and laboratory studies on bulk optical properties and in-water constituents as well as laboratory studies relating single

particle optics and single particle carbon concentrations. The link between these single particle relationships and the bulk relationships provides a method to model bulk POC from similar particle class inputs as those used in IOP modeling, namely particle size distribution and complex index of refraction.

Many previous studies have explored the relationship between bulk optical properties and in-water constituents based on field data. Several groups have shown that POC can be estimated from the IOP of the particulate beam attenuation coefficient c_p [*Gardner et al*., 1993; Bishop, 1999]. Work by *Loisel and Morel* [1998] has also shown that the particulate scattering coefficient, $b_p(550)$, can be used to derive an estimate of POC. *Stramski et al*. [1999] has further extended the scattering – POC relationship and looked at particulate backscattering, $b_{bp}(\lambda)$, as a proxy for POC in the Southern Ocean (see also Chapter 1 in this dissertation). Recent work [*Stramska and Stramski*, 2005; *Stramski et al*., 2008; Chapter 1 in this dissertation] has also explored the relationship between the apparent optical property (AOP) of ocean reflectance and POC concentration.

Similar work on relating bulk optical properties, c_p and b_p, to particulate organic carbon has been carried out in the laboratory on single species phytoplankton cultures [*Stramski and Morel*, 1990; *Stramski and Reynolds*, 1993]. For example, in the *Stramski and Morel* [1990] study it was shown that a single species phytoplankton culture of cyanobacterium grown under a range of lighting conditions produced a good relationship between the measured particulate scattering coefficient at 560 nm, $b_p(560)$, and bulk carbon concentration.

Laboratory studies have also investigated single particle carbon content and single particle optical properties. The relationship between the cellular carbon content and particle size has been studied for many plankton species and taxonomic groups [*Verity et al*., 1992; *Montagnes et al*., 1994]. Furthermore, there are several studies that explore the relationship between intracellular (intraparticle) carbon concentration and the real part of the refractive index of planktonic cells [*Stramski*, 1999; *DuRand et al*., 2002].

In the present work, the relationship established by *DuRand et al*. [2002] is used to model intraparticle carbon ($C_{p,k}$) concentration in units mg m^{-3} for any given (k^{th}) particle class:

$$C_{p,k} = 3946 \cdot n(650) - 3922 \tag{2.7}$$

where $n(650)$ is the real part of the refractive index of the particle class relative to water at 650 nm. The POC_k concentration for an assemblage of particles of concentration N_k representing a given class is then

$$\mathrm{POC_k} = N_k \cdot C_{p,k} \cdot \frac{\pi \overline{D_k}^3}{6} \tag{2.8}$$

where the product $C_{p,k}$ times $\pi \overline{D_k}^3 / 6$ is the mass of carbon per particle. *DuRand et al*. [2002] also proposed a model for intraparticle chlorophyll-*a* ($Chl_{p,k}$) concentration in units mg m^{-3} for any given (k^{th}) particle class:

$$Chl_{p,k} = 1244 \cdot n'(676) - 0.32 \tag{2.9}$$

where $n'(676)$ is the imaginary part of the refractive index of the particle relative to water at a wavelength of 676 nm where chlorophyll-*a* exhibits a maximum absorption

and other pigments have insignificant contribution to absorption. The chlorophyll-*a* concentration, $\mathrm{Chl_k}$, for an assemblage of particles of concentration N_k representing a given class is then

$$\mathrm{Chl_k} = N_k \cdot Chl_{p,k} \cdot \frac{\pi \overline{D_k}^3}{6} \tag{2.10}$$

where the product $Chl_{p,k}$ times $\pi \overline{D_k}^3 / 6$ is the mass of chlorophyll-*a* per particle.

2.2.4. Modeling bulk POC, Chl, and IOPs

The use of the above particle-specific models for generating the bulk seawater models of POC, Chl, and IOPs allows for a method to directly inspect the contribution of representative particle classes (for example, a given k^{th} class) to bulk biochemical properties and bulk IOPs. In addition, the bulk AOPs of the ocean, such as remote sensing reflectance, could be modeled using radiative transfer simulations with the bulk IOPs as inputs. In this study radiative transfer modeling is not used, rather, the ratio of IOPs is used as a proxy for ocean reflectance as indicated in Equation 2.1. Variation of the particle class properties such as size distribution or particle concentration and inclusion or exclusion of the particle classes in the mixture of particulate assemblages allows for investigation of the effects of the various combinations of detailed particle composition on the total carbon concentration (POC), chlorophyll-*a* concentration (Chl), and bulk optical properties (IOPs and AOPs) of the ocean. This in turn results in a more thorough understanding of the complexity of the system in terms of optical-biochemical relationships. This reductionist approach is powerful and unique in the areas of ocean optics and bio-

optical oceanography because seawater is represented in terms of a significant number of optically and biochemically important constituent classes, each playing a different role in marine optics and biogeochemistry. In contrast, seawater has traditionally been parameterized in a highly oversimplified manner in terms of a few broadly defined categories of constituent classes, such as all suspended particles as a single class or all phytoplankton species as a single class. Such an approach cannot satisfactorily explain the substantial optical variability in the ocean due to varying composition in seawater constituents.

Bulk properties of seawater, including the POC, Chl, and IOPs, were modeled by assemblages of several particle classes which are representative of particles found in the world's oceans. These particle classes consisted of colloids (COL1-COL3), minerals (MIN1-MIN4), organic detritus (DET1-DET5), heterotrophic bacteria (HBAC), and various plankton species or groups (PROC, SYNE, SYMA, PEUK, NAN1, NAN2, MIC1, and MIC2). Table 2.1 lists the 21 distinct particle classes used in this study. Values for the average cell size ($\overline{D_k}$), real and imaginary parts of the relative index of refraction $n_k(650)$ and $n_k'(676)$ at 650 nm and 676 nm respectively, and carbon ($C_{p,k}$) and chlorophyll ($Chl_{p,k}$) concentration of each component are also given in Table 2.1. Several of the particle classes are permutations of a base class but with a different particle size distribution. For example, detritus was modeled with five different size distributions.

The bulk POC and chlorophyll-*a* concentrations were calculated as the sum of the POC_k and Chl_k of all particle classes within an entire particulate assemblage from:

$$\mathrm{POC} = \sum_k \mathrm{POC}_k \tag{2.11}$$

$$\mathrm{Chl} = \sum_k \mathrm{Chl}_k \tag{2.12}$$

where POC_k and Chl_k are obtained from Equations 2.8 and 2.10, respectively.

Data that characterize the inherent optical properties of several planktonic components were derived from a study based on laboratory measurements of bacterial and phytoplankton cultures and modeling of particle optics [*Stramski et al*., 2001]. These components include heterotrophic bacteria (HBAC) representing a multispecies assemblage of these microbes, and three photoautotrophic picoplankton components, *Prochlorococcus* (PROC), *Synechococcus* (SYNE), and phycocyanin-rich picophytoplankton consisting of *Synechocystis* and *Anacystis* marina species (SYMA). The data for PROC and SYNE result from averaging different strains of *Prochlorococcus* and *Synechococcus* species as described in *Stramski et al*. [2001]. The optical data for the remaining nanophytoplankton (NAN) and microphytoplankton (MIC) components as well as other particle classes (colloids, detritus, minerals) in our model were derived from Mie modeling using assumptions about the particle size distribution and complex index of refraction. Colloids (COL) were assumed to have a relatively low value (1.04) for the real part of refractive index relative to water, which is consistent with the assumption that colloids are largely organic particles with significant water content. Detritus (DET) similarly represents a diverse assemblage of non-living organic particles but of larger sizes (> 1 μm). Minerals (MIN) are the only particulate component characterized by high refractive index (1.16), which is

consistent with inorganic particles. Naturally, COL, DET, MIN, and HBAC classes contain no chlorophyll and MIN classes contain no organic carbon.

The particle classes have a representative size distribution either measured experimentally or based on a modeled distribution. The range of particle diameters and the basis for the size distributions for each particle class are shown in Table 2.2. Note, for example, that nanophytoplankton is represented by two components, small nanophytoplankton (NAN1) ranging in size from 2 μm to 8 μm, and large nanophytoplankton (NAN2) from 8 μm to 20 μm. The colloidal fraction of particulate matter (< 1 μm) is also considered in two size classes, small colloids (COL1 and COL2 from 0.015 μm – 0.2 μm in size) and large colloids (COL3 from 0.2 μm – 1 μm in size). Similarly, the MIN classes cover different size ranges and the DET classes were modeled with different size distributions to cover the possible realistic scenarios.

For each (k^{th}) particle class (with the exception of HBAC, PROC, SYNE, and SYMA where laboratory measurements provided data) the Mie solution for a polydisperse collection of particles provides the spectral scattering efficiencies $Q_{i,k}(\lambda)$ for absorption, scattering, backscattering, and attenuation (subscript i). The representative optical cross sections $\overline{\sigma_{i,k}}(\lambda)$ were then calculated as indicated in Equation 2.5. For HBAC, PROC, SYNE, and SYMA the optical properties were derived from laboratory measurements with the exception of backscattering which was estimated from Mie calculations [*Stramski et al*., 2001]. The biochemical properties, $C_{p,k}$ and $Chl_{p,k}$, were also calculated for all particle classes from the relationships in Equations 2.7 and 2.9, respectively. In the case of minerals (MIN1-MIN4), the

intraparticle organic carbon concentration ($C_{p,k}$) was assumed to be zero. Additionally, the chlorophyll-*a* concentration per particle ($Ch_{lp,k}$) was set to zero for the HBAC, the colloid classes (COL1-COL3), the detritus classes (DET1-DET5), and the minerals (MIN1-MIN4).

A flow chart depicting the calculations involved in determining the representative particle optical cross sections and biochemical values is indicated in Figure 2.1. The inputs to the models are the class-specific relative particle size distribution $N_{R,k}(D)$ (*i.e.*, relative concentration of particles in each size bin) and the real and imaginary parts of the relative index of refraction of particles, $n_k(\lambda)$ and $n'_k(\lambda)$. A database of these particle properties for each particle class was assembled.

Having determined the optical and biochemical properties for each particle class, a base bulk model was constructed which represents a realistic collection of different particle classes (14 classes in all) at concentrations found in the open ocean. The particle classes and corresponding particle concentrations (N_k in units particles per m^3) included in the base model are described in Table 2.3. Additional models, as defined later, were also created to encompass a broader range of particle assemblages found in the ocean. In the base model there are no mineral particles ($N_k = 0$ for MIN1, MIN2, MIN3) and no *Prochlorococcus* (N_k =0 for PROC), the smallest photosynthetic picoplankton. These particle classes are still included in the model but the particles concentrations were set to 0. This inclusion allows for the permutation of these classes in other models while still maintaining the core members of the particulate assemblage. The assumptions of the base model are meant to realistically represent the open waters within the Southern Ocean, where these particle classes can

be reasonably assumed to have very small or negligible contributions to the optical and biochemical properties. The open waters of the Southern Ocean are of primary interest to this study. The particulate IOPs for each particle class k within the bulk models is determined by the total particle count per unit volume times the optical cross section as indicated in Equation 2.13:

$$IOP_{p,k} = N_k \cdot \overline{\sigma_{i,k}}(\lambda) \tag{2.13}$$

where $IOP_{p,k}$ is the particulate absorption, scattering, backscattering, or attenuation coefficient for class k, N_k is the total particle count per unit volume for class k, and $\overline{\sigma_{i,k}}(\lambda)$ is the representative particle optical cross section for the class k and IOP i. The total POC (POC_k) and chlorophyll-*a* (Chl_k) for the class is found by a similar method (see Equations 2.8 and 2.10). Finally, the total bulk particulate IOPs, POC, and chlorophyll-*a* (Chl) concentration for each model is then the sum of contributions from each particle class within the model (see Equations 2.13, 2.11, 2.12). Figure 2.2 summarizes the steps to achieve the bulk particulate optical and biochemical properties for the models.

As indicated earlier (Equations 2.2 and 2.3), the total IOPs of seawater depend not only on the contributions from various suspended particles, but also on the contributions of pure seawater, colored dissolved organic matter (CDOM), and bubbles. In the current analysis, for calculating the total IOPs of seawater, the pure water absorption values, $a_w(\lambda)$, were taken from *Pope and Fry* [1997], and the pure water scattering $b_w(\lambda)$ and backscattering values $b_{bw}(\lambda)$, were obtained from the study of *Morel* [1974]. Bubbles were not modeled, so the scattering $b_{bub}(\lambda)$ and

backscattering $b_{bbub}(\lambda)$ by bubbles were zero. The CDOM absorption coefficient, $a_{CDOM}(\lambda)$, are modeled empirically as a function of total chlorophyll-*a* concentration, Chl, on the basis of field data from the Southern Ocean [*Reynolds et al.*, 2001].

$$a_{CDOM}(400) = 0.046 \cdot \mathrm{Chl}^{0.298} \tag{2.13}$$

CDOM absorption values at other wavelengths λ are then calculated as

$$a_{CDOM}(\lambda) = a_{CDOM}(400) \cdot e^{-S(\lambda - 400)} \tag{2.14}$$

where the spectral slope S is 0.0195 nm^{-1} [*Reynolds et al.*, 2001].

2.3. Results

2.3.1. Overview

A total of 38 models were considered in the present study; 1 base model as described above and 37 permutations to that base model by addition or removal of the particle classes, changes in the concentration of the particle classes, or changes in the particle size distribution for a given class. Table 2.4 describes each of the models. The models were categorized into 7 broad groups: the base model, alternate (scaled) base models, addition of living phytoplankton classes, high chlorophyll-*a* models, models containing additional heterotrophic bacteria, models containing additional colloids, models containing additional detritus or alternate detrital PSDs, and models containing minerals. Tables 2.5 – 2.11 summarize the changes (scaled values) in the base model (Table 2.3) for each of the other 37 models considered within this study. Each of these models represents a realization of constituent composition within the

ocean. Analysis of the bulk results and comparison to field data from the Southern Ocean for all models is presented in the discussion section 2.4.

Four models (highlighted in Tables 2.4, 2.5 – 2.11) are investigated in detail below; the base model, the high chlorophyll-*a* model (I), the detritus-enriched model (II), and the minerals-enriched model (IV). For each model, the input relative particle size distribution is presented as well as the selection of the particle class concentrations. For each particle class k, the particle concentration N_k, the particulate absorption coefficient at 490 nm ($a_{p,k}(490)$), the particulate scattering coefficient at 555 nm ($b_{p,k}(555)$), the particulate backscattering coefficient at 555 nm ($b_{bp,k}(555)$), the ratio of the total absorption and total backscattering coefficients involving the blue and green wavelengths, and the POC_k and Chl_k concentrations are indicated. The bulk properties for the model are also included. The relative contributions to the bulk $b_{bp}(555)$, POC, and Chl are indicated for each particle class within the model. These four models were chosen as examples of the primary trends in the bulk IOPs, POC, and Chl caused by a given particle group (base, high chlorophyll-*a*, detritus-enriched, and minerals-enriched). A complete listing of all the results, for all models (38), is provided in Table 2.16. The comparison of these results to field data is discussed in section 2.4.

2.3.2. Base Model

The base model (Table 2.3) was constructed to represent one possible realistic collection of particles found in the Southern Ocean with moderate concentrations of POC and chlorophyll-*a*. Figure 2.3 shows the particle size distribution of the base

model. The contribution of each particle class to the total PSD is also indicated. This PSD is similar to the Junge type distribution, typically found in open ocean waters, which changes with particle diameter as D^{-4}. Colloids (COL2, COL3) and bacteria (HBAC) represent the most numerous particles with over 10^{14} and 10^{11} particles per m^{-3} respectively. The total particle count for all classes within the base model is 3.54 x 10^{14} particles per m^{-3}. Small colloids (COL2) represent over 99% of the total particle number within this model. The total POC concentration is 58.97 mg m^{-3} and the chlorophyll-*a* concentration is 0.298 mg m^{-3}. Note that the POC and Chl values are comparable to typical values encountered within the open waters of the Southern Ocean (see Chapter 3 in this dissertation). A complete representation of results for the base model is listed in Table 2.12.

Figure 2.4 indicates the relative contribution of each particle class to the bulk model properties b_{bp}(555), POC, and Chl. Because the colloids represent such a large portion of the particle number within this model, it is expected that they would have a significant contribution to the backscattering signal, especially as the submicron particles have a relatively high backscattering efficiency. Colloids account for over 71% of the total b_{bp}(555) in the model. Colloids (COL2, COL3) and heterotrophic bacteria (HBAC) totally dominate particulate backscattering (94%). All phytoplankton classes combined contribute only 3% to b_{bp}(555). The remaining 3% of particulate backscattering is due to detritus (DET1). Small nanophytoplankton (NAN1) account for 41% of the total chlorophyll-*a* concentration. Overall nanophytoplankton (NAN1, NAN2) contribute 63% to total chlorophyll-*a* concentration with the remaining 20% by microphytoplankton (MIC1), 12% by

picoeukaryotes (PEUK), and 5% by cyanobacteria *Synechococcus* (SYNE). The POC is quite evenly distributed among colloids (28%), detritus (26%), and HBAC (23%). The remaining 23% of POC is attributable to all phytoplankton classes.

2.3.3. High Chlorophyll-*a* Model

The high chlorophyll-*a* model increases the total phytoplankton particle count in the base model by increasing the particle concentrations of several of the phytoplankton classes (living photoautotrophic particles). In addition, increased amounts of colloid and detrital particles were added to this model to represent the additional non-living organic particles. This model represents a potential bloom condition and was constructed to contain large amounts of POC (phytoplankton classes, colloids, and detrital particles) and chlorophyll-*a* (phytoplankton classes). Figure 2.5 shows the particle size distribution of this model where the contributions of each particle class to the total PSD is indicated. The elevated portion of the PSD within both the small (NAN1) and large (NAN2) nanophytoplankton size ranges (2-20 μm) is evident in Figure 2.5. The total POC concentration in this model is 124.77 mg m^{-3} and the chlorophyll-*a* concentration is 1.769 mg m^{-3}. A complete representation of results for the model is listed in Table 2.13.

Figure 2.6 indicates the relative contributions of $b_{bp}(555)$, POC, and Chl for each particle class in the high chlorophyll-*a* model. Again colloids (COL2, COL3) dominate particulate backscattering with bacteria (HBAC) also being an important contributor to the $b_{bp}(555)$. Despite an increased concentration of phytoplankton in this model, the combined contribution of all phytoplankton classes to $b_{bp}(555)$ is still

small (13%) . Nanophytoplankton (NAN1, NAN2) and microphytoplankton (MIC1) account for about 88% of the total chlorophyll-*a* concentration, with 71% attributable to nanophytoplankton. POC is largely associated with the nano- and microphytoplankton (56%) with the remaining portion distributed nearly uniformly among detritus (12%), colloids (13%), and HBAC (11%). The picophytoplankton classes (SYNE and PEUK) contribute about 8% to POC.

2.3.4. Detritus-enriched Model

The detritus-enriched model adds 10 times more detritus (DET1) to the base model. This model was constructed to contain large amounts of POC associated with non-living organics relative to the base model. Figure 2.7 shows the particle size distribution of the detritus-enriched model. The elevated contribution of detritus to the PSD over a broad size range from 1 to 200 μm is evident. The total POC concentration of the detritus-enriched model is 195.83 mg m^{-3} and the chlorophyll-*a* concentration is 0.298 mg m^{-3}. Note that the total POC in this model is significantly higher than our estimates of average POC (varying generally from about 70 to 80 mg m^{-3}) in the surface waters of the Southern Ocean based on the application of our remote-sensing algorithm to satellite data of SeaWiFS [see Chapter 3 in this dissertation]. A complete representation of results for the detritus-enriched model is listed in Table 2.14.

Figure 2.8 indicates the relative contribution of $b_{bp}(555)$, POC, and chlorophyll-*a* for each particle class to the bulk properties of the detritus-enriched model. Colloids (COL2, COL3) account for 56% of the $b_{bp}(555)$ whereas detritus

(DET1) accounts for 24% and bacteria (HBAC) for 17% of the $b_{bp}(555)$. Over 78% of the POC is accounted for in the detritus with the majority of the remaining POC in colloids (9%) and HBAC (7%). Only ~7% of POC is associated with all phytoplankton classes. The chlorophyll-*a* is concentrated in the nano- (63%) and microphytoplankton (20%) with another 12% within the picoeukaryotes (PEUK) and 5% within cyanobacteria (SYNE) classes.

2.3.5. Small Minerals-enriched Model

This model, referred to as the small minerals-enriched model, adds to the base model small minerals (MIN2) at a concentration equivalent to the concentration of large (organic) colloids (COL3, size range 0.2 – 1 μm) present in the base model. This small minerals-enriched model was constructed to contain large amounts of small inorganic particles with relatively high refractive index, which are expected to produce large backscattering signal. Figure 2.9 shows the particle size distribution of this model. The presence of both small minerals and large colloids over the size range 0.2 – 1 μm is evident, which produces a small, albeit noticeable, elevation in the total PSD in that size range. The total POC concentration is 58.97 mg m^{-3} and the chlorophyll-*a* concentration is 0.298 mg m^{-3}, just as in the base model because minerals do not affect these biochemical variables. A complete representation of results for the small minerals-enriched model is listed in Table 2.15.

Figure 2.10 indicates the relative contributions of $b_{bp}(555)$, POC, and chlorophyll-*a* for each particle class in the mineral model. The addition of the small minerals completely changes the budget of the backscattering signal. Small minerals

(MIN2) account for 82% of the $b_{bp}(555)$ whereas colloids account for only 13% and HBAC for only 4% of the total $b_{bp}(555)$. All phytoplankton classes combined remain insignificant with <1% contribution. Because the addition of small minerals did not add any chlorophyll-*a* and carbon, the budgets for Chl and POC remain the same as for the base model.

2.4. Discussion

2.4.1. Overview

The benefit of the reductionist approach in modeling bulk seawater properties is the insight into the relative drivers of a particular signal (bulk IOP, carbon, or chlorophyll-*a*) by different particle classes. As the four example models indicate, the addition of phytoplankton has the strongest effect on chlorophyll-*a* concentration, the addition of detritus on the POC concentration, and the addition of small minerals on the backscattering signal. The consideration of all 38 models and their comparison to field data from the Southern Ocean provides greater insight into the roles of different particle classes as sources of variability in the bulk optical and biochemical properties of ocean waters.

The section below presents a comparison of the Southern Ocean field data with the model data and provides clues to understanding the variability in the bulk seawater properties. In particular, we show the following relationships: (i) Chl vs. $a_p(676)$; (ii) POC:Chl ratio vs. Chl; (iii) the ratio of $a_d(440)/a_p(440)$ vs. Chl; (iv) POC vs. $b_{bp}(555)$; and (v) POC vs. the band ratio of the absorption coefficient to the backscattering coefficient with the 490 nm and 555 nm wavelengths involved. The band ratio of IOP

coefficients is a proxy for the band ratio of remote-sensing reflectance (see Equation 2.1), which is used in the development of our POC remote-sensing algorithm based on the blue-to-green band ratio of reflectance [see Chapter 1 in this dissertation]. The relationship POC vs. $b_{bp}(555)$ is one of the two relationships used in another POC algorithm, which is referred to as a single-wavelength two-step POC algorithm [see Chapter 1 in this dissertation]. Thus, the analysis of these algorithm relationships within the context of the comparisons of the reductionist models and the field data provides a powerful tool for examining the potential variability (or departures) from the main trend lines representing the POC algorithm equations. This analysis has significance to understanding the ultimate performance of POC algorithms and potential uncertainties in these algorithms associated with natural variability in detailed particulate composition of seawater. In each of the comparisons discussed below, the results from all 38 models are overlaid on the field data. The models are colored by group (Table 2.4) to allow for identification of trends associated with specific particle classes. A complete listing of results from all 38 models is presented in Table 2.16.

2.4.2. Field Data

Optical, POC, and chlorophyll-*a* measurements were made during several oceanographic cruises within three regions of the Southern Ocean; in the waters near the Antarctic Peninsula and South Shetland Islands, the Antarctic Polar Frontal Zone (PFZ) within the Pacific sector, and the Ross Sea. The stations were located in high-latitude waters south of 50°S, and most stations were south of 60°S (see Figure 1.1 and

Figure 3.1). The field data were collected during six cruises spanning a time period from 1997 through 2006. These cruises include: (i) the U.S. Joint Global Ocean Flux Study (JGOFS) cruise NBP9711 in the Ross Sea in November-December of 1997; (ii) two JGOFS cruises REV9801 and REV9802 in the PFZ region which took place from January through March 1998; (iii) six cruises under the NOAA Fisheries' U.S. Antarctic Marine Living Resources (AMLR) Program in the region of the South Shetland Islands and Antarctic Peninsula during January-March in 2000, 2001, 2002, 2004, 2006, and 2007; and (iv) one cruise sponsored by the National Science Foundation during the 2004 AMLR season. Data collection and processing methodology is detailed in Chapters 1 and 3 in this dissertation. In the analysis below we restrict the field data to the use of POC and optical data collected at near-surface depths (< 10 m) within open water stations where it is reasonable to assume that optical properties and suspended particles are dominated by plankton microorganisms and plankton-derived organic matter. In bio-optical studies such waters have been customarily referred to as Case 1 waters [*Morel and Prieur*, 1977; *Gordon and Morel*, 1983].

2.4.3. Chlorophyll-*a* versus $a_p(676)$

Southern Ocean field data for chlorophyll-*a* concentration vs. $a_p(676)$ is compared with model results in Figure 2.11. The field data vary over 3 orders of magnitude. The particulate absorption coefficient $a_p(676)$ is affected mostly by chlorophyll-*a* because other phytoplankton pigments and other types of marine particles have very small or negligible absorption at 676 nm. Therefore, a good

correlation between Chl $a_p(676)$ and $a_p(676)$ can be generally expected. Although our field data support this correlation, there is still a significant scatter in the data points. Our model results allow us to explain this scatter in field data, in particular to identify particle composition scenarios that are responsible for the distribution of individual data points along the main trend line or the departure of data points in different directions from the main trend line.

The base model is shown as the large black circle in Figure 2.11, and falls well within the overall pattern of field data. This indicates that our base model is representative of typical conditions in the Southern Ocean. The small black circles represent the alternate base models. These models were obtained simply by scaling up (10x) or down (1/3x) the base model without any changes in the relative proportion of particle classes. These alternate base models are consistent with the main trend of field data. The large color symbols in Figure 2.11 represent the different model groups defined as perturbations to the base model with higher concentrations of different particle classes. Thus, the patterns (vectors) of the color symbols show to what extent a given particle class (as represented by the model group) drives the main trend of the relationship in question or to what extent a given particle class introduces a statistical "noise" into the relationship in question. A major feature seen in Figure 2.11 is that the single-class phytoplankton and high chlorophyll-*a* models (light and dark green circles) are a major source of the main trend of increasing chlorophyll-*a* vs. $a_p(676)$. Although this dominant role of phytoplankton in driving the chlorophyll-*a* vs. $a_p(676)$ relationship is not surprising, an important result is high consistency between the main trend in the field data and a series of models with increased

phytoplankton contributions. These results provide confidence in the ability to realistically model the complex optical and biochemical signal with the reductionist approach. In addition, Figure 2.11 shows that introducing a perturbation to the base model by adding heterotrophic bacteria (red circles), colloids (brown circles), organic detritus (yellow circles), or minerals (blue circles) has a very small or negligible effect on the relationship between chlorophyll-*a* and $a_p(676)$. Again, this is not surprising because these particle classes contain no chlorophyll-*a* and their absorption at 676 nm is very weak or undetectable.

2.4.4. POC:Chl ratio versus chlorophyll-a

Figure 2.12 shows a relationship between the ratio of POC to chlorophyll-*a* (abbreviated as POC:Chl) and the chlorophyll-*a* concentration, with the field data from the Southern Ocean varying over three orders of magnitude. There is considerable interest in understanding the POC:Chl ratio because it has the potential to provide information about the relative roles of phytoplankton and non-phytoplankton POC in seawater and the physiological status of phytoplankton. The field data show that there is a general covariation, with an increase of POC:Chl as Chl decreases. In low chlorophyll-*a* waters, the relative contribution of non-phytoplankton organic carbon to total POC is expected to be generally higher compared with high chlorophyll-*a* waters.

The modeled results are also indicated in Figure 2.12 with the base model (large black circle) located near the center of the field data pattern. This is again an indication that the base model is representative of typical conditions within the

Southern Ocean in terms of POC and Chl concentrations. Two major vectors are evident in the modeled results. The first is the addition of organic detritus (yellow circles) and colloids (brown circles), which drives only the POC concentration as evidenced in an increase in the POC:Chl ratio at a constant chlorophyll-*a* concentration. The second vector (green circles) indicates the dominant driver of the main trend of the presented relationship. This vector results from the addition of phytoplankton classes above the concentrations of the base model, and it follows the main trend of field data well. The high chlorophyll-*a* models (dark green circles) are farther away from the base model than the single-class phytoplankton models (light green circles), which reflects the differences in the phytoplankton cell and chlorophyll concentrations between these models. The inclusion of the organic detritus and colloids in the high chlorophyll-*a* models perturbs the POC:Chl to Chl relationship away from the dominant trend (light green vector) of the phytoplankton models and indicates the complex relationships of the aggregate ensembles of particle classes. Increases in HBAC (red circles) and organic detritus (yellow circles) only change the POC:Chl ratio, because heterotrophic bacteria and detritus contain carbon, but not chlorophyll-*a*. The perturbation of the base model with the addition of minerals has no effect on this relationship, and the alternate base models indicate a possibility for a significant range of Chl values at a given POC:Chl ratio.

2.4.5. $a_d(440)/a_p(440)$ versus chlorophyll-*a*

The ratio of the detrital absorption coefficient $a_d(440)$ to the total particulate absorption coefficient $a_p(440)$ (abbreviated as $a_d{:}a_p$) as a function of chlorophyll-*a*

concentration is presented in Figure 2.13. The ratio of $a_d:a_p$ provides insight into the contribution of non-algal particles to particulate absorption, so the difference 1 - $a_d:a_p$ specifies the contribution of phytoplankton absorption. The field data from the Southern Ocean show a significant range of the $a_d:a_p$ ratio, with most values indicating the 10%-40% contribution of non-algal absorption to particulate absorption in the blue spectral region at λ = 440 nm. This result implies that phytoplankton absorption is a dominant source of particulate absorption at blue wavelengths. Although there is considerable scatter in the data points, the relatively low contributions of non-algal absorption of ~ 10% (thus the highest contributions of phytoplankton absorption of ~ 90%) were typically observed in waters with high chlorophyll-*a* concentration on the order of a few milligrams per m^{-3}.

For the base model (large black circle), the ratio $a_d:a_p$ is about 0.3 which is consistent with typical field values. The perturbations of the base model with the addition of non-chlorophyll types of particles (colloids, HBAC, organic detritus, or minerals) produce variation only in the values of $a_d:a_p$, and not chlorophyll-*a*. While the addition of minerals has a small effect on the absorption ratio, the models with the addition of organic detritus (yellow circles), organic colloids (brown circles), or heterotrophic bacteria (red circles) at sufficient concentrations suggest that such scenarios of particulate composition can be responsible for relatively high contribution (>40%) of non-algal absorption to the particulate absorption. Such relatively high contributions are observed on rare occasions in our Southern Ocean data set with maximum values over 60%. The second set of models (light green circles in Figure 2.13) indicates a more complex relationship with the addition of phytoplankton to the

base concentrations. The pattern of these phytoplankton models is generally consistent with a tendency for a decrease in a_d:a_p with increasing phytoplankton concentration as parameterized in Figure 2.13 in terms of chlorophyll-*a*. However, these phytoplankton models exhibit a significant scatter around the main trend. The high chlorophyll-*a* models (dark green circles) show one of the lowest values of a_d:a_p < 0.1 among the models, but again these models also show variation in the absorption ratio at a given chlorophyll-*a* concentration. Interestingly, the different perturbations of the base model with increased phytoplankton chlorophyll-*a* concentration show a significant scatter in the modeled data points rather than a well-behaved relationship. This result is to some extent consistent with the significant scatter of field data. Note also that the alternate base models (smaller black circles) point to a possibility for a significant range of Chl values at a given a_d:a_p ratio.

2.4.6. POC versus b_{bp}(555)

The relationship between POC and the particulate backscattering coefficient at 555 nm, b_{bp}(555), is presented in Figure 2.14. This relationship is a component of the 2-step POC retrieval algorithm as described in Chapter 1. As depicted by the field data (grey circles) in Figure 2.14, the relationship between POC and b_{bp}(555) is characterized by considerable scatter of the data points (see also Figure 1.7b and relevant discussion in Chapter 1). As before, the modeled results aid in understanding this variability. The base model (large black circle) is within the central portion of the field data which further supports a very good capability of our modeling approach. The main trend of the POC vs. b_{bp}(555) relationship is shown to be driven largely by

colloids (brown circles), and also to large extent by heterotrophic bacteria (red circles). The inclusion of single-class phytoplankton models (light green circles) and the high chlorophyll-*a* models (dark green circles) has little effect on the $b_{bp}(555)$ but has a pronounced effect on the POC concentration. Therefore, these particle composition scenarios are capable of introducing significant statistical noise around the main overall trend of the relationship. The increased concentrations of organic detritus (yellow circles) also have a strong POC signal with relatively little effect on $b_{bp}(555)$, so these particle assemblages can also produce a statistical noise in the relationship. According to these modeling results, the observed regional differentiation between the Ross Sea data and other Southern Ocean data presented in Figure 1.7b (Chapter 1) are most likely attributable to the differences in the phytoplankton and detrital particle composition between these regions. Figure 2.14 also shows that the addition of minerals (blue circles), which contain no POC but produce strong backscattering, can be a major source of data scatter in the relationship. This result cautions against the use of particulate backscattering as a proxy for POC in waters where significant amount of minerogenic particles might be present, especially in coastal regions. Further reductionist modeling is required for greater understanding of the complexity in the POC vs. $b_{bp}(555)$ relationship and for potential improvements in this type of POC algorithm.

2.4.7. POC versus Backscattering:Aborption ratio

Equation 1.2 in Chapter 1 shows that the product of the blue-to-green band ratio of backscattering coefficient times the green-to-blue ratio of the absorption

coefficient can serve as a good proxy for the blue-to-green ratio of remote-sensing reflectance. This is an important relationship because it indicates that we can use a band ratio of IOP coefficients to approximate the behavior of the band ratio of ocean reflectance. Owing to this approximation we can use our reductionist models to examine how the different particle classes affect the POC ocean color algorithm based on the reflectance band ratio. We recall that such band-ratio algorithms were found in this study to provide the best candidate remote-sensing algorithms for estimating POC in the Southern Ocean (see Chapter 1) and that such a band-ratio algorithm was selected to examine the seasonal and interannual variability in POC within the Southern Ocean from satellite observations (Chapter 3).

Figure 2.15 depicts the relationship between POC and the product of bulk IOP ratios, $[b_b(490)/b_b(555)] \times [a(555)/a(490)]$. The IOP parameter is a proxy for the reflectance band ratio, $R_{rs}(490)/R_{rs}(555)$. The field data (grey circles) show a characteristic non-linear decrease in POC with increasing value of the IOP parameter, which is consistent with the reflectance band-ratio algorithm for estimating POC. Like the other relationships discussed above, the base model (large black circle) is positioned well within the "cloud" of field data. Most importantly, our modeling results show that the main trend of the POC band-ratio algorithm is best explained by phytoplankton models. The "vector" associated with single-class phytoplankton models (light green circles) very closely follows the main trend line of the field data. All other particle composition scenarios considered in our modeling show the potential to introduce scatter of data points in the band-ratio algorithm. This potential for statistical noise is associated not only with the addition of minerals (blue circles),

colloids (brown circles), heterotrophic bacteria (red circles), and organic detritus (yellow circles), but also to some extent with variability in particle composition at high chlorophyll-a concentrations (dark green circles).

2.5. Conclusions

Modeling a bulk population of marine particles based upon the summation of contributions of distinct classes of particles has allowed us to gain insight in the relative effects of each class on bulk POC, chlorophyll-*a*, and optical properties such as particulate backscattering coefficient and the product of band ratios of absorption and backscattering coefficients which serves as a proxy of the blue-to-green band ratio of remote-sensing reflectance. Our modeling results show the power of this approach for learning about the origins of bio-optical variability in the ocean. For example, we show clear decoupling between the particle classes that contribute to backscattering and chlorophyll, and also some degree of decoupling between backscattering and POC. Our model simulations suggest the general significance of colloidal particles and minerals (if present in sufficient amount) to backscattering. The various particle classes including phytoplankton, detritus, bacteria, and colloids can be significant contributors to POC, and their roles depend on the variation in the relative abundance of particle classes. As expected, the increase in the abundance of phytoplankton classes relative to other classes drives the relationship between the bulk chlorophyll and the absorption coefficient in the red part of the spectrum. Changes in other particle classes introduce little noise to this relationship. The POC:Chl ratio is additionally affected by non-phytoplankton POC-bearing particles.

Our model simulations also show that the general trend of POC versus backscattering relationship can be driven largely by colloidal particles and bacteria. The increase in relative abundance of phytoplankton, organic detritus, and minerals (>1 μm in size) introduces mostly statistical noise into this relationship. Importantly, whereas the noise produced by increases in phytoplankton and detritus is associated with significant change in POC accompanied by relatively small change in backscattering, the opposite effect is produced by minerals which increase backscattering without a change in POC. These findings are essential for the interpretation of the performance of POC algorithms that use the backscattering coefficient. Finally, our example models show the roles played by different particle classes in the POC algorithm based on the blue-to-green ratio of ocean reflectance. Here the major particles that drive the relationship are phytoplankton classes. Colloids, bacteria, and detritus all produce noise that propagates in a similar direction. Minerals produce noise in a clearly different direction. These results highlight a unique value of the presented analysis and point to a need for mechanistic approaches in the development of further improvements in optical remote sensing of POC or other biochemically important seawater constituents.

2.6. Figures

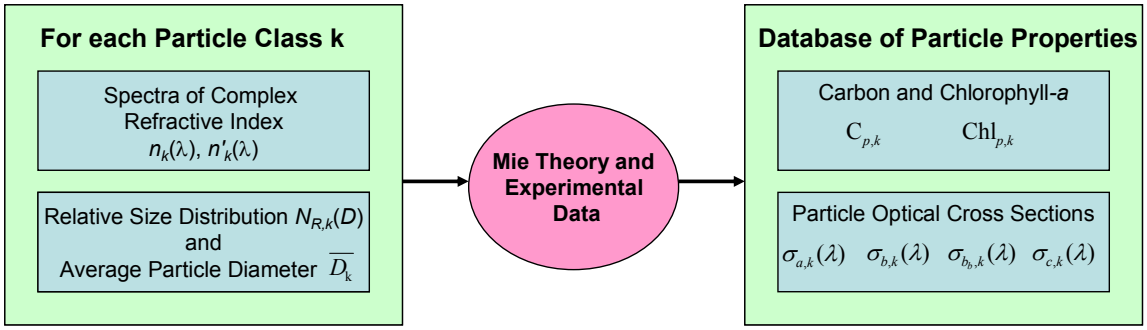

Figure 2.1. Schematic representation of the calculation of the database of properties for particle classes. The inputs to the Mie theory and empirical models are the spectra of complex index of refraction relative to water, relative particle size distribution, and the average particle diameter for the class. For each particle class, the inputs generate class carbon and chlorophyll-*a* concentration per particle and the particle optical cross sections.

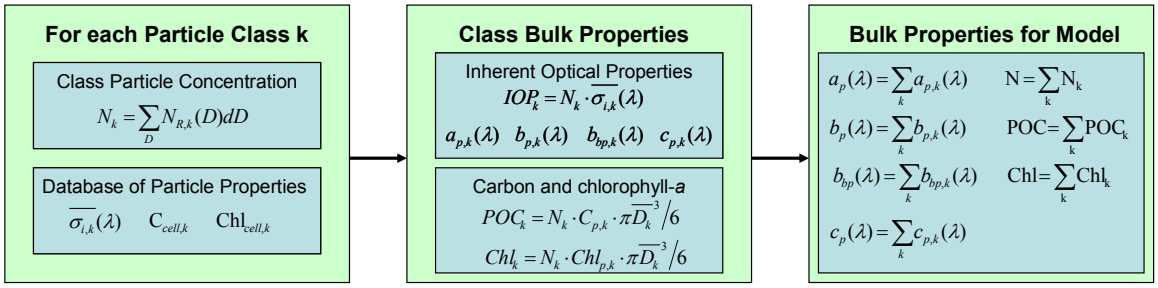

Figure 2.2. Flow chart to calculate bulk properties for a given model from single particle class properties. The inputs are the class particle concentration for each class included in the model and the database of optical and biochemical particle properties. For each particle class, the inputs generate class bulk properties of IOPs and class POC and chlorophyll-*a* concentrations. The sum of all class properties is then the bulk properties for the model.

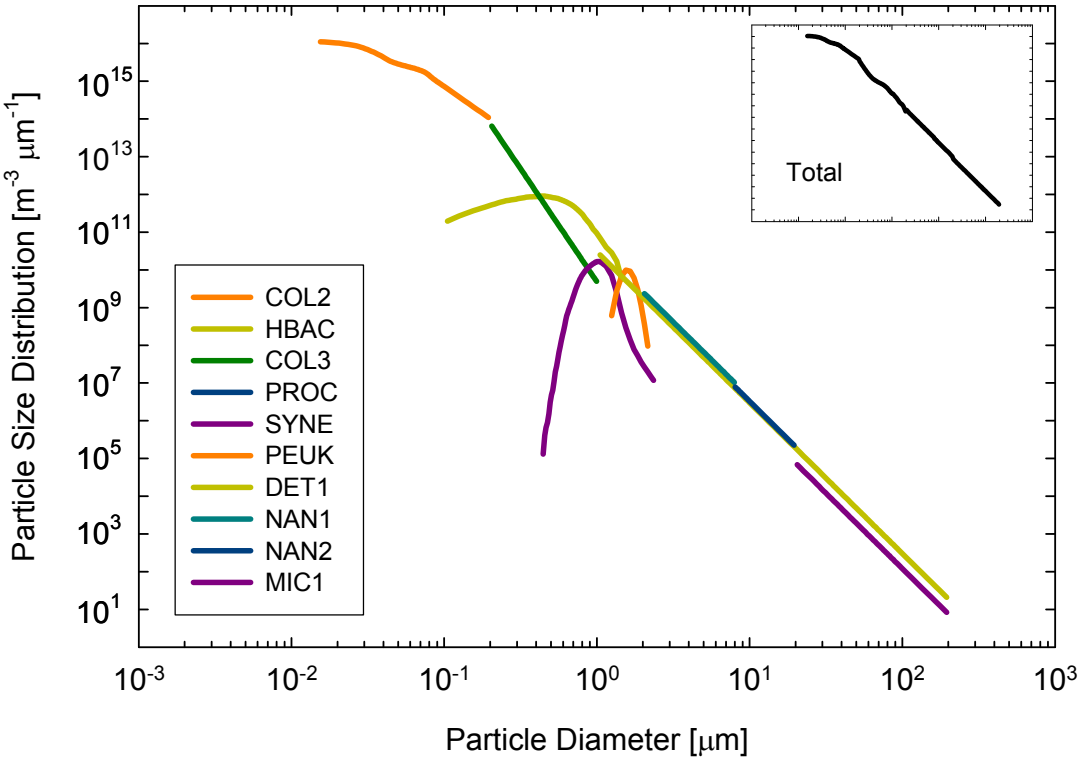

Figure 2.3. Density function of particle size distribution (PSD) for the base model. The contributions of each particle class are indicated as explained in the figure legend. The total PSD is indicated in the inset, and for the most part it is consistent with a Junge type power law $\sim D^{-4}$.

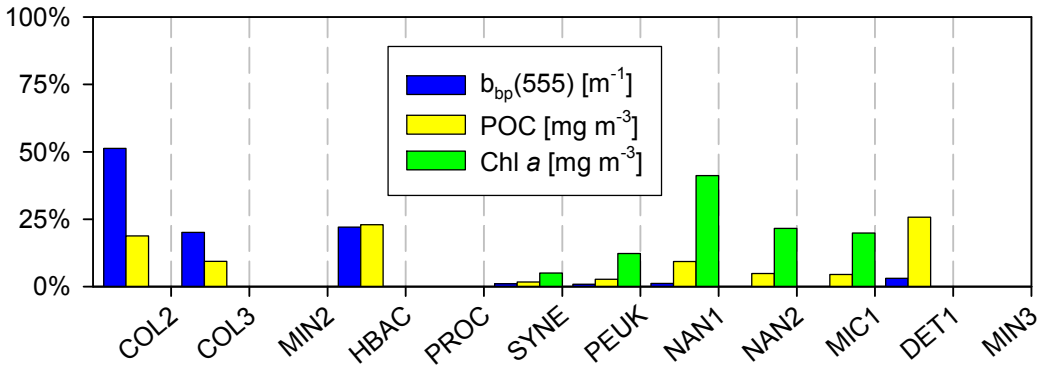

Figure 2.4. Relative contribution of each particle class to the bulk properties of b_{bp}(555), POC, and chlorophyll-*a* for the base model.

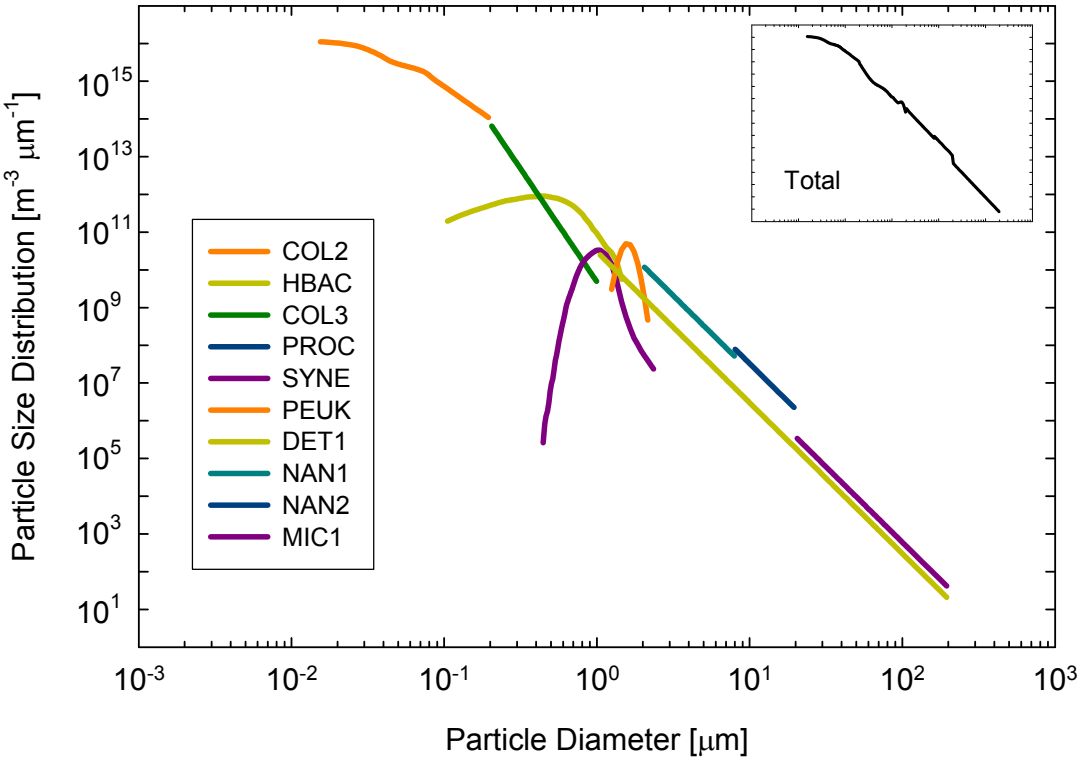

Figure 2.5. Density function of particle size distribution for the high chlorophyll-*a* multi-class phytoplankton bloom model. The contributions of each particle class are indicated as explained in the figure legend. The total PSD is indicated in the inset.

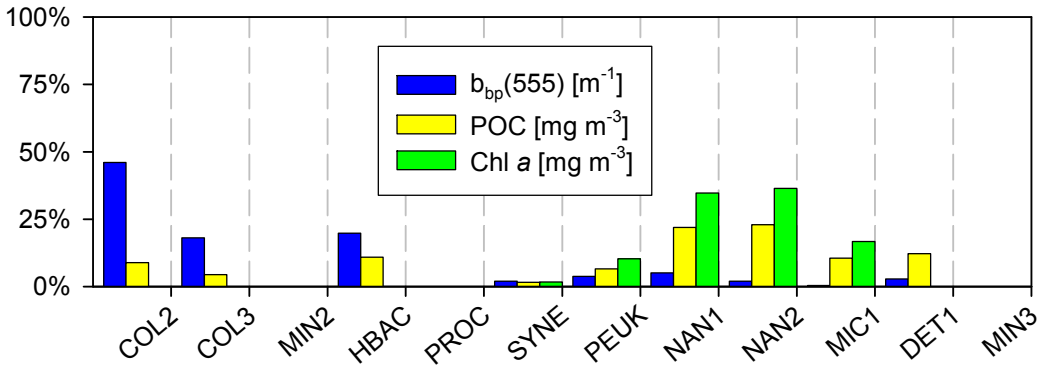

Figure 2.6. Relative contribution of each particle class to the bulk properties of $b_{bp}(555)$, POC, and chlorophyll-*a* for the high chlorophyll multi-class phytoplankton bloom model.

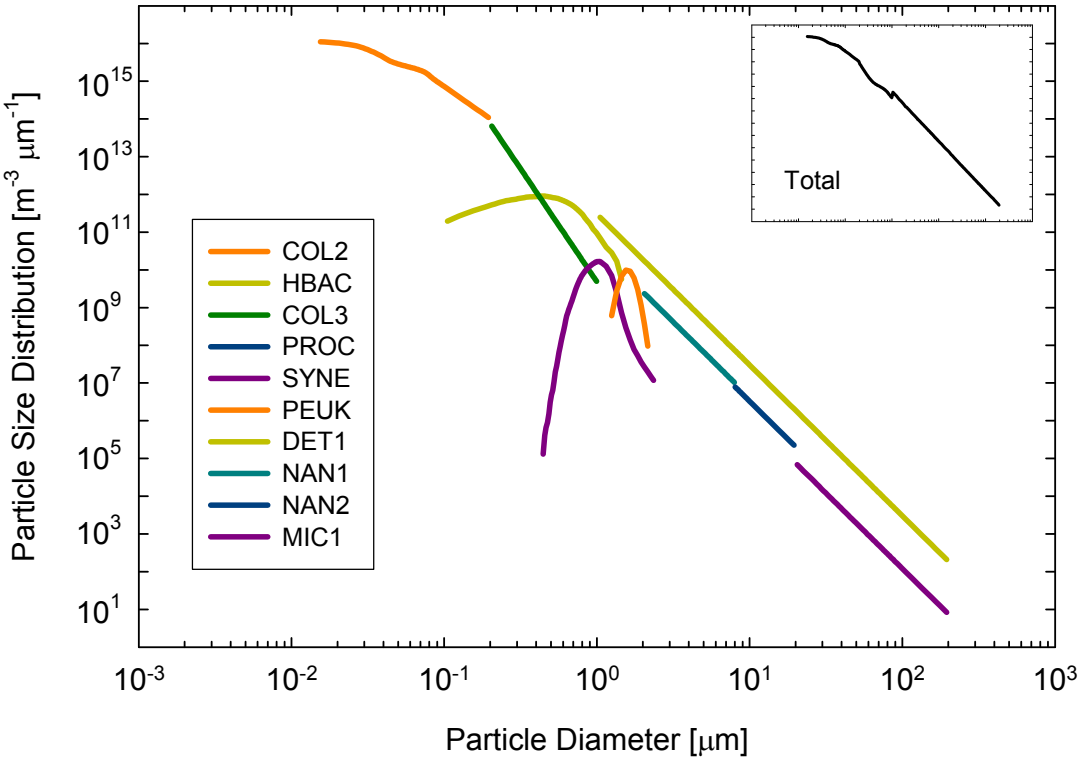

Figure 2.7. Density function of particle size distribution for the 10-fold increase in detritus model. The contributions of each particle class are indicated as explained in the figure legend. The total PSD is indicated in the inset.

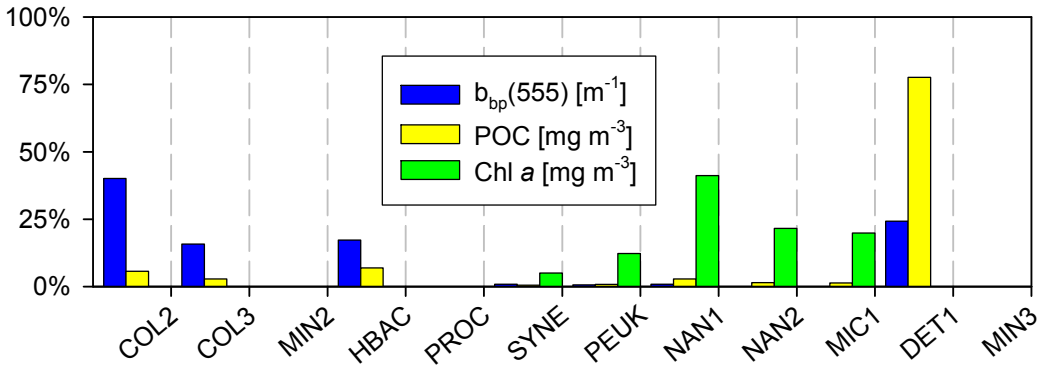

Figure 2.8. Relative contribution of each particle class to the bulk properties of b_{bp}(555), POC, and chlorophyll-*a* for the detritus-enriched model.

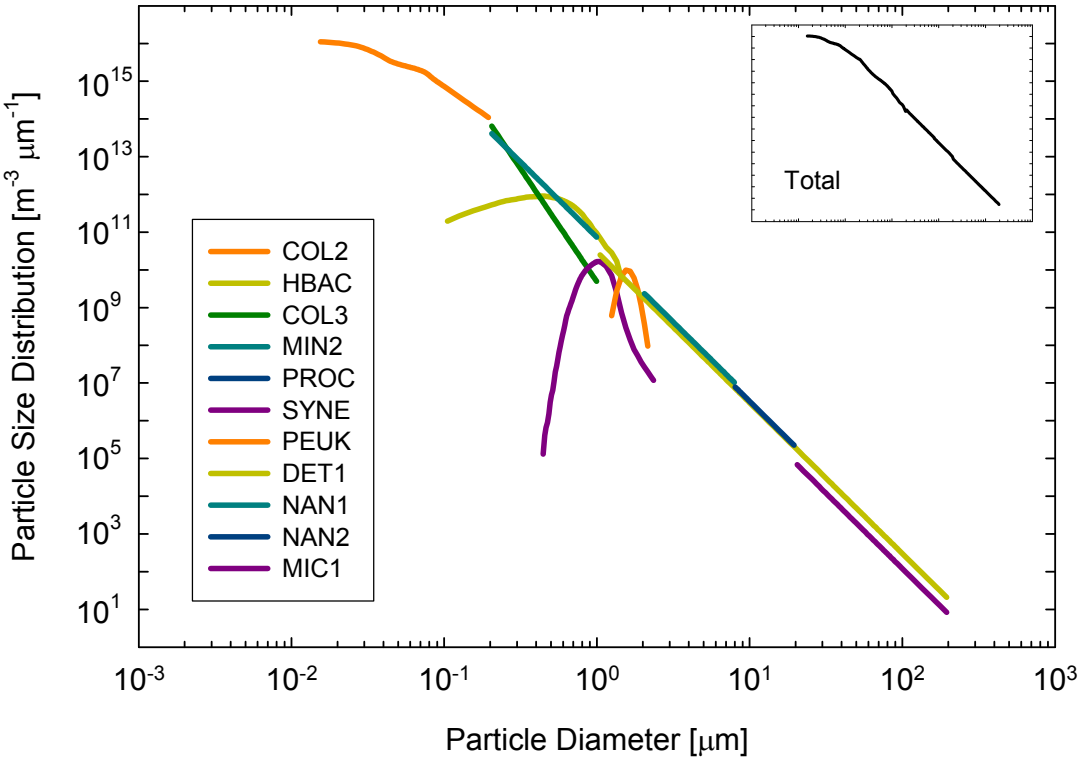

Figure 2.9. Density function of particle size distribution for the addition of small minerals model. The contributions of each particle class are indicated as explained in the figure legend. The total PSD is indicated in the inset.

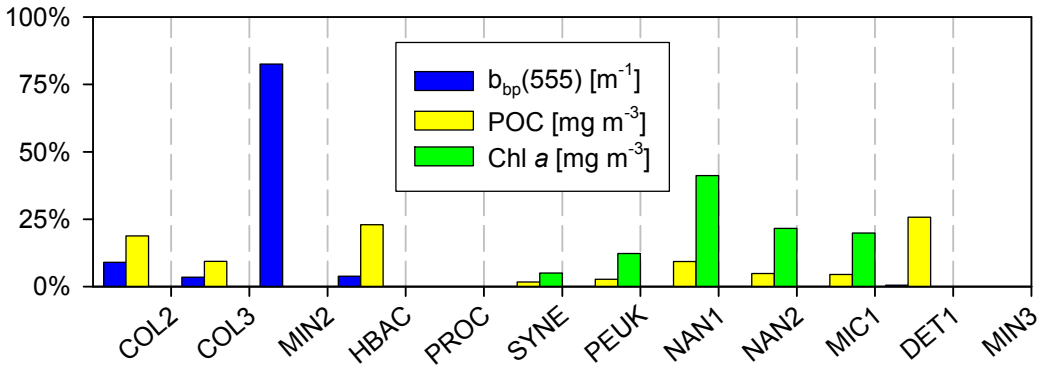

Figure 2.10. Relative contribution of each particle class to the bulk properties of b_{bp}(555), POC, and chlorophyll-*a* for small minerals-enriched model.

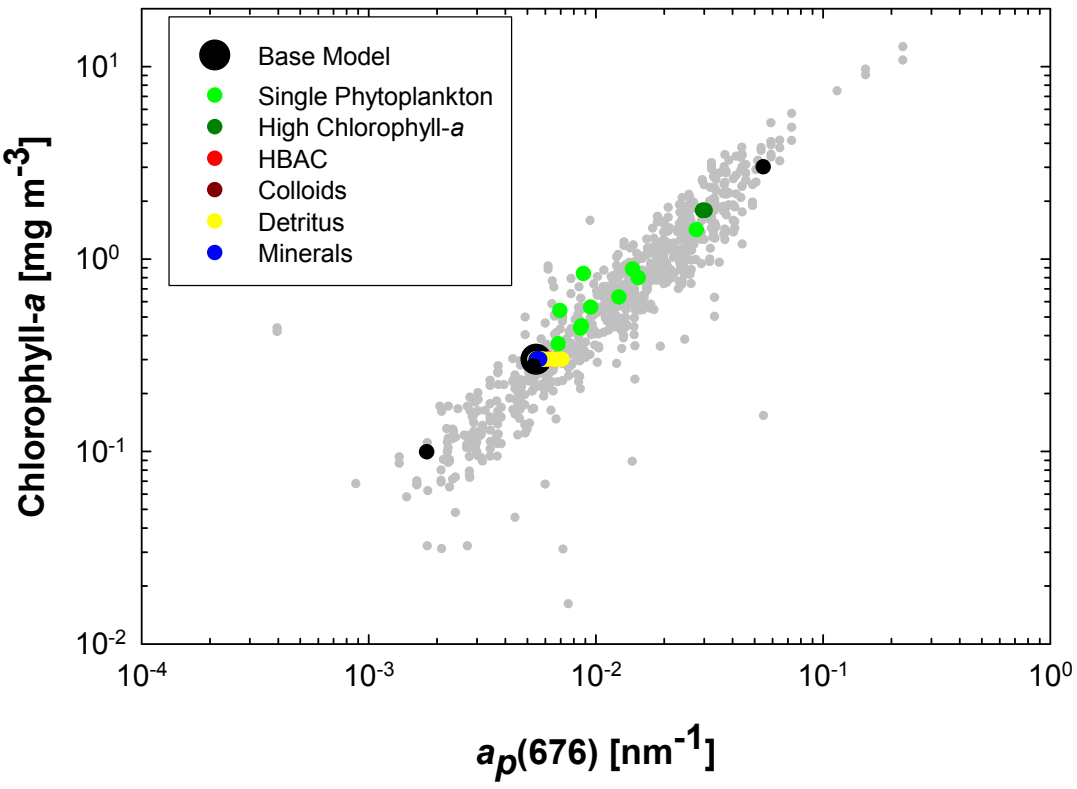

Figure 2.11. Comparison of field data and model results for the relationship between the bulk chlorophyll-*a* concentration and the bulk particulate absorption coefficient $a_p(676)$. Field data are indicated as grey circles. The base model is shown as the large black circle, and the smaller black circles correspond to the alternate base models. Additional models are represented by colored symbols as indicated in the legend.

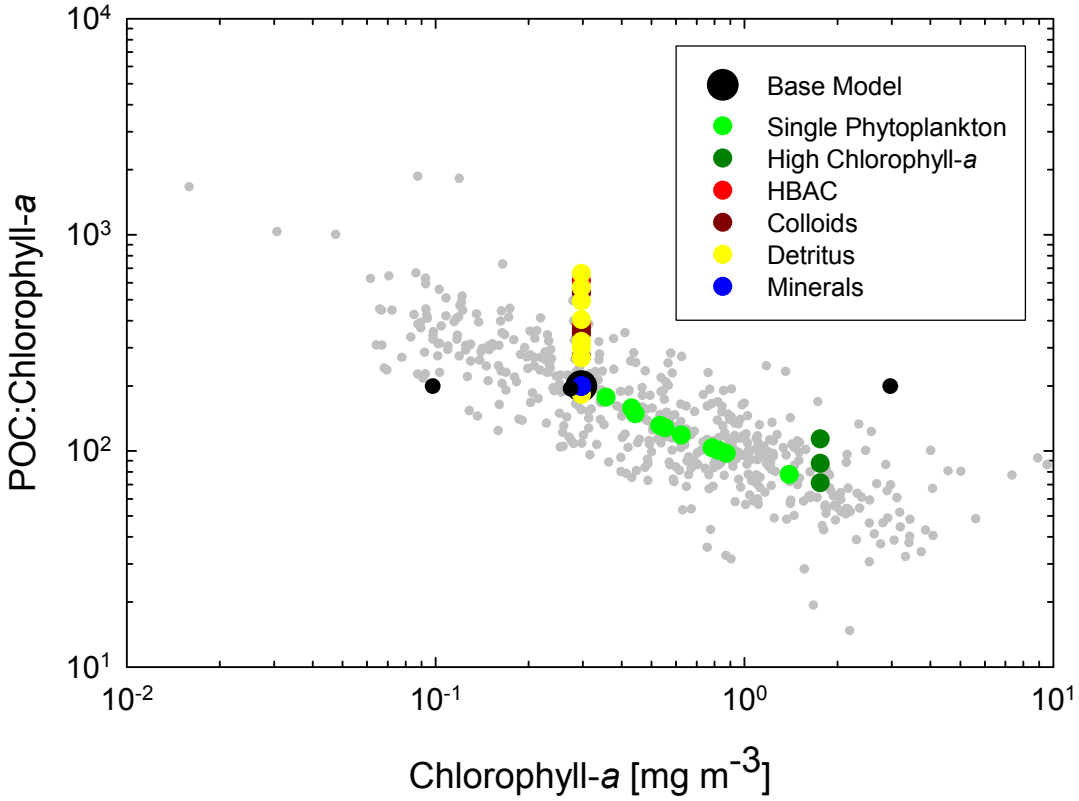

Figure 2.12. Comparison of field data and model results for the relationship between the bulk POC:Chl ratio and the bulk chlorophyll-*a* concentration. Field data are indicated as grey circles. The base model is shown as the large black circle, and the smaller black circles correspond to the alternate base models. Additional models are represented by colored symbols as indicated in the legend.

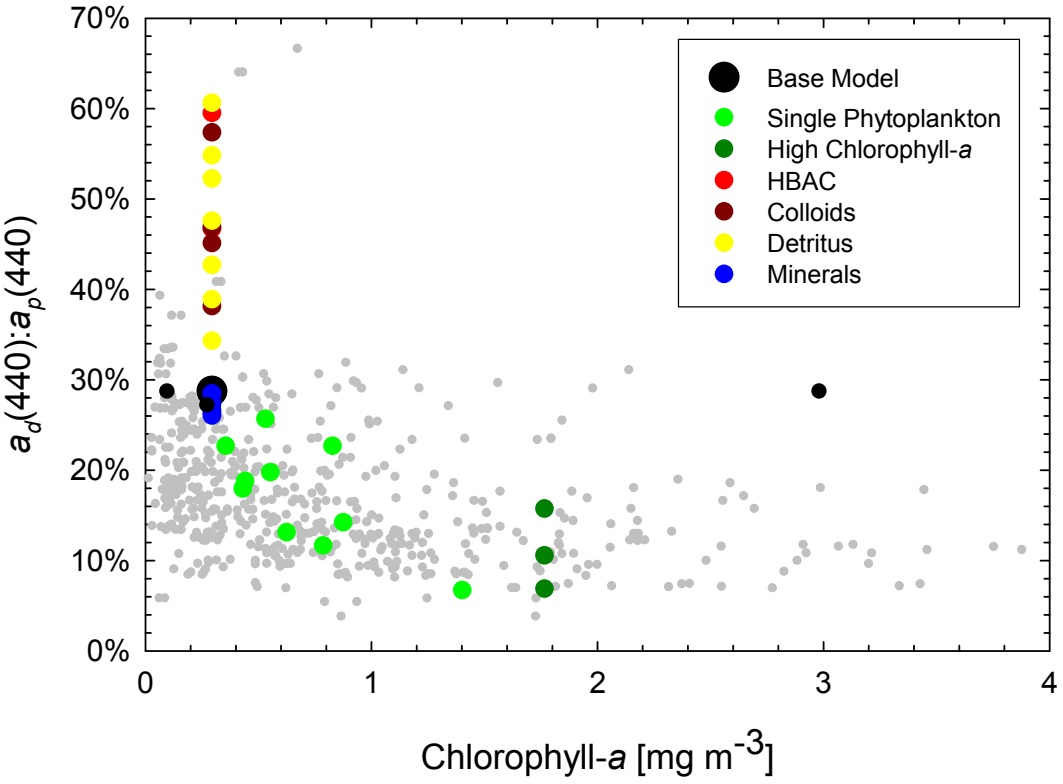

Figure 2.13. Comparison of field data and model results for the relationship between the ratio of bulk non-algal (a_d) to bulk particulate absorption (a_p) coefficients at 440 nm as a function of bulk chlorophyll-*a* concentration. Field data are indicated as grey circles. The base model is shown as the large black circle, and the smaller black circles correspond to the alternate base models. Additional models are represented by colored symbols as indicated in the legend.

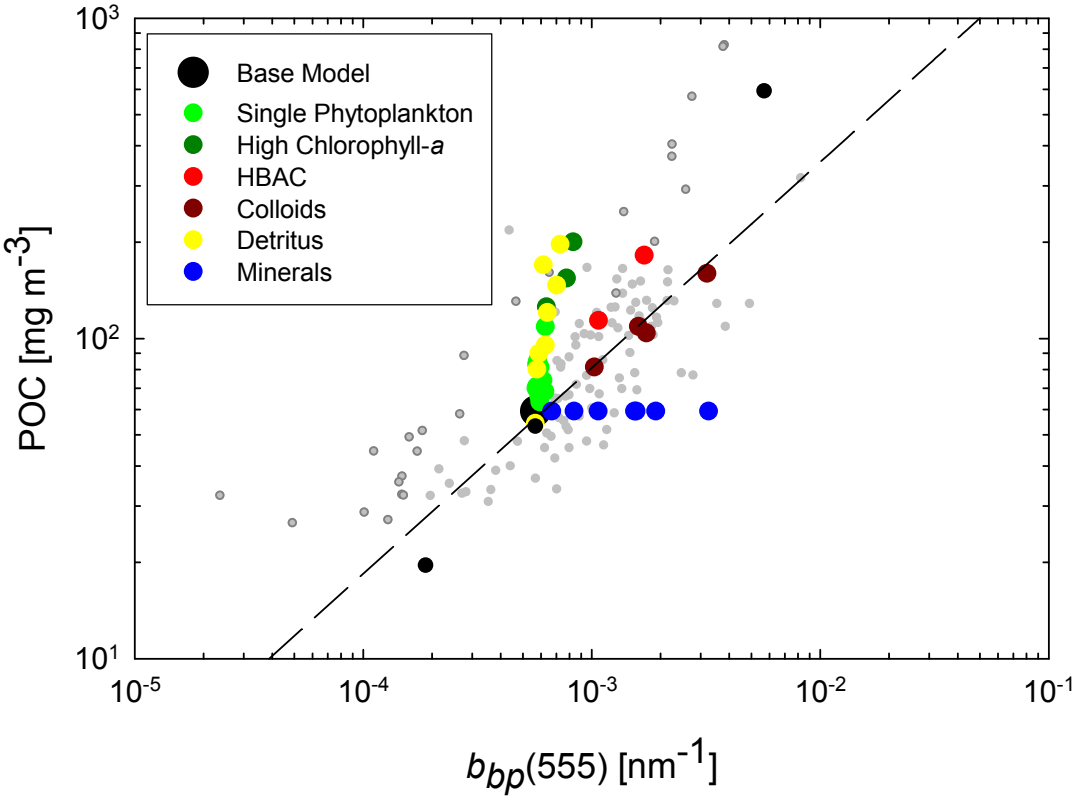

Figure 2.14. Comparison of field data and model results for the relationship between the POC concentration and the particulate backscattering coefficient at 555nm, $b_{bp}(555)$. Field data are indicated as grey circles. Field data from the Ross Sea are indicated by the grey circles with darker border. The base model is shown as the large black circle, and the smaller black circles correspond to the alternate base models. Additional models are represented by colored symbols as indicated in the legend. The dashed line represents the best fit to the field data (excluding the Ross Sea data).

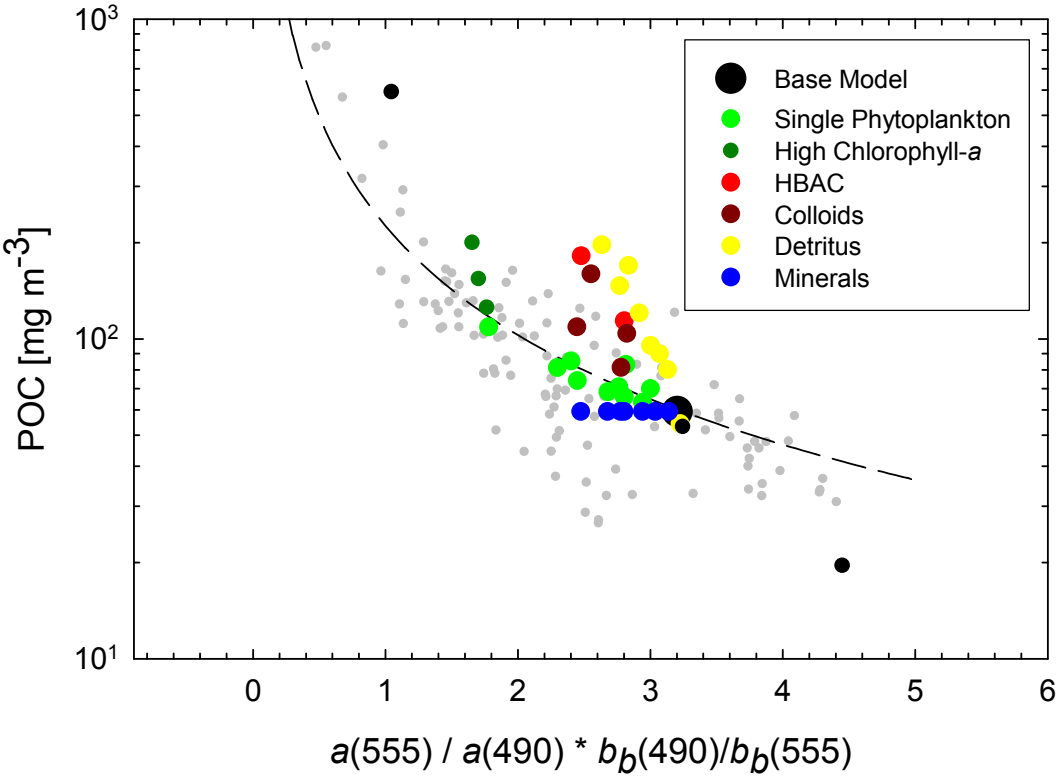

Figure 2.15. Comparison of field data and model results for the relationship between the bulk POC concentration and the inherent optical property (IOP) parameter, [b_b(490)/b_b(555)] x [a(555)/a(490)], which represents a proxy for the ocean reflectance band ratio, R_{rs}(490)/R_{rs}(555). Field data are indicated as grey circles. The base model is shown as the large black circle, and the smaller black circles correspond to the alternate base models. Additional models are represented by colored symbols as indicated in the legend. The dashed line represents the best fit to the field data. The presented relationships in the data are representative for other combinations of the blue and green wavebands such as 443 and 555 which were identified as the best pair of bands for the POC algorithm discussed in Chapter 1.

2.7. Tables

Table 2.1. Listing of the 21 unique particle classes available for modeling. Values for the average equivalent spherical diameter $\bar{D}_k$, the real part of the refractive index at 550 nm $n_k(550)$, imaginary part of the refractive index at 676 nm $n_k'(676)$, intracellular (intraparticle) carbon concentration $C_{p,k}$ and intracellular chlorophyll-*a* concentration $Chl_{p,k}$ are shown for each particle class. The values of $C_{p,k}$ were set to zero for mineral particles. Similarly, the values of $Chl_{p,k}$ were to zero for HBAC, MIN-1MIN4, DET1-DET5, and COL1-COL3.

Label	Particle Class	$\bar{D}_k$ (um)	$n_k(650)$	$n_k'(676)$ x 10^3	$C_{p,k}$ (mg m^{-3})	$Chl_{p,k}$ (mg m^{-3})
HBAC	Heterotrophic Bacteria	0.50	1.05	-	2.39E+08	-
PROC	Generic Prochlorophyte	0.65	1.05	10.03	2.19E+08	1.22E+07
SYNE	Generic *Synechococcus*;	1.04	1.05	2.98	2.24E+08	3.38E+06
SYMA	Generic phycocyanin-rich picophytoplankton	1.40	1.06	2.77	2.43E+08	3.13E+06
NAN1	Small nanophytoplankton	2.86	1.04	3.54	1.82E+08	4.08E+06
NAN2	Large nanophytoplankton	10.78	1.04	3.54	1.82E+08	4.08E+06
MIC1	Microphytoplankton (1)	29.75	1.04	3.54	1.82E+08	4.08E+06
MIC2	Microphytoplankton (2)	27.38	1.04	3.54	1.82E+08	4.08E+06
PEUK	Picoeukaryotes	1.61	1.04	3.54	1.82E+08	4.08E+06
DET1	Detritus (1)	1.50	1.04	0.083	1.82E+08	-
DET2	Detritus (2)	1.50	1.04	0.083	1.82E+08	-
DET3	Detritus (3)	1.77	1.04	0.083	1.82E+08	-
DET4	Detritus (4)	1.51	1.04	0.083	1.82E+08	-
DET5	Detritus (5)	1.74	1.04	0.083	1.82E+08	-
MIN1	Very small minerals	0.02	1.16	0.083	-	-
MIN2	Small minerals	0.29	1.16	0.083	-	-
MIN3	Large minerals (1)	1.50	1.16	0.083	-	-
MIN4	Large minerals (2)	1.50	1.16	0.083	-	-
COL1	Small colloids (1)	0.05	1.04	0.083	1.82E+08	-
COL2	Small colloids (2)	0.05	1.04	0.083	1.82E+08	-
COL3	Large colloids	0.25	1.04	0.083	1.82E+08	-

Table 2.2. Values for the smallest and largest diameter and the basis for the size distribution are shown for each particle class described in Table 2.1. The size distribution is either based on measured data as indicated by reference or a modeled power function.

Label	Particle Class	smallest diameter (μm)	largest diameter (μm)	Particle Size Distribution Source
HBAC	Heterotrophic Bacteria	0.1	1.5	data (Stramski et al.; 2001)
PROC	Generic Prochlorophyte	0.25	1.12	data (Stramski et al., 2001)
SYNE	Generic *Synechococcus*;	0.44	2.45	data (Stramski et al., 2001)
SYMA	Generic phycocyanin-rich picophytoplankton	0.7	2.26	data (Stramski et al., 2001)
NAN1	Small nanophytoplankton	2	8	D^{-4} (this study)
NAN2	Large nanophytoplankton	8	20	D^{-4} (this study)
MIC1	Microphytoplankton (1)	20	200	D^{-4} (this study)
MIC2	Microphytoplankton (2)	20	200	D^{-4} (this study)
PEUK	Picoeukaryotes	1.2	2.2	D^{-4} (this study)
DET1	Detritus (1)	1	200	D^{-4} (this study)
DET2	Detritus (2)	1	200	D^{-4}, D<=10um; $D^{-4.7}$, D>10um (this study)
DET3	Detritus (3)	1	200	$D^{-3.3}$ (this study)
DET4	Detritus (4)	1	200	D^{-4}, D<=10um; $D^{-3.3}$, D>10um (this study)
DET5	Detritus (5)	1	200	$D^{-3.3}$, D<=10um; D^{-4}, D>10um (this study)
MIN1	Very small minerals	0.01	0.2	D^{-4} (this study)
MIN2	Small minerals	0.2	1	D^{-4} (this study)
MIN3	Large minerals (1)	1	200	D^{-4} (this study)
MIN4	Large minerals (2)	1	200	D^{-4}, D<=10um; $D^{-4.7}$, D>10um (this study)
COL1	Small colloids (1)	0.015	0.2	average data (Stramski and Wozniak, 2005)
COL2	Small colloids (2)	0.015	0.2	average data (Stramski and Wozniak, 2005) with smoothing
COL3	Large colloids	0.2	1	data (Stramski and Wozniak, 2005) D^{-6}

Table 2.3. Definition of base model. The base model consists of 14 particles classes (4 of which have 0 contribution) representative of particles classes found within the Southern Ocean. Included in the model are the phytoplankton classes, non-living organic colloids and detritus, minerals, and bacteria. For each class, the total particle concentration (N_k) of the class is indicated.

Label	**Particle Class**	**Total Particle Concentration, N_k (m^{-3})**
MIN1	Very small minerals	--
COL2	Small colloids (2)	3.50E+14
HBAC	Heterotrophic Bacteria	5.00E+11
COL3	Large colloids	3.00E+12
MIN2	Small minerals	--
PROC	Generic Prochlorophyte	--
SYNE	Generic *Synechococcus*;	7.00E+09
SYMA	Generic phycocyanin-rich picophytoplankton	--
PEUK	Picoeukaryotes	4.00E+09
DET1	Detritus (1)	1.00E+10
MIN3	Large minerals (1)	--
NAN1	Small nanophytoplankton	1.70E+09
NAN2	Large nanophytoplankton	2.00E+07
MIC1	Microphytoplankton (1)	5.00E+05

Table 2.4. Listing of all (38) particle models. Each model consists of a selection of particle classes defined in Table 2.2. The models are divided into 7 groups defined by general characteristics. The highlighted models are discussed in the results section.

Model Group (Count)	ID	Model Description
Base Model (1)	I	Representative of Southern Ocean
Alternate Base Models (3)		
	I	10x the concentration of each particle class in base model
	II	1/3x the concentration of each particle class in base model
	III	Base model with 1x the MIC2 concentration
Single-Class Phytoplankton Models (10)		
	I	Base model + 5x the SYNE concentration
	II	Base model + 5x the PEUK concentration
	III	Base model + 5x the NAN1 concentration
	IV	Base model + 5x the NAN2 concentration
	V	Base model + 5x the MIC1 concentration
	I*	Base model + 10x the SYNE concentration
	II*	Base model + 10x the PEUK concentration
	III*	Base model + 10x the NAN1 concentration
	IV*	Base model + 10x the NAN2 concentration
	V*	Base model + 10x the MIC1 concentration
High Chlorophyll-*a* Models (3)		
	I	Base model + high chlorophyll-*a* associated classes
	II	Base model + high chlorophyll-*a* associated classes
	III	Base model + high chlorophyll-*a* associated classes
HBAC Models (2)		
	I	Base model + 5x HBAC concentration
	II	Base model + 10x HBAC concentration
Colloid Models (4)		
	I	Base model + 5x the COL2 concentration
	II	Base model + 10x the COL2 concentration
	III	Base model + 5x the COL3 concentration
	IV	Base model + 10x the COL3 concentration
Detritus Models (8)		
	I	Base model + 5x the DET1 concentration
	II	Base model + 10x the DET1 concentration
	III	Base model + 1x the DET2 concentration (replace DET1)
	IV	Base model + 5x the DET2 concentration (replace DET1)
	V	Base model + 10x the DET2 concentration (replace DET1)
	VI	Base model + 1x the DET3 concentration (replace DET1)
	VII	Base model + 1x the DET4 concentration (replace DET1)
	VIII	Base model + 1x the DET5 concentration (replace DET1)
Mineral Models (7)		
	I	Base model + small minerals at 0.1x COL3
	II	Base model + small minerals at 0.5x COL3
	III	Base model + small minerals at 1.0x COL3
	IV	Base model + large minerals at 0.1x DET1
	V	Base model + large minerals at 0.5x DET1
	VI	Base model + large minerals at 1.0x DET1
	VII	Base model + large minerals at 1.0x DET2

Table 2.5. Alternate base model definitions. The alternate base models are scaled versions of the base model presented in Table 2.3. Model I is 1/3x the particle concentration for each class. Model II is 10x the particle concentration for each class. Model III replaces the PSD1 for microphytoplankton (MIC1) with the alternate PSD2 (MIC2), the concentration is the same.

Label	I	II	III
MIN1	-	-	-
COL2	1/3x	10x	1x
HBAC	1/3x	10x	1x
COL3	1/3x	10x	1x
MIN2	-	-	-
PROC	-	-	-
SYNE	1/3x	10x	1x
SYMA	-	-	-
PEUK	1/3x	10x	1x
DET1	1/3x	10x	1x
MIN3	-	-	-
NAN1	1/3x	10x	1x
NAN2	1/3x	10x	1x
MIC1(2)	1/3x	10x	1x PSD2

Table 2.6. Definitions of single-class phytoplankton models. Each model indicated has an additional single phytoplankton class added to the base model at either 5x or 10x (indicated by an * in the model ID) the particle concentration in the base model.

Label	I(*)	II(*)	III(*)	IV(*)	V(*)
MIN1	-	-	-	-	-
COL2	1x	1x	1x	1x	1x
HBAC	1x	1x	1x	1x	1x
COL3	1x	1x	1x	1x	1x
MIN2	-	-	-	-	-
PROC	-	-	-	-	-
SYNE	5x (10x)	1x	1x	1x	1x
SYMA	-	-	-	-	-
PEUK	1x	5x (10x)	1x	1x	1x
DET1	1x	1x	1x	1x	1x
MIN3	-	-	-	-	-
NAN1	1x	1x	5x (10x)	1x	1x
NAN2	1x	1x	1x	5x (10x)	1x
MIC1	1x	1x	1x	1x	5x (10x)

Table 2.7. Definitions of models created to contain high chlorophyll-*a* concentrations. Each model indicated has multiple phytoplankton classes, colloids, and detritus added to the base model at the indicated scaling of the particle concentration in the base model. The phytoplankton classes could represent the living component in a bloom condition whereas the colloids and detritus are the resultant non-living organic matter. The highlighted model (I) is discussed in more detail in the results section.

Label	**I**	**II**	**III**
MIN1	-	-	-
COL2	1x	1x	1x
HBAC	1x	2x	2x
COL3	1x	1x	1x
MIN2	-	-	-
PROC	-	-	-
SYNE	1x	1x	1x
SYMA	2x	2x	2x
PEUK	5x	5x	5x
DET1	1x	2x	5x
MIN3	-	-	-
NAN1	5x	5x	5x
NAN2	10x	10x	10x
MIC1	5x	5x	5x

Table 2.8. Definitions of models created to contain high concentrations of heterotrophic bacteria (HBAC). Models I and II contain 5x and 10x the concentration of HBAC found in the base model respectively.

Label	**I**	**II**
MIN1	-	-
COL2	1x	1x
HBAC	5x	10x
COL3	1x	1x
MIN2	-	-
PROC	-	-
SYNE	1x	1x
SYMA	1x	1x
PEUK	1x	1x
DET1	1x	1x
MIN3	-	-
NAN1	1x	1x
NAN2	1x	1x
MIC1	1x	1x

Table 2.9. Definitions of models containing increased concentrations of colloids. The 4 models indicated in the table increase the concentration of colloids in the base model. Models I and II increase the small colloids (COL2) concentration of the base model by 5x and 10x respectively. Models III and IV add 5x and 10x more large colloids (COL3) to the base model respectively.

Label	**I**	**II**	**III**	**IV**
MIN1	-	-	-	-
COL2	5x)	10x	1x	1x
HBAC	1x	1x	1x	1x
COL3	1x	1x	10x	10x
MIN2	-	-	-	-
PROC	-	-	-	-
SYNE	1x	1x	1x	1x
SYMA	-	-	-	-
PEUK	1x	1x	1x	1x
DET1	1x	1x	1x	1x
MIN3	-	-	-	-
NAN1	1x	1x	1x	1x
NAN2	1x	1x	1x	1x
MIC1	1x	1x	1x	1x

Table 2.10. Definition of the organic detritus models. The 8 models have additional detritus added to the base model. Models I and II add an additional 5x and 10x detritus to the base model with the original particle size distribution (DET1). Models III-V replace the PSD for detritus in the base model with an alternate PSD for detritus (DET2) at concentrations of 1x, 5x, and 10x respectively of the concentration within the base model. Models VI-VIII replace the PSD for detritus (DET1) in the base model with an alternate PSDs for detritus (DET3, DET4, DET5) at the same 1x concentration of the base model. The highlighted model (II) is discussed in the results section.

Label	**I**	**II**	**III**	**IV**	**V**	**VI,VII,VIII**
MIN1	-	-	-	-	-	-
COL2	1x	1x	1x	1x	1x	1x
HBAC	1x	1x	1x	1x	1x	1x
COL3	1x	1x	1x	1x	1x	1x
MIN2	-	-	-	-	-	-
PROC	-	-	-	-	-	-
SYNE	1x	1x	1x	1x	1x	1x
SYMA	-	-	-	-	-	-
PEUK	1x	1x	1x	1x	1x	1x
DET1	5x	10x	1x (DET2)	5x (DET2)	10x (DET2)	1x (DET3,4,5)
MIN3	-	-	-	-	-	-
NAN1	1x	1x	1x	1x	1x	1x
NAN2	1x	1x	1x	1x	1x	1x
MIC1	1x	1x	1x	1x	1x	1x

Table 2.11. Definitions of the mineral models. The 7 models add minerals to the base model. Model I has the addition of very small minerals (MIN1) at 10x the particle concentration of the small colloids (COL2) found in the base model. Models II-IV add small minerals (MIN2) to the base model at 0.1x, 0.5x and 1x the particle concentration of large colloids (COL3) found in the base model. Models V-VII add large minerals (MIN3) to the base model at 0.1x, 0.5x and 1x the particle concentration of detritus (DET1) found in the base model. Model VII adds large minerals to the base model with the alternate PSD (MIN4) at 1x the concentration of detritus (DET1) in the base model. The highlighted model (IV) is discussed in the results section.

Label	**I**	**II**	**III**	**IV**	**V**	**VI**	**VII**	**VII**
MIN1	10x (COL2)	-	-	-	-	-	-	-
COL2	1x	1x	1x	1x	1x	1x	1x	1x
HBAC	1x	1x	1x	1x	1x	1x	1x	1x
COL3	1x	1x	1x	1x	1x	1x	1x	1x
MIN2	-	1/10x (COL3)	1/2x (COL3)	1x (COL3)	-	-	-	-
PROC	-	-	-	-	-	-	-	-
SYNE	1x	1x	1x	1x	1x	1x	1x	1x
SYMA	-	-	-	-	-	-	-	-
PEUK	1x	1x	1x	1x	1x	1x	1x	1x
DET1	1x	1x	1x	1x	1x	1x	1x	1x
MIN3	-	-	-	-	1/10x (DET1)	1/2x (DET1)	1x (DET1)	1x (DET1) (MIN4)
NAN1	1x	1x	1x	1x	1x	1x	1x	1x
NAN2	1x	1x	1x	1x	1x	1x	1x	1x
MIC1	1x	1x	1x	1x	1x	1x	1x	1x

Table 2.12. Results for the base model. The IOPs and POC and Chl concentrations, are indicated for each particle class k within the model as well as the bulk results for the model as a whole.

	N_k	$a_{p,k}(676)$	$b_{p,k}(555)$	$b_{bp,k}(555)$	$\frac{a_k(555)}{a_k(490)} * \frac{b_{b,k}(490)}{b_{b,k}(555)}$	POC_k	Chl_k
Units	[m^{-3}]	[m^{-1}]	[m^{-1}]	[m^{-1}]	[unitless]	[mg m^{-3}]	[mg m^{-3}]
Bulk	**3.54E+14**	**5.50E-03**	**8.12E-02**	**5.73E-04**	**3.21**	**58.972**	**0.298**
MIN1	-	-	-	-	-	-	-
COL2	3.50E+14	1.28E-04	9.00E-04	2.94E-04	-	11.100	-
HBAC	5.00E+11	8.60E-05	2.12E-02	1.26E-04	-	13.556	-
COL3	3.00E+12	6.50E-05	2.20E-03	1.16E-04	-	5.499	-
MIN2	-	-	-	-	-	-	-
PROC	-	-	-	-	6.65	-	-
SYNE	7.00E+09	3.48E-04	2.23E-03	6.26E-06	5.61	0.995	0.015
SYMA	-	-	-	-	6.65	-	-
PEUK	4.00E+09	8.04E-04	3.86E-03	4.79E-06	5.34	1.631	0.037
DET1	1.00E+10	1.82E-04	2.58E-02	1.78E-05	-	15.206	-
MIN3	-	-	-	-	-	-	-
NAN1	1.70E+09	2.49E-03	2.07E-02	6.54E-06	4.61	5.477	0.123
NAN2	2.00E+07	1.02E-03	3.75E-03	1.26E-06	5.18	2.870	0.064
MIC1	5.00E+05	3.75E-04	5.89E-04	5.24E-07	5.41	2.636	0.059

Table 2.13. Results for the example high chlorophyll-*a* model (model I). The IOPs and POC and Chl concentrations, are indicated for each particle class k within the model as well as the bulk results for the model as a whole.

	N_k	$a_{p,k}(676)$	$b_{p,k}(555)$	$b_{bp,k}(555)$	$\frac{a_k(555)}{a_k(490)} * \frac{b_{b,k}(490)}{b_{b,k}(555)}$	POC_k	Chl_k
Units	[m^{-3}]	[m^{-1}]	[m^{-1}]	[m^{-1}]	[unitless]	[mg m^{-3}]	[mg m^{-3}]
Bulk	**3.54E+14**	**2.97E-02**	**2.18E-01**	**6.38E-04**	**1.77**	**124.777**	**1.769**
MIN1	-	-	-	-	-	-	-
COL2	3.50E+14	1.28E-04	9.00E-04	2.94E-04	-	11.100	-
HBAC	5.00E+11	8.60E-05	2.12E-02	1.26E-04	-	13.556	-
COL3	3.00E+12	6.50E-05	2.20E-03	1.16E-04	-	5.499	-
MIN2	-	-	-	-	-	-	-
PROC	-	-	-	-	6.65	-	-
SYNE	1.40E+10	6.96E-04	4.46E-03	1.25E-05	5.28	1.990	0.030
SYMA	-	-	-	-	6.65	-	-
PEUK	2.00E+10	4.02E-03	1.93E-02	2.40E-05	4.15	8.157	0.183
DET1	1.00E+10	1.82E-04	2.58E-02	1.78E-05	-	15.206	-
MIN3	-	-	-	-	-	-	-
NAN1	8.50E+09	1.25E-02	1.04E-01	3.27E-05	2.94	27.386	0.615
NAN2	2.00E+08	1.02E-02	3.75E-02	1.26E-05	3.27	28.700	0.645
MIC1	2.50E+06	1.88E-03	2.95E-03	2.62E-06	4.64	13.182	0.296

Table 2.14. Results for the example detritus-enriched model (model II, 10x DET1). The IOPs and POC and Chl concentrations, are indicated for each particle class k within the model as well as the bulk results for the model as a whole.

	N_k	$a_{p,k}(676)$	$b_{p,k}(555)$	$b_{bp,k}(555)$	$\frac{a_k(555)}{a_k(490)} * \frac{b_{b,k}(490)}{b_{b,k}(555)}$	POC_k	Chl_k
Units	[m^{-3}]	[m^{-1}]	[m^{-1}]	[m^{-1}]	[unitless]	[mg m^{-3}]	[mg m^{-3}]
Bulk	**3.54E+14**	**7.13E-03**	**3.14E-01**	**7.33E-04**	**2.64**	**195.825**	**0.298**
MIN1	-	-	-	-	-	-	-
COL2	3.50E+14	1.28E-04	9.00E-04	2.94E-04	-	11.100	-
HBAC	5.00E+11	8.60E-05	2.12E-02	1.26E-04	-	13.556	-
COL3	3.00E+12	6.50E-05	2.20E-03	1.16E-04	-	5.499	-
MIN2	-	-	-	-	-	-	-
PROC	-	-	-	-	6.65	-	-
SYNE	7.00E+09	3.48E-04	2.23E-03	6.26E-06	5.61	0.995	0.015
SYMA	-	-	-	-	6.65	-	-
PEUK	4.00E+09	8.04E-04	3.86E-03	4.79E-06	5.34	1.631	0.037
DET1	1.00E+11	1.82E-03	2.58E-01	1.78E-04	-	152.060	-
MIN3	-	-	-	-	-	-	-
NAN1	1.70E+09	2.49E-03	2.07E-02	6.54E-06	4.61	5.477	0.123
NAN2	2.00E+07	1.02E-03	3.75E-03	1.26E-06	5.18	2.870	0.064
MIC1	5.00E+05	3.75E-04	5.89E-04	5.24E-07	5.41	2.636	0.059

Table 2.15. Results for the example mineral-enriched model (model IV, inclusion of small minerals). The IOPs and POC and Chl concentrations, are indicated for each particle class k within the model as well as the bulk results for the model as a whole.

	N_k	$a_{p,k}(676)$	$b_{p,k}(555)$	$b_{bp,k}(555)$	$\frac{a_k(555)}{a_k(490)} * \frac{b_{b,k}(490)}{b_{b,k}(555)}$	POC_k	Chl_k
Units	[m^{-3}]	[m^{-1}]	[m^{-1}]	[m^{-1}]	[unitless]	[mg m^{-3}]	[mg m^{-3}]
Bulk	**3.57E+14**	**5.65E-03**	**1.98E-01**	**3.27E-03**	**2.48**	**58.972**	**0.298**
MIN1	-	-	-	-	-	-	-
COL2	3.50E+14	1.28E-04	9.00E-04	2.94E-04	-	11.100	-
HBAC	5.00E+11	8.60E-05	2.12E-02	1.26E-04	-	13.556	-
COL3	3.00E+12	6.50E-05	2.20E-03	1.16E-04	-	5.499	-
MIN2	3.00E+12	1.52E-04	1.17E-01	2.70E-03	-	-	-
PROC	-	-	-	-	6.65	-	-
SYNE	7.00E+09	3.48E-04	2.23E-03	6.26E-06	5.61	0.995	0.015
SYMA	-	-	-	-	6.65	-	-
PEUK	4.00E+09	8.04E-04	3.86E-03	4.79E-06	5.34	1.631	0.037
DET1	1.00E+10	1.82E-04	2.58E-02	1.78E-05	-	15.206	-
MIN3	-	-	-	-	-	-	-
NAN1	1.70E+09	2.49E-03	2.07E-02	6.54E-06	4.61	5.477	0.123
NAN2	2.00E+07	1.02E-03	3.75E-03	1.26E-06	5.18	2.870	0.064
MIC1	5.00E+05	3.75E-04	5.89E-04	5.24E-07	5.41	2.636	0.059

Table 2.16. Bulk IOPs, POC, and Chl results for all models.

ID	$a_p(676)$ [m^{-1}]	Chl [mg m^{-3}]	$b_{bp}(555)$ [m^{-1}]	POC [mg m^{-3}]	POC / Chl	$a_d(440)$ / $a_p(440)$	$a(555)*b_b(490)$ / $a(490)\ b_b(555)$
Base Model							
	5.50E-03	2.98E-01	5.73E-04	5.90E+01	1.98E+02	2.87E-01	3.21E+00
Alternate Base Models (3)							
I	5.50E-02	2.98E+00	5.73E-03	5.90E+02	1.98E+02	2.87E-01	1.05E+00
II	1.81E-03	9.85E-02	1.89E-04	1.95E+01	1.98E+02	2.87E-01	4.45E+00
III	5.35E-03	2.75E-01	5.70E-04	5.29E+01	1.92E+02	2.71E-01	3.25E+00
Single-Class Phytoplankton Models (10)							
I	6.89E-03	3.59E-01	5.98E-04	6.30E+01	1.76E+02	2.26E-01	2.95E+00
II	8.71E-03	4.45E-01	5.92E-04	6.55E+01	1.47E+02	1.87E-01	2.81E+00
III	1.55E-02	7.90E-01	5.99E-04	8.09E+01	1.02E+02	1.16E-01	2.30E+00
IV	9.56E-03	5.56E-01	5.78E-04	7.05E+01	1.27E+02	1.97E-01	2.77E+00
V	7.00E-03	5.35E-01	5.75E-04	6.95E+01	1.30E+02	2.56E-01	3.01E+00
I*	8.63E-03	4.34E-01	6.29E-04	6.79E+01	1.57E+02	1.79E-01	2.69E+00
II*	1.27E-02	6.28E-01	6.16E-04	7.37E+01	1.17E+02	1.30E-01	2.45E+00
III*	2.79E-02	1.41E+00	6.32E-04	1.08E+02	7.70E+01	6.63E-02	1.79E+00
IV*	1.46E-02	8.78E-01	5.84E-04	8.48E+01	9.65E+01	1.41E-01	2.41E+00
V*	8.87E-03	8.31E-01	5.78E-04	8.27E+01	9.95E+01	2.26E-01	2.82E+00
High Chlorophyll-a Models (3)							
I	2.97E-02	1.77E+00	6.38E-04	1.25E+02	7.05E+01	6.78E-02	1.77E+00
II	3.00E-02	1.77E+00	7.82E-04	1.54E+02	8.68E+01	1.05E-01	1.71E+00
III	3.05E-02	1.77E+00	8.36E-04	1.99E+02	1.13E+02	1.56E-01	1.66E+00
HBAC Models (2)							
I	5.84E-03	2.98E-01	1.08E-03	1.13E+02	3.79E+02	4.66E-01	2.81E+00
II	6.27E-03	2.98E-01	1.71E-03	1.81E+02	6.07E+02	5.94E-01	2.48E+00
Colloid Models (4)							
I	6.01E-03	2.98E-01	1.75E-03	1.03E+02	3.46E+02	4.50E-01	2.83E+00
II	6.65E-03	2.98E-01	3.22E-03	1.59E+02	5.32E+02	5.73E-01	2.56E+00
III	5.76E-03	2.98E-01	1.04E-03	8.10E+01	2.71E+02	3.81E-01	2.78E+00
IV	6.08E-03	2.98E-01	1.61E-03	1.08E+02	3.64E+02	4.68E-01	2.45E+00
Detritus Models (8)							
I	6.23E-03	2.98E-01	6.44E-04	1.20E+02	4.02E+02	4.75E-01	2.92E+00
II	7.13E-03	2.98E-01	7.33E-04	1.96E+02	6.56E+02	6.06E-01	2.64E+00
III	5.44E-03	2.98E-01	5.70E-04	5.40E+01	1.81E+02	2.70E-01	3.23E+00
IV	5.94E-03	2.98E-01	6.32E-04	9.48E+01	3.18E+02	4.26E-01	3.01E+00
V	6.56E-03	2.98E-01	7.08E-04	1.46E+02	4.89E+02	5.47E-01	2.77E+00
VI	6.76E-03	2.98E-01	6.19E-04	1.69E+02	5.65E+02	5.22E-01	2.84E+00
VII	5.73E-03	2.98E-01	5.80E-04	7.96E+01	2.67E+02	3.42E-01	3.14E+00
VIII	5.86E-03	2.98E-01	5.92E-04	8.94E+01	3.00E+02	3.88E-01	3.08E+00
Mineral Models (7)							
I	5.51E-03	2.98E-01	8.43E-04	5.90E+01	1.98E+02	2.84E-01	3.04E+00
II	5.57E-03	2.98E-01	1.92E-03	5.90E+01	1.98E+02	2.74E-01	2.68E+00
III	5.65E-03	2.98E-01	3.27E-03	5.90E+01	1.98E+02	2.63E-01	2.48E+00
IV	5.52E-03	2.98E-01	6.73E-04	5.90E+01	1.98E+02	2.84E-01	3.14E+00
V	5.60E-03	2.98E-01	1.08E-03	5.90E+01	1.98E+02	2.72E-01	2.95E+00
VI	5.71E-03	2.98E-01	1.58E-03	5.90E+01	1.98E+02	2.59E-01	2.78E+00
VII	5.65E-03	2.98E-01	1.55E-03	5.90E+01	1.98E+02	2.65E-01	2.81E+00

2.8. References

Bishop, J. K. B. (1999). Transmissometer measurement of POC, *Deep-Sea Res. Part I*, *46*, 353–369.

Bohren, C. F. and D. R. Huffman (1983), *Absorption and scattering of light by small particles,* J. Wiley and Sons, New York.

DuRand, M., R. Green, H. Sosik, and R. J. Olson (2002). Diel variations in optical properties of Micromonas pusilla (Prasinophyceae). *J. Phycol.. 38*, 1132-1142.

Gardner, W. D., I. D. Walsh, and M. J. Richardson (1993), Biophysical forcing of particle production and distribution during a spring bloom in the North Atlantic, *Deep Sea-Res. Part II*, *40*, 171–195.

Gordon, H. R. and A. Morel (1983), *Remote assessment of ocean color for interpretation of satellite visible imagery - A review. Lecture notes on coastal and estuarine studies*, 114 pp., Springer-Verlag, New York.

Loisel, H. and A. Morel, A. (1998), Light scattering and chlorophyll concentration in case 1 waters: A reexamination. *Limnol. Oceanogr.*, *43*, 847-858.

Montagnes, D. J., J. A. Berges, P. J. Harrison, and F. J. R. Taylor (1994), Estimation of carbon, nitrogen, protein, and chlorophyll a from volume in marine phytoplankton. *Limnol. Oceanogr.*, *39*, 1044–1060.

Morel, A. (1974), Optical properties of pure water and pure sea water, in *Optical Aspects of Oceanography*, edited by N. G. Jerlov and E. Steeman-Nielsen, pp. 1-24, Academic Press, New York.

Morel, A. and L. Prieur, L. (1977), Analysis of variations in ocean color. *Limnol. Oceanogr.*, *22*, 709-722.

O'Reilly, J. E, S. Maritorena, B. G. Mitchell, D. A. Siegel, K. L. Carder, S. A. Garver, M. Kahru, and C. R. McClain (1998), Ocean color chlorophyll algorithms for SeaWiFS, *J. Geophys. Res., 103*, 24937–24953.

Pope, R. and E. Fry (1997), Absorption spectrum (380-700 nm) of pure water .2. Integrating cavity measurements. *Appl.Opt.*, 36, 8710-8723.

Reynolds, R. A., D. Stramski, and B. G. Mitchell (2001), A chlorophyll-dependent semianalytical reflectance model derived from field measurements of absorption and backscattering coefficients within the Southern Ocean, *J. Geophys. Res*., 106 (C4), 7125–7138.

Stramska, M., and D. Stramski (2005), Variability of particulate carbon concentration in the north polar Atlantic based on ocean color observations with Sea-viewing Wide Field-of-view Sensor (SeaWiFS), *J. Geophys. Res*., *110*, C10018, doi:10.1029/2004JC002762.

Stramski, D., A. Bricaud, and A. Morel (2001), Modeling the inherent optical properties of the ocean based on the detailed composition of planktonic community, *Appl. Opt.*, *40*, 2929-2945.

Stramski, D., and A. Morel (1990), Optical properties of photosynthetic picoplankton in different physiological states as affected by growth irradiance, *Deep-Sea Res. 37*, 245-266.

Stramski, D., E. Boss, D. Bogucki, and K. J. Voss (2004), The role of seawater constituents in light backscattering in the ocean, *Prog. Oceanogr.*, 61, 27-56.

Stramski, D., R. A. Reynolds, M. Kahru, and B. G. Mitchell (1999), Estimation of particulate organic carbon in the ocean from satellite remote sensing, *Science, 285*, 239-242.

Stramski, D., and R. A. Reynolds (1993), Diel variations in the optical properties of a marine diatom. *Limnol. Oceanogr.*, *38*, 1347-1364.

Stramski, D., R. A. Reynolds, M. Babin, S. Kaczmarek, M. R. Lewis, R. Röttgers, A. Sciandra, M. Stramska, M. S. Twardowski, B. A. Franz, and H. Claustre (2008), Relationships between the surface concentration of particulate organic carbon and optical properties in the eastern South Pacific and eastern Atlantic Oceans, *Biogeosciences*, *5*, 171-201.

Verity, P. G., C. Y. Robertson, C. R. Tronzo, M. G. Andrews, J. R. Nelson, and M. E. Sieracki (1992). Relationships between cell volume and the carbon and nitrogen content of marine photosynthetic nanoplankton, *Limnol. Oceanogr.*, 37,1434–1446.

Chapter 3. Seasonal and Interannual Variability of Particulate Organic Carbon within the Southern Ocean from Satellite Ocean Color Observations

3.0. Abstract

We use field data of particulate organic carbon (POC) concentration and spectral remote-sensing reflectance, $R_{rs}(\lambda)$, to develop an empirical algorithm for estimating POC from ocean color in the Southern Ocean. The algorithm based on the band ratio $R_{rs}(443)/R_{rs}(555)$ is used in conjunction with SeaWiFS satellite data to demonstrate seasonal and interannual variability in POC from 1997 through 2007. The surface POC concentrations generally range from 30 to 120 mg m^{-3}. On a whole basin scale (south of 35°S), the monthly means are mostly 70 - 80 mg m^{-3}. The seasonal signal is weakest at lower latitudes within the Sub-Antarctic Zone and most pronounced at higher latitudes (>55°S). The area-integrated stock of water column POC in the upper 100 m shows small interannual variations and no clear evidence for long-term trend during the examined 10-year period. The seasonal maximum of the POC stock occurs in December and reaches a value of about 0.6 Pg of carbon for the entire basin south of 35°S. The seasonal range of area-normalized POC is between about 5.5 and 6.6 g m^{-2}. The region south of 55°S provides a dominant contribution to the accumulation of POC within the Southern Ocean during the productive period of the season. During the austral spring, the area-normalized POC accumulates in these high-latitude waters at rates from about 0.2 to 0.7 g m^{-2} $month^{-1}$. The comparison of

these rates with large-scale satellite-based estimates of net primary production indicates that only a small fraction (<10%) of production accumulates as POC.

3.1. Introduction

The Southern Ocean is a unique oceanic domain that encircles the globe providing a link for exchanges of water masses and climatically significant quantities between the world's major ocean basins and atmosphere. Numerous recent studies have been motivated by a need to advance an understanding of the role of the Southern Ocean in regulating atmospheric CO_2 over time scales relevant to climate change and how the ecosystem structure and biogeochemical cycles of the Southern Ocean respond to climate change [e.g., *Sarmiento and Orr*, 1991; *Sarmiento et al*., 2004; *Le Quéré et al*., 2007]. The Southern Ocean, in particular a region of the Antarctic Circumpolar Current between 40^{o} and 60^{o}S, has been identified as a contemporary net sink for atmospheric CO_2 on an annual basis, but the magnitude of this sink is not firmly established [e.g., *Metzl et al.*, 1999; *Takahashi et al*., 2002; *McNeil et al*., 2007].

The drawdown of atmospheric CO_2 into the ocean is favored by: (i) the increase in the CO_2 solubility in the cold high-latitude surface waters that sink to form the deep waters of the ocean, and (ii) biological uptake of CO_2 *via* phytoplankton photosynthesis in the euphotic zone of the ocean, which results in the production of particulate and dissolved forms of organic carbon that is then partly exported into the deep sea. The ice-free Southern Ocean is the largest of several oceanic regions with high-nutrient low-chlorophyll (HNLC) characteristics, where major macronutrients

(nitrate, phosphate, silicate) occurring in significant concentrations in surface waters are under utilized by autotrophic processes [*Martin et al*., 1991; *Mitchell et al*., 1991; *Banse*, 1996]. These characteristics indicate that the capacity of the biological pump to export organic carbon out of the euphotic layer within the majority of the Southern Ocean is less than its potential maximum. Recent experimental and modeling studies showed, however, relatively high estimates of efficiency of the biological pump exporting particulate organic carbon (POC) [*Honjo et al.*, 2000; *Trull et al*., 2001; *Schlitzer*, 2002]. Potential changes in the efficiency of the Southern Ocean's biological pump are of interest because they may affect air-sea CO_2 fluxes and levels of atmospheric CO_2 [e.g., *Knox and McElroy*, 1984; *Sarmiento and Toggweiler*, 1984; *Siegenthaler and Wenk*, 1984].

An assessment of biological controls of the carbon cycle, including the efficiency of the biological pump and air-sea CO_2 fluxes, requires determinations of various carbon reservoirs as well as the processes responsible for transformations and transport of carbon, such as primary production, remineralization, and export of organic carbon. POC in the surface ocean, which consists of autotrophic and heterotrophic plankton and biologically-derived detrital particles, is one of the reservoirs of substantial importance. The biological pump that exports organic carbon out of the surface ocean is effected largely by sinking particles, which provides a mechanism for a long-term storage of atmospheric CO_2 in the deep ocean [*Volk and Hoffert*, 1985; *Longhurst and Harrison*, 1989]. In addition, the net change of POC in the surface ocean is a component of net community production (NCP), which is defined as gross primary production minus respiration by all the autotrophic and

heterotrophic organisms [e.g., *Eppley*, 1989]. As the NCP describes the net amount of organic carbon produced, it is equivalent to the net amount of inorganic carbon biologically consumed in surface waters. Therefore, the NCP integrated within the euphotic layer over a certain period of time determines the role of biological activities for the inorganic carbon budget in surface waters and can also provide a useful constraint for estimating export production out of the euphotic layer if sufficient information about carbon mass balance components, including the net change of POC, is available [*Bates et al*., 1998; *Hansell and Carlson*, 1998; *Sweeney et al*., 2000; *Sabine et al*., 2004].

The stock of POC in the upper ocean is highly variable and its large-scale distributions and long-term variations are poorly characterized. Historically, the large-scale estimates of this variability have been difficult to derive with confidence, primarily because conventional oceanographic sampling has been both temporally and spatially sparse. Recent efforts to develop remote sensing algorithms for estimating POC in the upper ocean from satellite imagery of ocean color offer significant potential for extending temporal and spatial scales of observations in marine biogeochemical studies [*Stramski et al.*, 1999; *Loisel et al*., 2001; *Mishonov et al*., 2003; *Stramska and Stramski*, 2005; *Gardner et al*., 2006; *Pabi and Arrigo*, 2006; *Stramski et al*., 2008; *Son et al*., 2009]. The commonly accepted empirical approach to develop algorithms for estimating seawater constituent concentrations from the spectral ocean reflectance (ocean color) requires the simultaneous collection of *in situ* data of relevant optical quantities and seawater constituents. Whereas relatively large amounts of such field data have been collected over the years to allow the

development of chlorophyll algorithms [e.g., *O'Reilly et al.,* 1998; 2000], the amount of data relevant for the POC algorithm development is much more limited. Only a few studies exist in which the development of POC algorithms is based on an adequate suite of simultaneously collected *in situ* data that include POC, ocean reflectance, and inherent optical properties (IOPs) of seawater [*Stramski et al.*, 1999; *Stramska and Stramski*, 2005; *Pabi and Arrigo*, 2006; *Stramski et al*., 2008]. Clearly, due to the limited availability of adequate field data and their limited geographic coverage, further work in this direction is required.

In this study we use field data collected on several cruises in the Southern Ocean to develop an empirical algorithm that relates surface concentration of POC to the blue-to-green band ratio of remote-sensing reflectance, R_{rs}. Our primary objective is to apply the algorithm to satellite data of Sea-viewing Wide Field-of-View Sensor (SeaWiFS) and examine seasonal and interannual variability in POC within the surface waters of the Southern Ocean during a period from September 1997 through December 2007.

3.2. Field Experiments

Optical and POC measurements were made during several oceanographic cruises within three regions of the Southern Ocean spanning a time period from 1997 through 2006. These regions include the waters near Antarctic Peninsula and South Shetland Islands (LMG04, AMLR04, and AMLR06 cruises), the Antarctic Polar Frontal Zone (PFZ) within the Pacific sector (REV98 cruises), and the Ross Sea (NBP97 cruise) (Figure 3.1). The stations were located in high-latitude waters south

of 50°S. Most stations were south of 60°S. During each cruise vertical profiles of optical data were collected from several instruments either mounted on the ship's CTD/rosette system for simultaneous *in situ* measurements with discrete water sampling or deployed shortly before or after the CTD/rosette cast. These deployments of the CTD/rosette and optical instruments constitute a common station. Data collected at the common station are considered "coincident in time and space" for the purposes of development of the POC algorithm. The measurements of direct interest to this study include *in situ* vertical profiles of radiometric quantities from which the remote-sensing reflectance was determined and the analysis of water samples for the determinations of POC concentration. We restrict our algorithm development to the use of POC and optical data from open water stations where it is reasonable to assume that optical properties and suspended particles are dominated by plankton microorganisms and plankton-derived organic matter.

3.2.1. *In situ* Radiometric Measurements

Underwater vertical profiles of spectral downwelling irradiance, $E_d(z, \lambda)$, and upwelling radiance in the nadir direction, $L_u(z, \lambda)$ (where z is depth and λ light wavelength in vacuo), were made with several calibrated radiometers (Biospherical Instruments, Inc.), each having a number of wavebands in the visible and ultraviolet spectral regions. Specifically, we used MER-2040 and MER-2048 profiling radiometers that were mounted on an optical package lowered by the ship's winch, or PRR-600 and PRR-800 radiometers deployed as free-falling instruments.

The radiometric measurements and data processing were consistent with methods described in NASA protocols [*Mueller et al*., 2003]. Profiles were visually inspected for quality, the data were binned into 1-m depth intervals, and the near-surface data (usually the top 3-5 m) were rejected from the analysis to avoid surface wave effects. A depth range within the upper mixed layer (typically 5-20 m) was then selected for extrapolation of $E_d(z, \lambda)$ and $L_u(z, \lambda)$ to immediately beneath the sea surface using the vertical attenuation coefficients for downwelling irradiance (K_d) and upwelling radiance (K_{Lu}). The estimates of $E_d(z = 0^-, \lambda)$ and $L_u(z = 0^-, \lambda)$ just beneath the surface were propagated through the surface to yield the above-water estimates of downward irradiance, $E_d(z = 0^+, \lambda) \equiv E_s(\lambda)$, and water-leaving radiance, $L_u(z = 0^+, \lambda) \equiv L_w(\lambda)$. The effective coefficients for propagating E_d and L_u through the water-air interface were: $E_d(z = 0^+, \lambda)/E_d(z = 0^-, \lambda) = 1/0.957$ and $L_u(z = 0^+, \lambda)/L_u(z = 0^-, \lambda) = 0.5425$. The value of 0.5425 for the transmittance coefficient for L_u corresponds to the refractive index of water, $n_w = 1.343$, which is a reasonable value representative of the visible spectral range [e.g., *Mobley,* 1994].

In the final step of computations, the spectral remote sensing-reflectance just above the water surface was obtained as $R_{rs}(\lambda) = L_w(\lambda)/E_s(\lambda)$. With the values for the effective transmittance coefficients for radiance and irradiance assumed in this study, the relationship between $R_{rs}(\lambda)$ and its counterpart reflectance just below the surface is: $R_{rs}(\lambda) = 0.519\ L_u(z = 0^-, \lambda)/E_d(z = 0^-, \lambda)$. For the purposes of POC algorithm development, our interest in this study is focused on the $R_{rs}(\lambda)$ values from the blue and green spectral regions.

3.2.2. POC Determinations

Discrete water samples were collected from Niskin bottles triggered at several depths within the upper water column extending typically to 200 m during CTD/rosette profiles. For the determinations of POC concentration, suspended particles were collected by filtration under low vacuum of measured volumes of water samples onto precombusted (450°C for 4 hours) 25-mm Whatman glass-fiber filters (GF/F). After filtration, the samples were rinsed with 0.01N HCl to remove inorganic carbon, transferred to sterile glass vials, dried at 55°C in a clean oven, and stored until post cruise analysis in the laboratory. POC was determined by high temperature combustion of sample filters *via* standard CHN analysis [*Parsons et al*., 1984; *Knap et al*., 1996]. Blank filters were also collected during the cruises to quantify background POC. Precombusted blank GF/F filters were placed on the filtration rig with a small amount of deionized water for the same period of time needed to filter samples of seawater. The blank filters were then processed the same way as sample filters.

The final values of POC concentration were calculated by subtracting the mass of organic carbon on blank filters from the mass of carbon on sample filters, and then dividing this result by the measured volume of filtered sample. For the AMLR04, LMG04, and AMLR06 cruises, replicate POC samples were taken for each depth examined and averaged to produce the final POC concentration; otherwise the POC estimate was obtained from the analysis of a single sample filter. For the development of the POC algorithm we only consider data collected at near-surface depths (< 10 m). The POC data between the surface and the depths exceeding 100 m are considered in

the development of the relationship between the surface POC and the water-column integrated (0-100 m) POC stock.

3.3. Results and Discussion

3.3.1. Reflectance Band-ratio Algorithm for POC

Our approach for developing algorithms to estimate surface POC concentration from ocean reflectance relies on empirical relationships between surface POC and the blue-to-green (BG) band-ratio of remote-sensing reflectance, $R_{rs}(\lambda_B)/R_{rs}(555)$. The rationale for the POC band-ratio algorithm is similar to that used to estimate chlorophyll-*a* concentration from reflectance band-ratio algorithms. Specifically, in the case of POC algorithm, variations in the BG ratio can be viewed as being driven largely by changes in the spectral absorption coefficient of seawater associated with varying concentrations of all kinds of POC-containing particles, which include not only pigmented phytoplankton but also organic detritus and heterotrophic organisms. All these POC-containing particle types show higher absorption in the blue than in the green spectral region, so their effect on the BG ratio is expected to be qualitatively similar.

We examined the relationship between the surface POC and the following band ratios of reflectance: $R_{rs}(443)/R_{rs}(555)$, $R_{rs}(490)/R_{rs}(555)$, $R_{rs}(510)/R_{rs}(555)$, and the maximum band ratio, *MBR*. *MBR* represents the largest of the three ratios considered. $R_{rs}(443)/R_{rs}(555)$ was most frequently the largest (55%) and $R_{rs}(510)/R_{rs}(555)$ was least frequently the largest (15%) amongst the three ratios considered within our data set. Note that the bands centered at 443, 490, 510, and 555

nm are consistent with the SeaWiFS wavebands [*McClain et al*., 2004], and these bands are currently used in the NASA algorithm for estimating chlorophyll-*a* concentrations in the global ocean [*O'Reilly et al.*, 1998; 2000]. We tested two equations for fitting the data of POC versus reflectance ratio. One equation is the power function and the other equation has the form of the current Ocean Chlorophyll 4 (OC4) algorithm [*O'Reilly et al*., 2000].

The simple power function of POC versus $R_{rs}(443)/R_{rs}(555)$ was found to have slightly better error statistics than the other algorithms tested. This power function is POC = 189.29 $[R_{rs}(443)/R_{rs}(555)]^{-0.870}$, which is shown in Figure 3.2 along with the data points. Presently this algorithm appears to be the best choice for the applications in the Southern Ocean. For our data set consisting of 85 measurements that were used to derive this algorithm, the mean normalized bias is 3.2%, the normalized root mean square error is 27.3%, and the determination coefficient is 0.933 [see *Stramski et al*., 2008 for formulas for calculating the error statistics].

The best fit coefficients for the Southern Ocean algorithms show some differences when compared with the previous analysis of POC and reflectance measurements taken in other oceanic regions [*Stramska and Stramski*, 2005; *Stramski et al*., 2008]. For example, the coefficients of the power function POC = A $[R_{rs}(443)/R_{rs}(555)]^{B}$ for the data from the tropical and subtropical waters of the eastern South Pacific and eastern Atlantic Oceans examined in *Stramski et al.* [2008] were A = 203.2 and B = -1.034. These differences support the notion that some variability in the empirical band-ratio algorithms can be expected within the open waters of the global ocean. Naturally, the optically complex coastal environments present even greater

research challenges for ocean color algorithms. In this study, we restricted the algorithm development to the use of data from open water stations and we excluded data from near-coastal stations visited on the AMLR cruises due to potentially significant input of terrigenous material. Some data included in our analysis were collected during an intense bloom of *Phaeocystis antarctica* in the Ross Sea where POC was significantly higher than typical open water concentrations (see the NBP97 data points for POC > 800 mg m^{-3} in Figure 3.2).

It is of interest to note that the use of the blue-to-green reflectance band ratios as inputs to POC and chlorophyll-*a* algorithms implies that both estimated variables are forced to always covary. However, because the band-ratio algorithms for POC and chlorophyll-*a* are described by different nonlinear functions, the ratio of the two data products will not be constant over the dynamic range of these variables. Nevertheless, further work on approaches that have potential for more effective decoupling of the remote sensing estimations of POC and chlorophyll-*a* appears to be warranted [*Stramski et al*., 2008].

3.3.2. Satellite Estimates of POC in the Southern Ocean

To evaluate the spatial, seasonal, and interannual variations of surface POC in the Southern Ocean, we applied our power function algorithm based on the band ratio $R_{rs}(443)/R_{rs}(555)$ to the SeaWiFS-derived $R_{rs}(\lambda)$. For this analysis the Level 3B standard SeaWiFS data products of normalized-water leaving radiance, $nL_w(\lambda)$, binned to a 9x9 km equal-area grid within monthly intervals spanning a period of over 10 years from September 1997 through December 2007 were obtained from the NASA

Ocean Color Web. These data result from SeaWiFS Reprocessing 5.2. Because our POC algorithm requires $R_{rs}(\lambda)$ as input, the satellite estimates of $nL_w(\lambda)$ were first converted to $R_{rs}(\lambda)$ using the relationship $R_{rs}(\lambda) = nL_w(\lambda) / F_o(\lambda)$, where $F_o(\lambda)$ is the extraterrestrial solar constant. The values of $F_o(\lambda)$ were taken from *Thuillier et al*. [2003]. After determining the satellite estimates of $R_{rs}(\lambda)$, the POC algorithm was applied to produce the monthly composites of POC distribution within the Southern Ocean.

3.3.2.1. Surface Concentration of POC

Maps of monthly mean POC concentrations obtained by averaging data for each month over a 10-year period are displayed in Figure 3.3. The valid pixels of ocean color data are determined through standard NASA processing after screening for clouds, sun glint, ice cover, atmospheric correction failure, and other failure conditions (e.g., negative R_{rs}). The white areas in the maps reflect data that are flagged as invalid with this standard processing. Because of multiyear averaging of monthly composites, significant seasonal change in the white area seen in Figure 3.3 can be attributed primarily to winter darkness, short day length, low solar elevation, and seasonal variation in sea ice extent at high latitudes. Other factors, such as cloud cover, appear to have smaller contribution to the extent of data gaps in these multiyear average maps. During the austral autumn, winter, and early spring, large amounts of invalid (flagged) satellite data limit our investigation of POC to lower latitudes, generally north of 50^{o}-55^{o}S. The POC maps for July and August have no valid data south of 55^{o}S. The spatial pattern and seasonal change of white areas in Figure 3.3 for

August through April resemble monthly images of sea ice coverage obtained from passive microwave remote sensing [*Comiso et al*., 1993; *Parkinson*, 2004]. For May-July the white areas are also largely related to NASA-flagged invalid ocean color data due to large solar zenith angle.

One of the most striking features of the POC distributions displayed in Figure 3 occurs at latitudes of about 35-40^{o}S within the Subtropical Frontal Zone, STFZ. This zone separates the nitrate replete subantarctic waters of the Southern Ocean from the lower latitude nitrate-deplete subtropical gyres where primary production is very low [*Belkin and Gordon*, 1996]. A significant north-to-south increase in POC is observed throughout the year within STFZ all around the globe.

The monthly distributions of POC show significant spatial variability within the Southern Ocean. Elevated POC concentrations generally occur within and downstream of coastal and shelf areas, in regions of major fronts, and areas associated with sea ice retreat. These areas of elevated POC are generally consistent with previous satellite-based estimates of enhanced chlorophyll-*a* concentrations and primary production in the Southern Ocean [*Comiso et al.*, 1993; *Sullivan et al*., 1993; *Arrigo et al.*, 1998; *Moore and Abbott*, 2000; *Arrigo et al*., 2008]. For example, among the coastal and shelf regions, high POC values often exceeding 150 mg m^{-3}, are seen off the east coast of South America, in waters surrounding and downstream of Kerguelen Islands (~50^{o}S, 70^{o}E), off southern Australia and New Zealand, and in some shelf and coastal areas around the Antarctic continent. High POC values are observed in parts of the Ross Sea from December through the rest of austral summer,

which can be attributed to the development of phytoplankton blooms in areas of sea ice retreat [*Arrigo and McClain*, 1994; *Arrigo and van Dijken*, 2003].

Bands of elevated POC associated with fronts are also apparent in the Atlantic and Indian sectors of the Southern Ocean. These bands occur within two major frontal zones, the Subtropical Frontal Zone, STFZ, and the Polar Frontal Zone, PFZ. Moving from low to high latitudes, the STFZ is bounded by the North Subtropical Front, NSTF, and the South Subtropical Front, SSTF, and the PFZ is bounded by Subantarctic Front, SAF, and the Polar Front, PF [*Belkin and Gordon*, 1996]. These frontal structures encompass the flow of the Antarctic Circumpolar Current, ACC. The major oceanic regime north of PFZ is generally regarded as the Sub-Antarctic Zone (SAZ). The regime from the PF southward to the continental margins of Antarctica is the Antarctic Zone (AZ) [*Orsi et al.*, 1995, *McNeil et al*., 2007]. The AZ encompasses Antarctic surface water masses which are widely subject to winter ice and the effects of melting within the marginal ice zone.

By showing the multiyear monthly means of POC based on averaging data from a 10-year period, Figure 3.3 highlights the persistent POC features that occur consistently every year or nearly every year in the same areas of the Southern Ocean. The spatial distribution of POC in any given month can, however, vary considerably from year to year. Example illustration of this variability is provided in Figure 3.4, which compares a 10-year mean distribution of POC for the month of January with the distributions for January 1999, 2001, and 2006. One can see, for example, that the region of very low POC in the southeastern Pacific sector and extending through the southern part of the Drake Passage is significantly more pronounced in January 1999

compared with other images. Another example is the presence of relatively large area of elevated POC within the southeastern Atlantic sector in January 2006. This feature has a much less pronounced expression in other images.

The statistical characteristics of seasonal variability in surface POC are presented in Figures 3.5 and 3.6. These calculations were made for the entire Southern Ocean, which for the purpose of this study is defined as the area south of 35^{o}S. The latitude of 35^{o}S is close to the mean position of the North Subtropical Front that is often used to mark the northern border of the Southern Ocean [e.g., *Belkin and Gordon*, 1996; *Moore and Abbott*, 2000; *MacCready and Quay*, 2001]. During the months from November through February, which encompass the peak of the growing season for phytoplankton at high latitudes, the probability density functions of POC are generally broader and show higher frequency of occurrence of relatively high POC > 100 - 150 mg m^{-3} compared with the rest of the year (Figure 3.5).

The mean and mode values of POC obtained from these probability distributions show moderate seasonal variation (Figure 3.6a). The maximum value of monthly mean POC slightly above 80 mg m^{-3} is observed in December. Similarly high values occur in November and January. The minimum monthly mean POC during the austral winter is below 70 mg m^{-3}, but it is important to recall that the estimation of winter values exclude large areas south of 50^{o} - 55^{o}S due to the lack of valid SeaWiFS data. The standard deviation varies from about 40 to 50 mg m^{-3} for the different months. For each month the standard deviation about the mean represents the combined effect associated with both the spatial variation of POC within the Southern Ocean and the year-to-year variation. As the probability distributions

generally display asymmetry (see Figure 3.5), the mode is smaller than the mean POC (Figure 6a). For the months of February, March, and April the difference between these statistical parameters is largest, about 15 mg m^{-3}.

To illustrate the geographic distribution of POC seasonality, we also calculated zonally averaged POC concentration (Figure 3.6b). The Southern Ocean shows a significant degree of north-south differentiation by zone in physical, chemical, and biological characteristics [e.g., *Deacon*, 1982; *Pollard et al*., 2002]. We defined three latitudinal zones, 35° - 45°S, 45° - 55°S, and south of 55°S. As the zones were determined simply by latitude, they can only be roughly related to major oceanic regimes or ecological provinces that are typically defined on the basis of fronts, bathymetry, sea ice coverage, and other physical or biogeochemical features. The 35° - 45°S zone overlaps largely with the Subtropical Frontal Zone, STFZ, and encompasses significant parts of the major oceanic regime of the Sub-Antarctic Zone (SAZ). This region is also within the ecological province that was referred to as the Subantarctic Water Ring (SWR) in the satellite-based study of chlorophyll distributions and primary production in the Southern Ocean [*Moore and Abbott*, 2000]. The latitude band between 45°S and 55°S also largely coincides with the SAZ and the SWR province, especially in the Pacific sector where the mean path of the Antarctic Polar Front (PF) is located south of 55°S [*Gille*, 1994; *Orsi et al*., 1995; *Belkin and Gordon*, 1996; *Moore et al*., 1999]. Over much of the Atlantic sector and also within the Indian Ocean sector (approximately between 50°W and 150°E), the mean path for the PF is, however, generally north of 55°S and can extend as far north as 50°S. In these areas the 45° - 55°S band includes the Polar Frontal Zone.

The large expanses around the Antarctic continent within the latitudinal zone south of 55°S also comprise more than just one major oceanic domain or ecological province. As a result of a large latitudinal range in the position of the PF of more than 10° (due to steering by continents, islands and bathymetry), the areas south of 55°S generally include both the PFZ and AZ in the Pacific sector, and the AZ in the Atlantic and Indian Ocean sectors. At these high latitudes, several distinct ecological regions can be defined on the basis of the variability in the extent of the sea ice cover, bathymetry, and proximity to land, such as the Permanently Open Ocean Zone (POOZ), the Seasonal Ice Zone (SIZ) that contains the Marginal Ice Zone (MIZ), and the coastal and continental shelf zone [*Tréguer and Jacques*, 1992; *Arrigo et al*., 1998; *Moore and Abbott*, 2000; *Arrigo et al*., 2008].

Figure 6b compares the seasonal progression of zonally averaged POC concentration. Weakest seasonality is observed in the 35° - 45°S zone where the highest monthly mean POC of about 80 mg m^{-3} occurs in October-November and the lowest POC of about 70 mg m^{-3} in February-March and then again from June through September. This seasonal variation is somewhat weaker than that calculated for the entire Southern Ocean south of 35°S. Our results for low latitudes within the Southern Ocean are consistent with earlier analysis of weak seasonality of phytoplankton pigment concentration in subantarctic waters [e.g., *Banse*, 1996]. In the 45° - 55°S band, the seasonal signal of POC is stronger, varying between the maximum of about 90 mg m^{-3} in December and a minimum of 60 mg m^{-3} in August. At higher latitudes south of 55°S, the seasonality is even more pronounced. Whereas the maximum mean POC in December is relatively high (~87 mg m^{-3}), the winter minimum drops to

values close to 50 mg m^{-3}. We emphasize, however, that no satellite ocean color data are available in the months of May, June, and July south of 55°S, which prevents the estimation of winter values.

Figure 3.6c shows the monthly mean ratio of ocean area with valid ocean color data to the total ocean area for the entire Southern Ocean and the three latitudinal regions considered. These values are calculated relative to the total ocean area within a given region including the areas permanently covered by ice. During winter, the satellite data coverage is limited not only within the region south of 55°S but also to a significant extent within the 45° - 55°S latitudinal zone. Only the northernmost zone between 35°S and 45°S exhibits consistently high monthly mean percentage (~96-98%) of valid ocean color pixels throughout the year.

3.3.2.2. The Upper Water-column Stock of POC

Our field data show that the surface POC concentration is reasonably well correlated with the mass of POC integrated within the upper water column between the sea surface and a depth of 100 m (Figure 3.7). At each station the POC determinations were usually made at 4-6 discrete depths from near surface to 150 m. These data were used to obtain the relationship in Figure 3.7. The limit of 100 m was chosen because our *in situ* measurements of spectral downwelling irradiance, $E_d(z, \lambda)$, indicated that the 1% level of surface irradiance at 490 nm is, on average, at a depth of about 70 m (standard deviation SD = 30 m, number of observations 65). The light close to the 490 nm waveband is usually most penetrating in open ocean waters. To a first approximation, we assume that the 100 m depth delimits the biologically active

layer where most organic carbon production *via* photosynthesis occurs in the open waters of Southern Ocean. The top 100 m layer was used in previous biogeochemical studies of the Southern Ocean, in which the upper water column primary production, net community production, POC stock, and POC export were examined [*Gardner et al*., 2000; *Buesseler et al*., 2001; *Sweeney et al*., 2000; *Arrigo et al*., 2008].

Using the relationship from Figure 3.7 and satellite-derived monthly maps of surface POC concentration, we calculated the area-integrated water-column standing stock of POC within the upper 100 m of the Southern Ocean. Because at any given time SeaWiFS data are not available for the entire area of the Southern Ocean, it is important to describe in detail the method that we use to calculate the area-integrated stock of POC. For these calculations the Southern Ocean south of 35^{o}S was first divided into 1^{o} circumpolar latitudinal bands. Each of these bands was further divided into sectors that have a 10^{o} longitudinal extent. For each sector of 1^{o} (in latitude) x 10^{o} (in longitude) and for each month, we calculated a representative value of monthly mean area-normalized water-column integrated POC, denoted as $\overline{POC}_{area,sector}$ [in units of g m^{-2}]. This value of $\overline{POC}_{area,sector}$ was obtained by converting the monthly mean surface concentration of POC [mg m^{-3}] to water-column integrated POC [g m^{-2}] (using the relationship from Figure 3.7) for each pixel within the sector where the SeaWiFS data are available, and then averaging the results for all these valid pixels within each sector. Next, the area-integrated value of water-column POC within the sector, $POC_{int,sector}$ [Pg = 10^{15} g], was determined as a product of $\overline{POC}_{area,sector}$ and the entire ocean area of the sector, A_{sector} [m^{2}]. We note that this method of calculations

essentially allows filling of "sporadic" gaps in SeaWiFS data within a given sector (for example, due to clouds, sea ice, sunglint, etc.), and therefore to account for the entire area of the sector, provided that there are some valid pixels within the sector. In this method we assume that the data from the valid pixels provide an average value of $\overline{POC}_{area,sector}$, which is representative for the entire sector. Hence, the size of each sector is reasonably limited in spatial extent, i.e. 1^o (in latitude) x 10^o (in longitude). In summary, our method of calculating the area-integrated POC includes the ocean area that is somewhat larger than the area of valid pixels themselves, and excludes the ocean area that is permanently (during a given month) inaccessible to ocean color observations, such as high latitude waters due to winter darkness, ice cover, and large solar zenith angle. In short, in our method a relatively small-area "box" (sector) is first chosen (1 deg x 10 deg), the average value based on valid pixels within that box is calculated, and then this average value is assigned to all invalid pixels within the box.

In the final step of calculations, the total area-integrated standing stock of POC within the top 100 m water column was estimated by summing up all values of $POC_{int,sector}$ corresponding to all sectors within a region of interest. As in the analysis above, these regions include the entire Southern Ocean south of 35^oS and the three zones, i.e., the 35^o-45^oS zone, the 45^o-55^oS zone, and the high-latitude region south of 55^oS. The final results of monthly means of area-integrated water-column POC for these four major regions are denoted as $POC_{int,>35}$, $POC_{int,35-45}$, $POC_{int,45-55}$, and $POC_{int,>55}$ [in units of Pg of carbon], respectively.

In the calculations of $POC_{int,>35}$, $POC_{int,35-45}$, $POC_{int,45-55}$, and $POC_{int,>55}$, we also tested alternative algorithms using sectors with higher resolution in longitude than 10^o, specifically 2^o and 5^o. As expected, the estimates of area-integrated POC stocks decreased somewhat with a decrease in the size of the sector because using larger sectors increased the probability of valid pixels that were then used to represent the entire sector. For example, for the entire Southern Ocean, the $POC_{int,>35}$ stocks from the calculations using the highest resolution, i.e., the 1^o (in latitude) x 2^o (in longitude) sectors, were lower on average by about 1.9% than the results from our standard calculations with the 1^o x 10^o sectors. In this study we report the results from the calculations based on the 1^o x 10^o sectors.

Because the estimates of area-integrated POC stock depend on the ocean area that is applied in the calculation of these estimates, it is important to show the portion of ocean area, referred to as "applied" ocean area, A_{appl}, which contributes to these final estimates of area-integrated POC. Figure 3.8 shows the monthly mean values of A_{appl} as a fraction of the total ocean area. These values are based on averaging data from a 10-year period from October 1997 through September 2007. The year-to-year variations for any given month were small, less than a few percent. As expected, the applied ocean area is generally higher than the ocean area actually associated with valid ocean color pixels shown in Figure 3.6c because of the "filling" of the full sector if some valid pixels are observed for that sector. For the 35^o-45^oS latitudinal zone, the applied area $A_{appl,35-45}$ always equals to the total ocean area, i.e. every sector within this zone has always valid pixels with SeaWiFS data (this is not explicitly displayed in Figure 8). In the 45^o-55^oS region, the applied area $A_{appl,45-55}$ shows a drastic decrease

in June-July compared with the rest of the year. There is a strong seasonal variation in the applied area in the region south of 55°S, $A_{appl,>55}$, from zero in May-July to over 90% in December-March. As a result, the applied area for the entire Southern Ocean, $A_{appl,>35}$, also shows a seasonal variation, with $A_{appl,>35}$ reduced to less than 50% of the total ocean area in June. We note that the total ocean area for the entire Southern Ocean south of 35°S is about 9.26×10^{13} m^2. The total ocean area for the latitude zone 35°-45°S is 3.23×10^{13} m^2, for the latitude zone 45°-55°S is 2.80×10^{13} m^2, and for the high-latitude region south of 55°S is 3.23×10^{13} m^2.

The large seasonal changes in the applied ocean area at high latitudes shown in Figure 3.8 contribute to the estimation of area-integrated POC stock. Therefore, in addition to calculating the area-integrated stock for the applied ocean area, we also estimated the potential values of the area-integrated POC stock for the entire ocean area in each region considered (Table 3.1). These latter estimates were obtained by multiplying the applied ocean area-based estimates of POC stock by the ratio of the total ocean area to the applied ocean area. These simple scaling calculations were made for all months and regions considered, with the exception of May, June, and July in the region south of 55°S, where no satellite data are available.

Figure 3.9 shows the two estimates of the area-integrated stock of POC within the top 100 m of the water column. The results are presented for the monthly mean values based on averaging the data over a 10-year period from October 1997 through September 2007. The interannual variations for any given month were small (the coefficient of variation typically less than 3%) and no evidence of a decadal trend was observed. The seasonal signal in the area-integrated POC is clearly observed,

especially during the October-April period for the entire Southern Ocean basin (south of 35°S), the 45-55°S zone, and the southernmost region (> 55°S) where this signal is most pronounced. The seasonality of $POC_{int,>35}$, $POC_{int,45-55}$, and $POC_{int,>55}$ is seen in both the estimates based on the applied ocean area and those scaled up to the total ocean area. The seasonal maximum occurs in December. In contrast, the POC stock at lower latitudes within the 35°-45°S zone shows smaller seasonal changes with a maximum earlier in the season during the September-November period. We recall that in this region, the applied ocean area equals to the total ocean area, so both estimates of $POC_{int,35-45}$ are identical.

The differences between the two estimates of area-integrated POC in Figure 3.9 are obviously largest during the winter months when the applied ocean area represents the smallest fraction of total ocean area. With the exception of the 35-45°S region, the area-integrated POC stocks based on the applied ocean area show a sharp decline during the winter in comparison to the estimates that are scaled up to the total ocean area. Whereas no attempt is made to estimate the winter stocks south of 55°S because of the total lack of data, one can reasonably expect that the true total winter stocks for the entire Southern Ocean will fall between the two estimates displayed in Figure 9. Such expectation also applies to the 45-55°S region. Obtaining winter estimates with higher level of confidence would require the knowledge of POC stocks within large ocean regions covered with ice, which is not available. However, because POC is not zero for ocean water inaccessible by ocean color satellite observations, we expect the total POC stocks to be closer to values scaled to the full ocean area.

The differences between the two estimates of area-integrated POC stocks are smallest during the austral summer maximum (Figure 3.9). In December, the total area-integrated stock of $POC_{int,>35}$ within the Southern Ocean reaches a value of about 0.6 Pg of carbon. It is noteworthy that the three parts of the Southern Ocean defined in our study, the 35°-45°S latitudinal zone, the 45°-55°S zone, and the region south of 55°S, each contribute approximately 0.2 Pg to $POC_{int,>35}$ during the summer maximum. We also estimate that the 10-year mean value of $POC_{int,>35}$, as determined over the period from October 1997 through September 2007, is between 0.46 Pg and 0.56 Pg. The lower estimate is based on the calculations for the applied ocean area and the higher estimate is based on the calculations scaled up to the total ocean area.

Because the estimates of area-integrated stock of POC within the upper ocean can be useful for biogeochemical modeling, we provide the monthly mean values of $POC_{int,>35}$, $POC_{int,45\text{-}55}$, $POC_{int,45\text{-}55}$, and $POC_{int,>55}$ in Table 3.1. These estimates are based on scaling our calculations up to the total ocean area for each region considered. One may expect that the estimates shown in Table 3.1 represent the upper bound for the actual POC stocks within the entire ocean areas (including areas with no valid satellite ocean color data). As noted earlier, we expect the true value to be closer to the estimates scaled to total ocean area. Nevertheless, the values presented in Table 3.1 should be viewed with caution, especially for winter months. Note, for example, that the winter values for the entire Southern Ocean are based on scaling up information acquired at latitudes less than 55°S to the entire ocean area that includes latitudes greater than 55°S.

Although the processes of seasonal accumulation or decline of organic carbon pools in the surface layer of the ocean are now well recognized, the rates of POC changes at large basin and global scales remain uncertain but are required as part of a comprehensive understanding of oceanic mediation of the global carbon cycle. The rate of change of area-integrated POC stock within the 100 m upper water column can be determined by time-differencing the satellite-derived data presented in Figure 3.9. For example, during the October-November-December period the net accumulation of POC within the entire Southern Ocean is 0.047-0.049 Pg month^{-1} (on the basis of calculations for the applied ocean area) or 0.018-0.026 Pg month^{-1} (on the basis of scaling to total ocean area). The seasonal accumulation of POC stops in January. The high-latitude waters south of 55^{o}S provide a dominant contribution to the net accumulation of POC within the entire Southern Ocean during the productive season. The average net accumulation of POC south of 55^{o}S during the October-November-December period is 0.035-0.046 Pg month^{-1} (on the basis of calculations for the applied ocean area) or 0.014-0.018 Pg month^{-1} (on the basis of scaling to total ocean area).

Figure 3.10 shows time-series of monthly values of area-normalized stocks of POC within the top 100 m layer for the entire Southern Ocean ($POC_{area,>35}$) and its three regions ($POC_{area,35-45}$, $POC_{area,45-55}$, and $POC_{area,>55}$) throughout the entire period examined from September 1997 to December 2007. These estimates (in units of g m^{-2}) were obtained respectively as the ratios: $POC_{int,>35}/A_{appl,>35}$, $POC_{int,35-45}/A_{appl,35-45}$, $POC_{int,45-55}/A_{appl,45-55}$, and $POC_{int,>55}/A_{appl,>55}$. In contrast to the area-integrated POC stocks, the area-normalized estimates are virtually insensitive to the size of sectors and

the magnitude of applied area used in the calculations. The estimates calculated using different sizes of the sectors agree to within 1% regardless of the month throughout the period of the study.

The seasonal range of $POC_{area,>35}$ is between about 5.5 and 6.6 g m^{-2}. This seasonal variation occurs around the multiyear average value of 6 g m^{-2}. Similar values of the area-normalized POC stock are observed in the three regions although seasonal variability is clearly the largest at latitudes south of 55°S. Within this high-latitude region, the seasonal minimum of $POC_{area,>55}$ is about 5 g m^{-2} and the maximum can reach 7 g m^{-2}.

Some interannual variations in the area-normalized stocks of POC are also observed. For example, the summer maximum of $POC_{area,>35}$ exceeds slightly the value of 6.6 g m^{-2} in December of 1998, 1999, 2003, 2005, and 2006. In December 2001 and 2007, the $POC_{area,>35}$ value is about 6.4 g m^{-2}.

From Figure 3.10 one can also estimate net changes in the area-normalized POC stock. Within the entire Southern Ocean, the highest monthly accumulation rates are observed in the period between September and November, when the rates can exceed 0.3 g m^{-2} $month^{-1}$. The seasonal accumulation of POC over a period between August and December is on average 0.99 g m^{-2} (SD = 0.12 g m^{-2}) based on a 10-year data set. For the high-latitude region south of 55°S, the monthly accumulation rates of area-normalized POC stock are, on average, 0.43 g m^{-2} $month^{-1}$ during September-November period and 0.56 g m^{-2} $month^{-1}$ in November-December period. The maximum accumulation rate at latitudes > 55°S occurs between November and December 2006 and exceeds 0.7 g m^{-2} $month^{-1}$. The 10-year mean seasonal

accumulation of POC for a period from August through December south of 55°S is 1.64 g m^{-2} (SD = 0.25 g m^{-2}).

3.3.3. Potential Significance of Satellite Observations of POC

Monitoring the rates of change in organic carbon pools in the ocean at large basin scales using satellite-derived data such as those shown in Figures 3.9 and 3.10 provides a means for advancing a methodology to diagnose rates and fluxes of relevance to the global carbon cycle and to constrain the uncertainties of carbon budgets. As an example, the satellite-derived net accumulation or decline of POC in the upper ocean can be used in a carbon mass balance approach to constrain estimates of other components of the carbon budget, including export of organic carbon from the euphotic layer. The uncertainties and scarcity of various data required for rigorous mass balance calculations make this exercise difficult, in particular for large scale calculations within the Southern Ocean. Although such calculations are outside the scope of this paper, we can illustrate this point schematically using a simplified carbon mass balance approach that is based on biological drawdown of dissolved inorganic carbon (DIC) within the euphotic layer.

Because of utilization and production of CO_2 during photosynthesis and respiration, biologically-mediated change in dissolved inorganic carbon $(\Delta DIC)_{bio}$ is equivalent to net community production, NCP, which is the difference between gross primary production, GPP, and total community respiration, R. The NCP process can result in: (i) the net change of POC stock in the euphotic zone, ΔPOC; (ii): the net change of DOC (dissolved organic carbon) stock, ΔDOC; and (iii) export of organic

carbon, POC_{exp} + DOC_{exp}, from the euphotic zone to the deep ocean, largely as sinking biogenic particles (i.e., POC_{exp}). Hence, we can write: GPP - R = ΔPOC + ΔDOC + POC_{exp} + DOC_{exp} or NPP - R_h = ΔPOC + ΔDOC + POC_{exp} + DOC_{exp}, where NPP is the net primary production and R_h the heterotrophic respiration (NPP = GPP - R_p where R_p is phytoplankton respiration). This simplified budget neglects the exchange of organic carbon laterally *via* advection and the contribution of calcium carbonate dynamics, and it also assumes that the export term represents the net vertical exchange between the euphotic zone and the underlying layer. The accumulation, decline, and export of POC generally exert strong control on the NCP balance. In particular, during time periods of enhanced seasonal phytoplankton growth, the large impact of biology on the carbon budget is typically associated with accumulation and export of POC.

As an example of such simplified analysis, we can compare our satellite-based estimates of ΔPOC obtained from Figure 3.10 with large-scale satellite-based estimates of NPP in the Southern Ocean during the most productive months. Large-scale estimates of other components of carbon mass balance are generally not available or exhibit significant range, so the pursuit of rigorous closure of mass balance is difficult at this time. There have been several studies utilizing satellite data to estimate distributions of primary production in the Southern Ocean [*Arrigo et al*., 1998; *Moore and Abbott*, 2000; *Arrigo et al*., 2008]. For example, at the peak of the productive season, the daily rates of NPP within the 100 m upper layer of the pelagic province of the Southern Ocean south of 50°S were estimated to range from 300 to 400 mg C m^{-2} day^{-1} [*Arrigo et al*., 2008]. Although regional estimates of production

within the marginal ice zone and shelf provinces can be higher, especially during spring phytoplankton blooms, the size of these provinces is much smaller than the pelagic province. Thus, the estimates of area-normalized production for the pelagic province obtained by Arrigo and co-workers are approximately representative of the entire high-latitude portion of the Southern Ocean, and they can be compared to our POC data for the region south of 55^{o}S. We also note that at the December seasonal peak, other available large-scale estimates of NPP within the high-latitude regions south of the Polar Front (including Permanently Open Ocean Zone, Marginal Ice Zone, and Seasonal Ice Zone) are close to 10 g C m^{-2} month^{-1} (see Plate 7 in *Moore and Abbott*, 2000). This result is consistent with the range of daily rates obtained by Arrigo and co-workers.

Compared to the productivity estimates, it is remarkable that the highest seasonal accumulation rates, ΔPOC, in the high-latitude region south of 55^{o}S based on our time-series of monthly data in Figure 10 are, on average, only about 19 mg C m^{-2} day^{-1}. These rates are observed in the November-December period. The maximum POC accumulation rates of 24 mg C m^{-2} day^{-1} were observed in 2006.

An important result from this comparison of ΔPOC and NPP is that the POC accumulation rates are less than 10% of net primary production within the high-latitude portion of the Southern Ocean during the most productive part of the season. To support this comparison, we also verified that our area-normalized accumulation rates of POC are nearly the same regardless of whether we use the region south of 55^{o}S or south of 50^{o}S (the latter was used in the study of primary production by Arrigo and co-workers). Similar results indicating that ΔPOC is a small percentage of NPP,

is obtained by comparing our estimates of ΔPOC representing the entire Southern Ocean during the most productive period (which are generally less than 12 mg C m^{-2} day^{-1}) with primary production estimates for oceanic regions south of 35°S (see Plate 7 in *Moore and Abbott*, 2000).

Given that ΔPOC is less than 10% of NPP, the major fraction (>90%) of NPP according the mass balance approach must be accounted for by the sum of ΔDOC, POC_{exp}, DOC_{exp}, and R_h. In open ocean regions away from land such as most of the Southern Ocean, a significant portion of the DOC pool is derived from local primary production. As a result, biologically refractory and semilabile DOC can accumulate in the surface layer where it is then available for export *via* convective mixing and deep water formation [e.g., *Duursma*, 1963; *Carlson et al*., 1994; *Hansell et al*., 2002]. It has been shown, for example, that during the austral summer in the eutrophic system of the Ross Sea, the fraction of net community production (NCP) accumulating in the upper 150 m as DOC ranges from about 3 to 37% with an average of 14% [*Hansell and Carlson*, 1998]. During periods of maximum accumulation of total organic carbon in the Ross Sea, ΔPOC was shown to account for most of this accumulation, and not ΔDOC [*Carlson et al*., 2000]. In the context of our comparative analysis of large-scale estimates, one may expect that ΔDOC probably does not exceed 10% of NPP. Therefore, approximately 80% or more of NPP during the most productive months within the upper water column of the Southern Ocean appears to be partitioned as the sum of remineralization (R_h) and export (POC_{exp} + DOC_{exp}).

The existing data also suggest that both respiration and export terms can be large or dominant. For example, typical estimates of biological carbon export for open ocean waters of the Southern Ocean during late spring and summer months range between 150 and 300 mg C m^{-2} day^{-1} [e.g., *MacCready and Quay*, 2001 and references therein]. The estimates of community respiration, R, in the mixed layer of the Polar Front region in the Indian Ocean sector during early spring were observed in the range 180 - 420 mg C m^{-2} day^{-1} [*Aristegui et al.*, 2002]. Measurements during late spring and summer months in the Pacific sector showed even higher rates of community respiration and suggested a significant contribution of phytoplankton respiration [*Dickson and Orchardo*, 2001]. These respiration and export data are supportive of our satellite-derived POC in a qualitative sense. Whereas the export and respiration rates represent a large fraction or are comparable to the magnitude of NPP, our data indicate that a small fraction of NPP (<10%) accumulates as POC. As there exists significant physical and biological heterogeneity within the Southern Ocean [e.g., *Patterson*, 1985; *Gille and Kelly*, 1996; *Constable et al*., 2003; *Longhurst,* 1998], these large-scale estimates of low accumulation of POC during the productive season are, however, not necessarily representative of the Southern Ocean on regional scales. In some Antarctic waters with extremely intense seasonal phytoplankton blooms, for example in the Ross Sea, the POC accumulation can represent a much larger fraction of primary production [*Carlson et al*., 2000; *Gardner et al*., 2000].

3.4. Conclusions

In this study we apply an empirical remote-sensing algorithm for estimating surface POC concentration from ocean color in the Southern Ocean. Using our algorithm based on the blue-to-green reflectance band ratio, we demonstrate variability in POC within the Southern Ocean on seasonal and interannual time scales during a decade of SeaWiFS satellite mission. Our results show that surface POC concentrations in the Southern Ocean (i.e. at latitudes south of 35^{o}S) generally fall within the range of low to moderate values, from about 30 to 120 mg m^{-3}. On a whole basin scale, the monthly means are mostly between 70 to 80 mg m^{-3} and the probability of occurrence of POC concentrations above 200 mg m^{-3} is very low (Figures 3.5 and 3.6a). The seasonal signal in POC is weakest at lower latitudes within the Sub-Antarctic Zone and most pronounced at higher latitudes (>55^{o}S).

Our estimates of the total area-integrated stock of water column POC in the upper 100 m of the Southern Ocean show no clear evidence for a long-term trend in the POC stock during the examined 10-year period from 1997 through 2007. The seasonal variations range from a maximum of 0.6 Pg of carbon in December to a winter minimum, which is uncertain primarily due to incomplete coverage of the ocean area with valid satellite data (Figure 3.9). We estimate, however, that the winter minimum occurring during the June-August period is within a range of 0.24-0.51 Pg, and probably closer to the upper limit value. During the seasonal maximum (December), the three regions, the 35^{o}-45^{o}S latitudinal band, the 45^{o}-55^{o}S band, and the region south of 55^{o}S, each contribute approximately 0.2 Pg to the total area-integrated stock of POC within the upper 100 m of the Southern Ocean. The seasonal

range of area-normalized water column POC for the entire Southern Ocean (>35^{o}S) is between 5.5 and 6.6 g m^{-2}, and for the high-latitude region (>55^{o}S) from 5 g m^{-2} to 7 g m^{-2} (Figure 3.10). The high-latitude region south of 55^{o}S provides a dominant contribution to the accumulation of POC within the Southern Ocean during the productive period of the season between September and December when the net increase in POC occurs. Then, in these high-latitude waters, the area-normalized POC accumulates at rates between 0.2 and 0.7 g m^{-2} month^{-1}. The comparison of these rates with large-scale satellite-based estimates of primary production indicates that only a small fraction (<10%) of production accumulates as POC.

Despite limitations of optical remote sensing at high latitudes, especially during winter months, the presented capability to monitor POC from satellite observations will be important to further extend our understanding of the role of POC in ecosystem and carbon dynamics in the Southern Ocean and ecological responses to changing climate. As changing climate and environmental conditions can affect critical carbon fluxes and partitioning of carbon among various reservoirs, the analysis based on satellite observations presented in this study establishes a reference point for potential future change in the pool of particulate organic carbon in the Southern Ocean. Also, because the change in POC stock is one of the components of net community production that describes the carbon mass balance associated with biological processes in the surface ocean, the time-series satellite observations of POC can advance an understanding of key questions of the biologically-mediated carbon cycle, such as whether oceanic biota act as sources or sinks of carbon and the capacity of the oceanic biological pump to draw down increased levels of atmospheric CO_2.

Chapter 3, in full, is a reprint of material as it appears in Journal of Geophysical Research, Oceans 2010, Allison, David B., Stramski, Dariusz, Mitchell, B. Greg. The dissertation author was the primary investigator and author of this paper.

3.5. Acknowledgments

This work was funded by NASA Ocean Biology and Biogeochemistry Program (Grant NNG04GO02G awarded to D.S), NSF Chemical Oceanography Program (OCE-0324680 to D.S.), NASA (G2004-2983 to B.G.M), NSF (ANT0444134 to B.G.M), NASA and NSF (NAG5-7100 and OPP 98-023836 to D.S. and B.G.M.) as part of the US JGOFS Antarctic Environment Southern Ocean Process Study, NSF Graduate Student Fellowship (awarded to D.B.A.), the NOAA Fisheries' U.S. Antarctic Marine Living Resources (AMLR) Program, and the NASA SIMBIOS program. We are grateful to Rick Reynolds, Mati Kahru, Haili Wang, and John Wieland for their invaluable contributions to the execution of our field program and data processing. We also thank the SeaWiFS Project and the NASA's Goddard Earth Sciences Data and Information Services Center DAAC (NASA's Ocean Color Website) for the production and distribution of ocean color data. The technical staff of Antarctic Support Associates, scientists, officers, and crews of the R/V *Nathaniel B. Palmer*, R/V *Roger Revelle*, R/V *Yuzhmorgeologiya*, and R/V *Laurence M. Gould* are acknowledged for providing logistical support and their help onboard during the field work. The analysis of samples for particulate organic carbon was made at Marine Science Institute Analytical Laboratory, University of California at Santa Barbara.

3.6. Figures

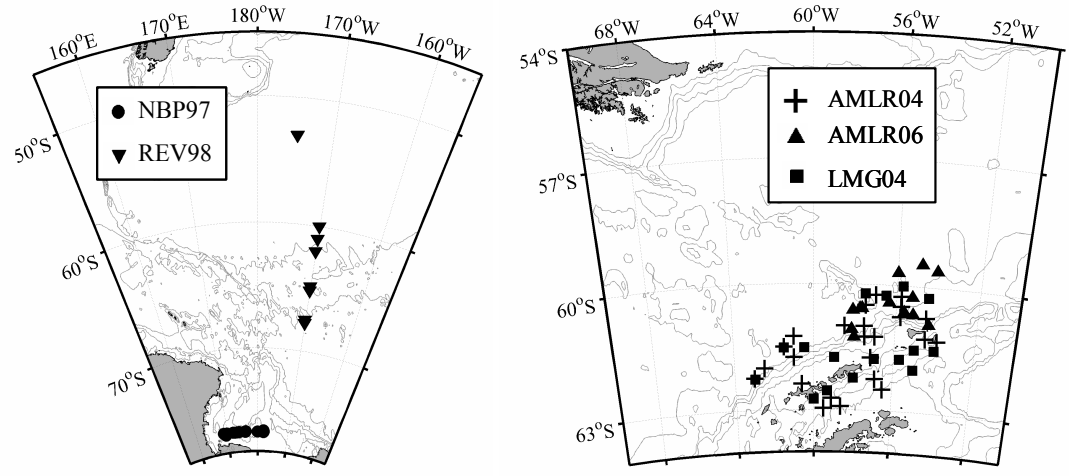

Figure 3.1. Locations of stations in the Southern Ocean where the optical and POC measurements used in the development of POC algorithms were made. The NBP97 stations were visited during the U.S. Joint Global Ocean Flux Study (JGOFS) cruise (NBP9711) in the Ross Sea in November-December of 1997. The REV98 stations represent the JGOFS cruises REV9801 and REV9802 which took place from January through March 1998. The AMLR stations were visited during the January-March period in 2004 and 2006 on the AMLR04 and AMLR06 cruises of the NOAA Fisheries' U.S. Antarctic Marine Living Resources Program. Additionally, one set of data was collected during the 2004 AMLR season by a National Science Foundation sponsored cruise LMG0402.

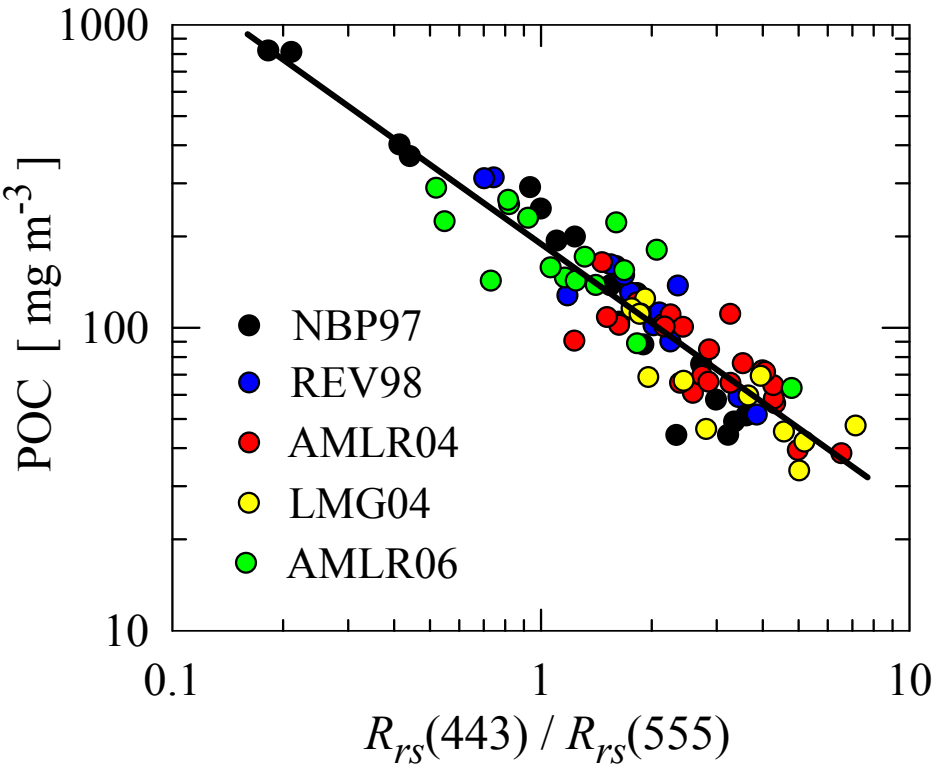

Figure 3.2. Relationship between surface concentration of particulate organic carbon, POC, and the blue-to-green band ratio of remote-sensing reflectance, $R_{rs}(443)/R_{rs}(555)$. The data points from several cruises are shown as indicated (the REV98 data are from two cruises REV9801 and REV9802). The power function fit to all data is also shown (solid black line).

Figure 3.3a. The multiyear monthly mean values of POC concentration in the surface waters within the Southern Ocean. Each map was obtained by averaging monthly data collected over a 10 year time period as indicated. The austral spring-summer months are shown. The POC concentrations were derived by applying our algorithm based on the $R_{rs}(443)/R_{rs}(555)$ band ratio to the Level 3B standard binned data of SeaWiFS-derived remote-sensing reflectance. For mapping of surface POC concentrations, the data are projected to an equidistant azimuthal projection. Areas in white represent no satellite data due to winter darkness, sea ice cover, persistent cloudiness, atmospheric correction failure, or other algorithm failure conditions (e.g., low solar elevation, negative R_{rs}). The latitude gridlines are shown for 35^{o}S, 45^{o}S, 55^{o}S, and 65^{o}S. The meridians 0^{o}-180^{o} and 90^{o}E-90^{o}W are also shown.

(a) spring - summer

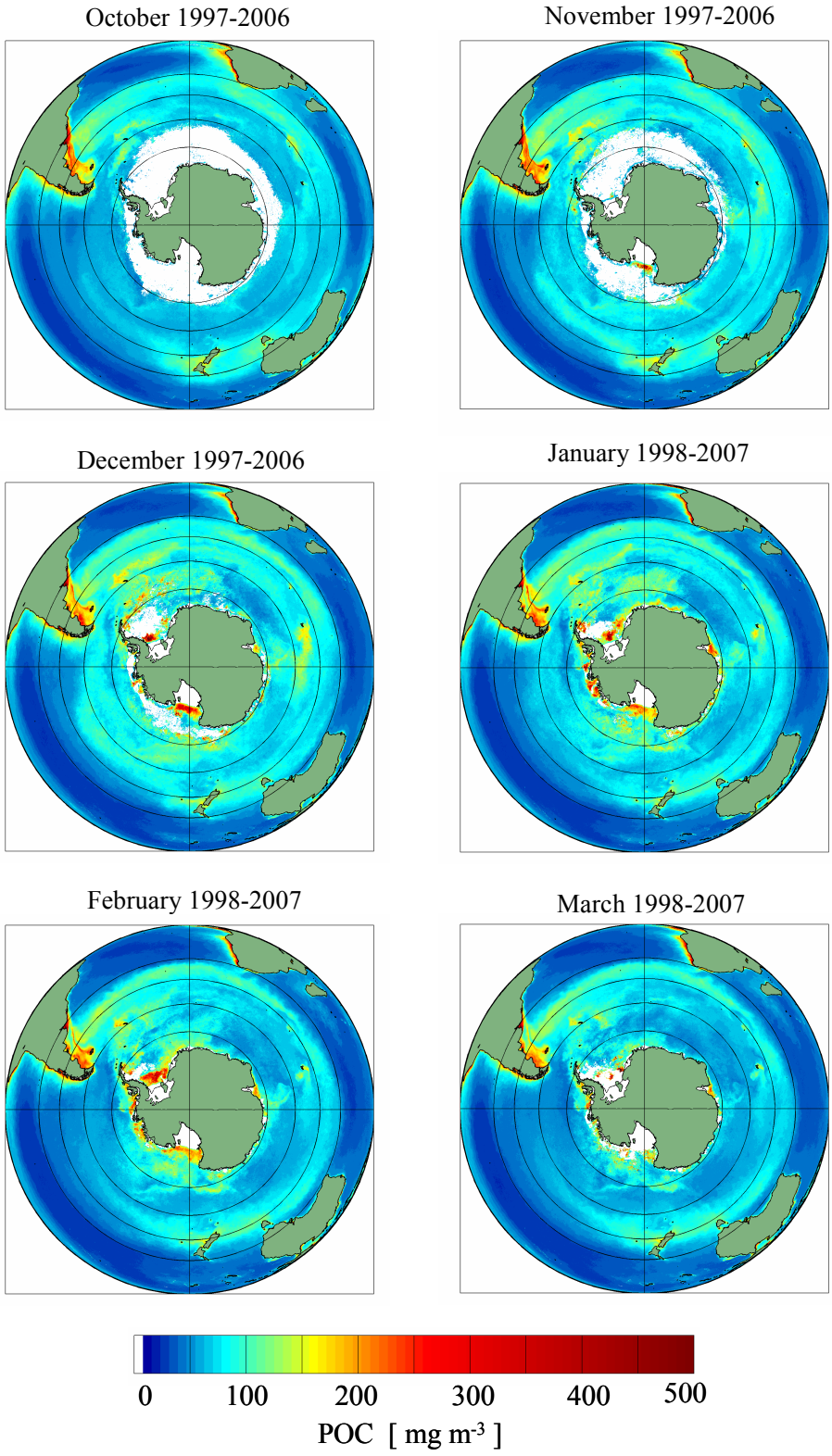

Figure 3.3b. The multiyear monthly mean values of POC concentration in the surface waters within the Southern Ocean. Each map was obtained by averaging monthly data collected over a 10 year time period as indicated. The autumn-winter months are shown. The POC concentrations were derived by applying our algorithm based on the $R_{rs}(443)/R_{rs}(555)$ band ratio to the Level 3B standard binned data of SeaWiFS-derived remote-sensing reflectance. For mapping of surface POC concentrations, the data are projected to an equidistant azimuthal projection. Areas in white represent no satellite data due to winter darkness, sea ice cover, persistent cloudiness, atmospheric correction failure, or other algorithm failure conditions (e.g., low solar elevation, negative R_{rs}). The latitude gridlines are shown for 35^{o}S, 45^{o}S, 55^{o}S, and 65^{o}S. The meridians 0^{o}-180^{o} and 90^{o}E-90^{o}W are also shown.

(b) autumn - winter

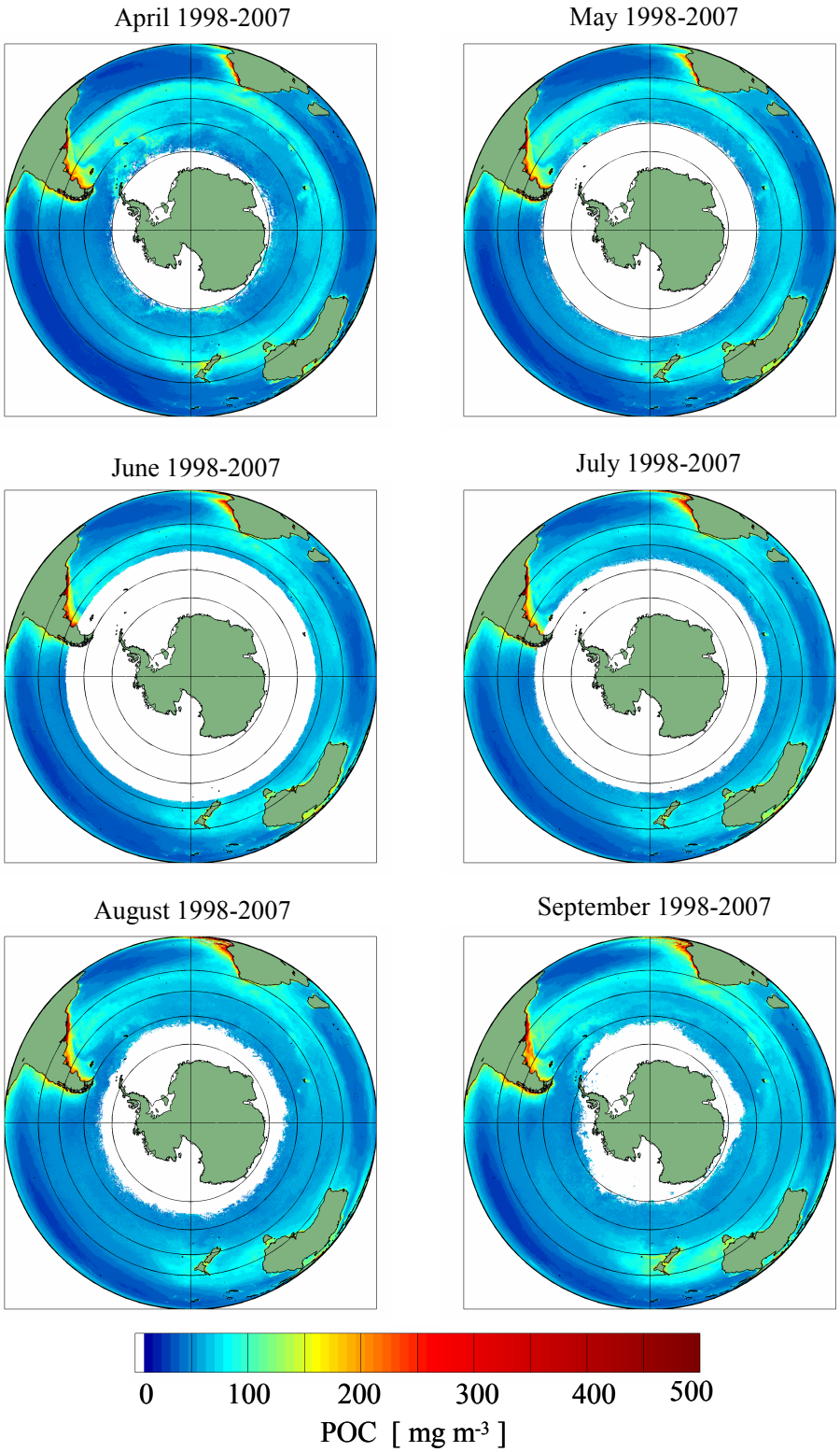

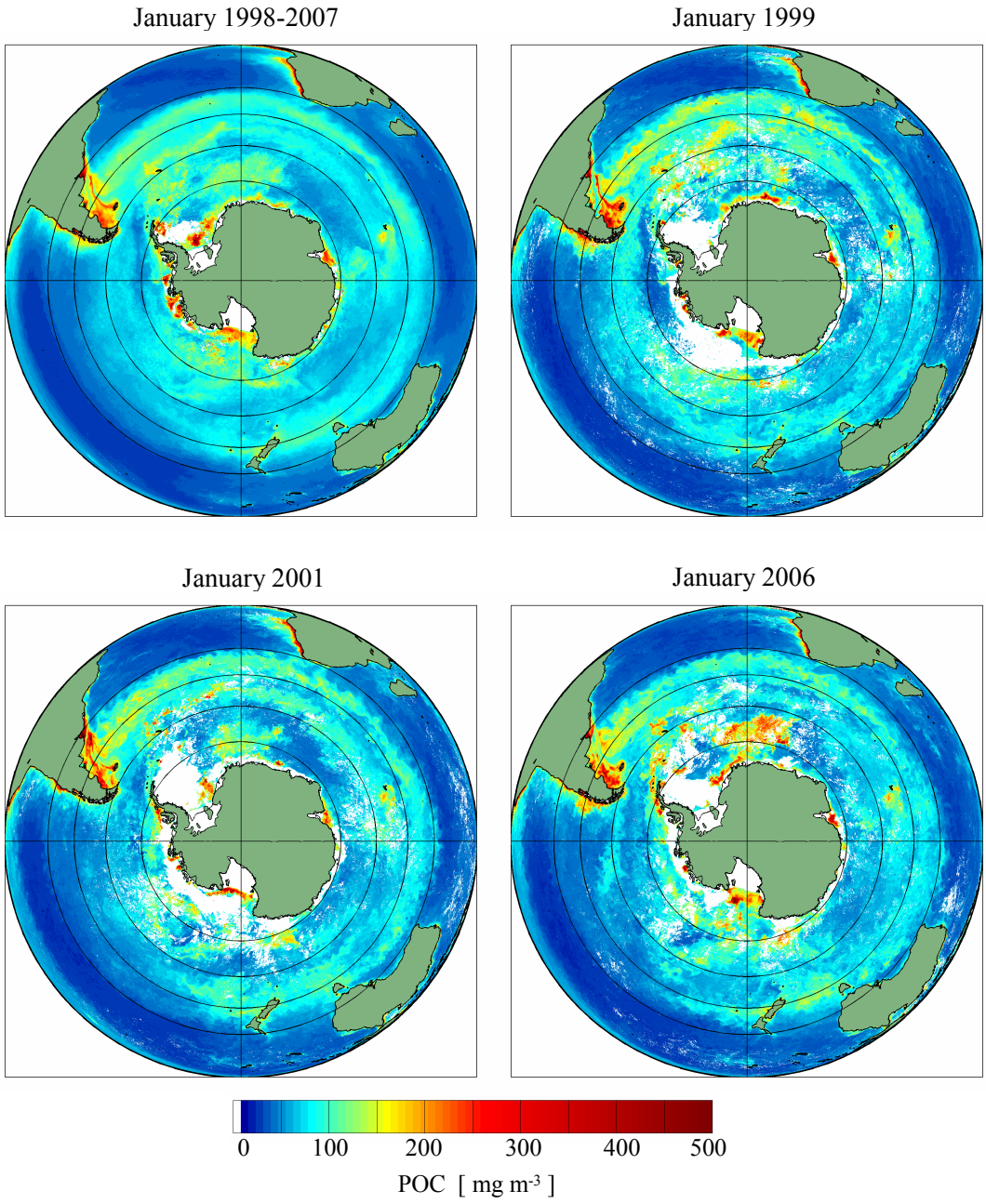

Figure 3.4. Comparison of the monthly mean distribution of POC concentration in the surface waters within the Southern Ocean for the month of January based on averaging data from a time period between January 1998 and January 2007, with the monthly mean distributions for the month of January in three example years: 1999, 2001, and 2006. Areas in white represent no valid satellite data. The latitude gridlines are shown for 35°S, 45°S, 55°S, and 65°S. The meridians 0°-180° and 90°E-90°W are also shown.

Figure 3.5. The probability density functions of the surface POC concentration within the Southern Ocean (south of 35^{o}S) for each month based on the month-by-month analysis of SeaWiFS data over a 10-year period from October 1997 through September 2007. These distributions were created using bins of constant width (0.025) for the log-transformed POC. For a given month (e.g., January), the number of occurrences of POC values within every bin was counted and summed up for all 10 years (i.e., January 1998, January 1999, January 2000, etc..., January 2007). To determine the final value of the probability density at a mid-point of a given bin, the ratio of the total count within the bin to the overall total count summed up over all bins was multiplied by 100 and divided by the bin width. In these calculations, the bin width represents the difference in POC between the two end-points of the bin expressed as ordinary values of POC (i.e., not logarithmically transformed). For example, for a bin whose mid-point is POC = 10 mg m^{-3} the bin width is about 0.576 mg m^{-3}, and for the mid point of POC = 100 mg m^{-3} the bin width is about 5.76 mg m^{-3}.

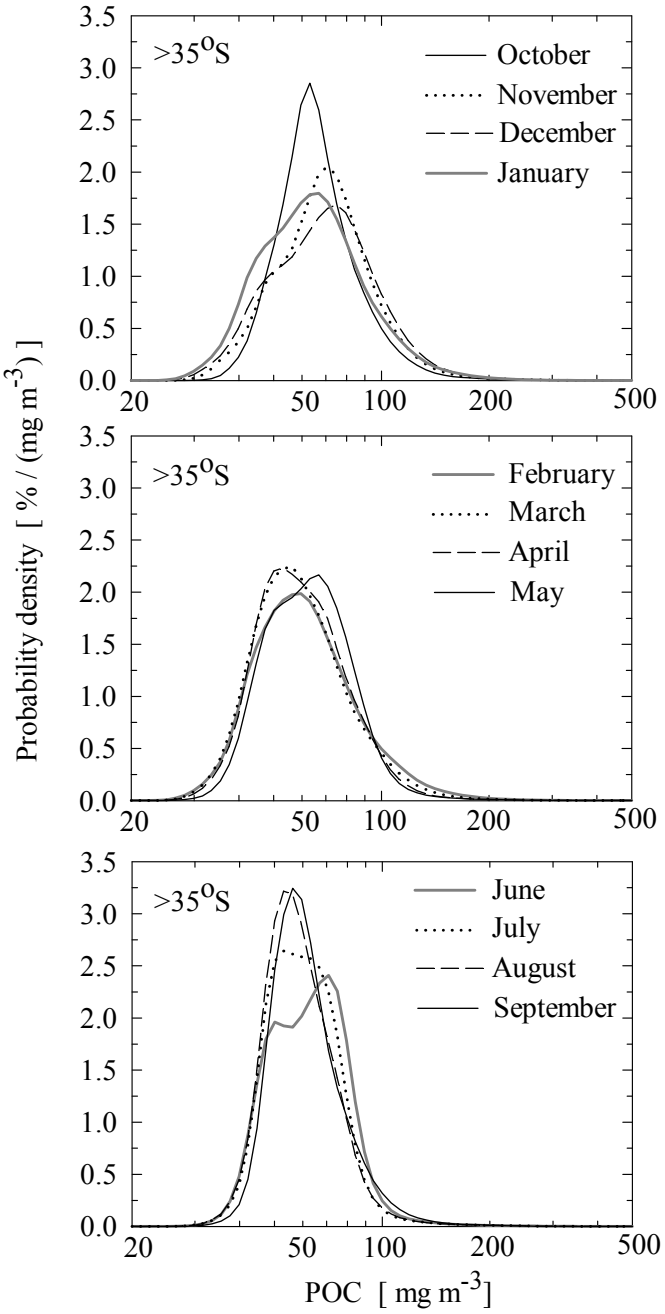
>35°S
October
November
December
January
>35°S
February
March
April
May
>35°S
June
July
August
September
Probability density [% / (mg m-3)]
POC [mg m-3]
0.0
0.5
1.0
1.5
2.0
2.5
3.0
3.5
20
50
100
200
500

Figure 3.6. (a) Seasonal progression of monthly mean (solid circles) and mode values of surface POC concentration within the entire Southern Ocean (south of 35^{o}S) corresponding to the probability density functions presented in Figure 5. The standard deviation is also shown. (b) Comparison of the monthly mean POC concentration from panel (a) with similar monthly means for the three latitudinal zones: 35^{o}-45^{o}S, 45^{o}-55^{o}S, and south of 55^{o}S. (c) Monthly mean values of the ratio of ocean area with valid ocean color data pixels to the total ocean area for the entire Southern Ocean and the three latitude bands (see symbols in panel b) based on the month-by-month analysis of SeaWiFS data over a 10-year period from October 1997 through September 2007.

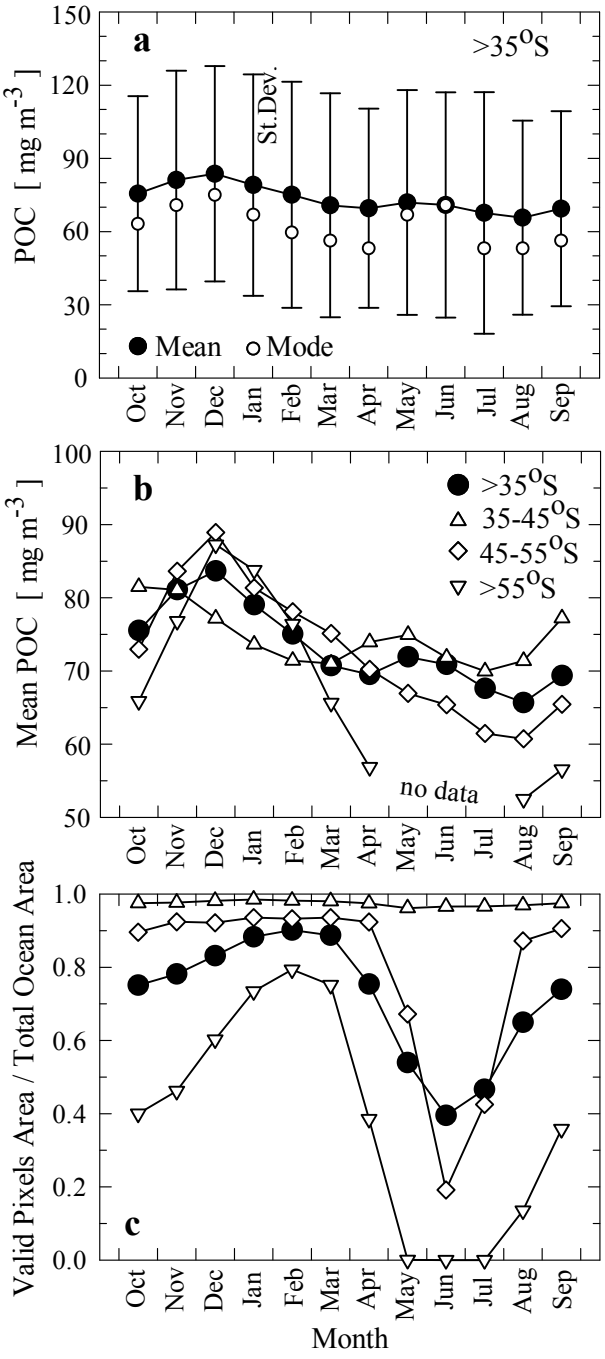
a
>35°S
St.Dev.
POC [mg m-3]
Mean
Mode
b
>35°S
35-45°S
45-55°S
>55°S
Mean POC [mg m-3]
no data
c
Valid Pixels Area / Total Ocean Area
Month
Oct
Nov
Dec
Jan
Feb
Mar
Apr
May
Jun
Jul
Aug
Sep

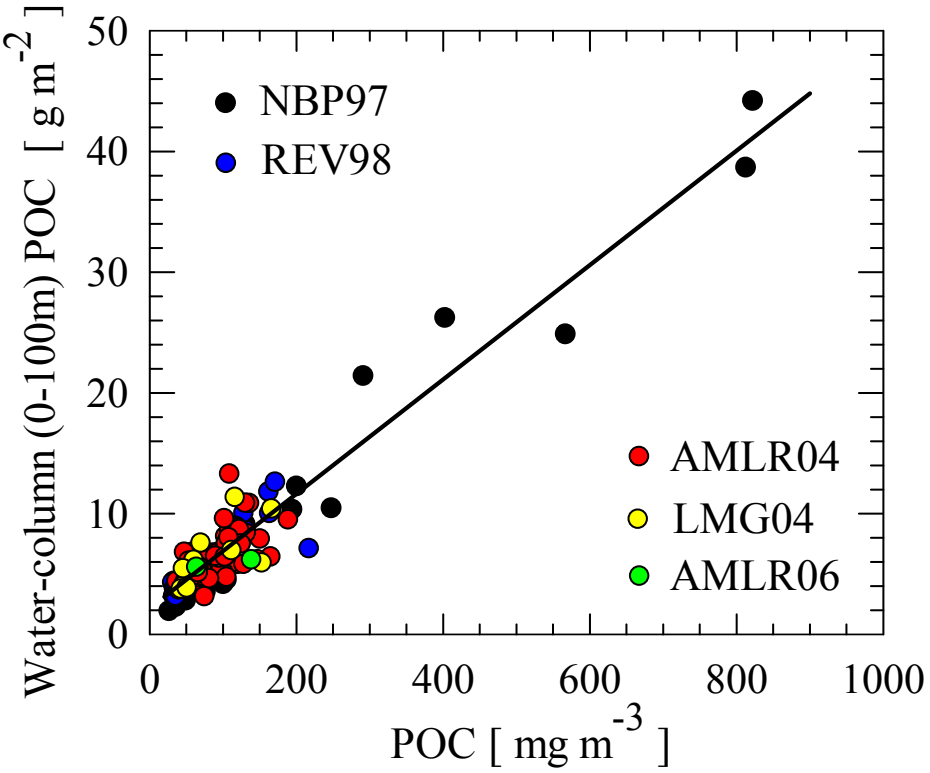

Figure 3.7. The relationship between the water column POC integrated from the sea surface to 100 m depth and the surface concentration of POC obtained from our field data collected on several cruises in the Southern Ocean (as shown in Figure 1). The best fit linear equation is: POC (water column integrated in g m^{-2}) = 0.04737 (±0.00141) x POC (surface concentration in mg m^{-3}) + 2.16672 (±0.22816). The standard errors of the estimates of the regression coefficients are given in parentheses, the squared correlation coefficient is 0.91, and the number of observations is 115.

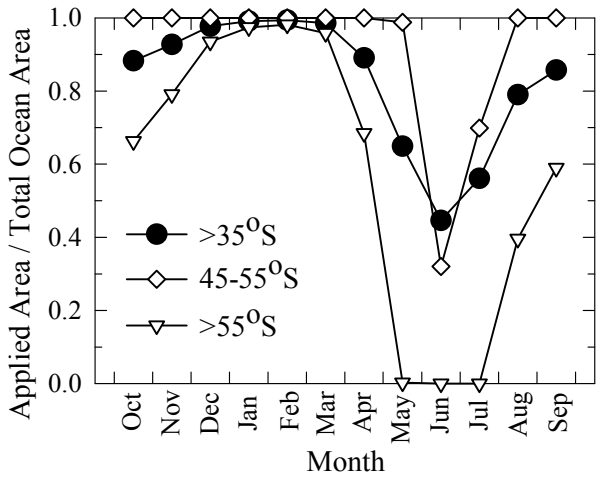

Figure 3.8. Monthly mean values of the ratio of the applied area to the total ocean area within the entire Southern Ocean (> 35°S) and the two major regions (45°-55°S and south of 55°S) based on averaging over a 10-year period from October 1997 through September 2007. The data for the latitude band 35°-45°S are not displayed because the values in that region are 1 for all months.

Figure 3.9. Monthly mean values of area-integrated stock of POC within the 100 m upper water column based on averaging over a 10-year period from October 1997 through September 2007 for (a) the entire Southern Ocean (> 35°S), (b) the 35°-45°S and 45°-55°S regions, and (c) the region south of 55°S. The open symbols represent the calculations for the applied ocean area. The grey solid symbols represent the calculations scaled up to the total ocean area (see text for details). For the 35°-45°S region these two calculations yield identical results for all months. There is no data at latitudes > 55°S for May, June, and July.

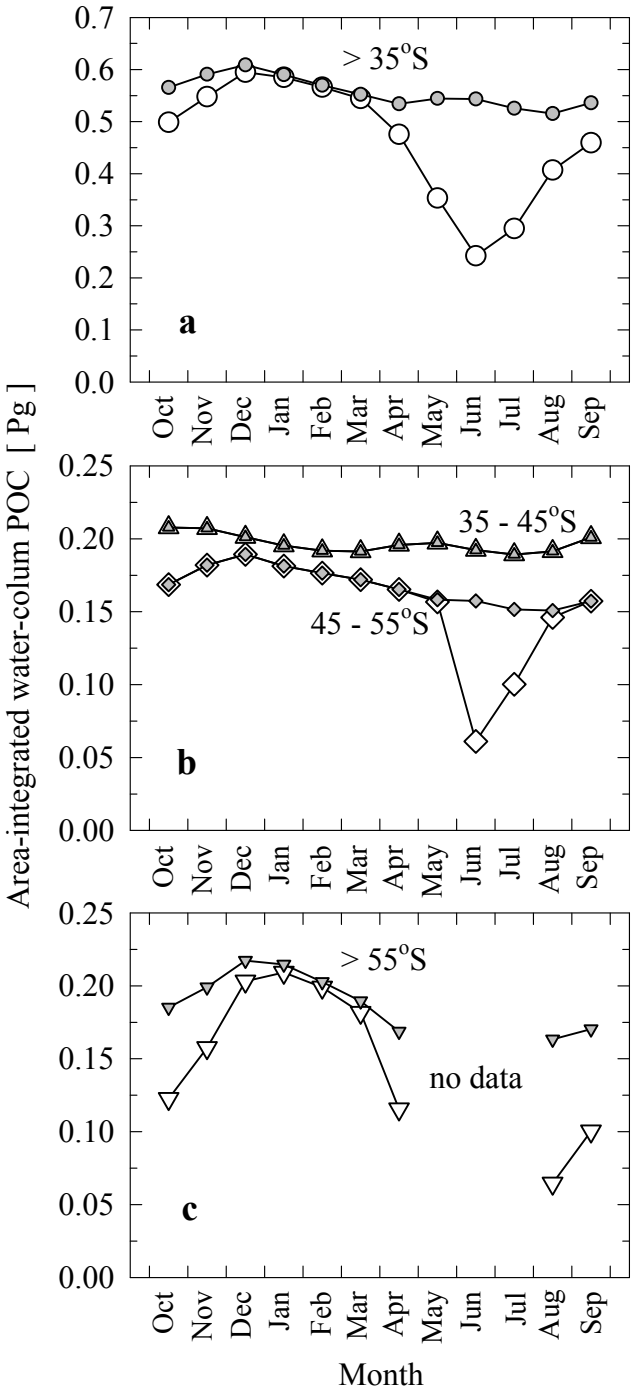
Area-integrated water-colum POC [Pg]
> 35°S
a
35 - 45°S
45 - 55°S
b
> 55°S
no data
c
Oct
Nov
Dec
Jan
Feb
Mar
Apr
May
Jun
Jul
Aug
Sep
Month

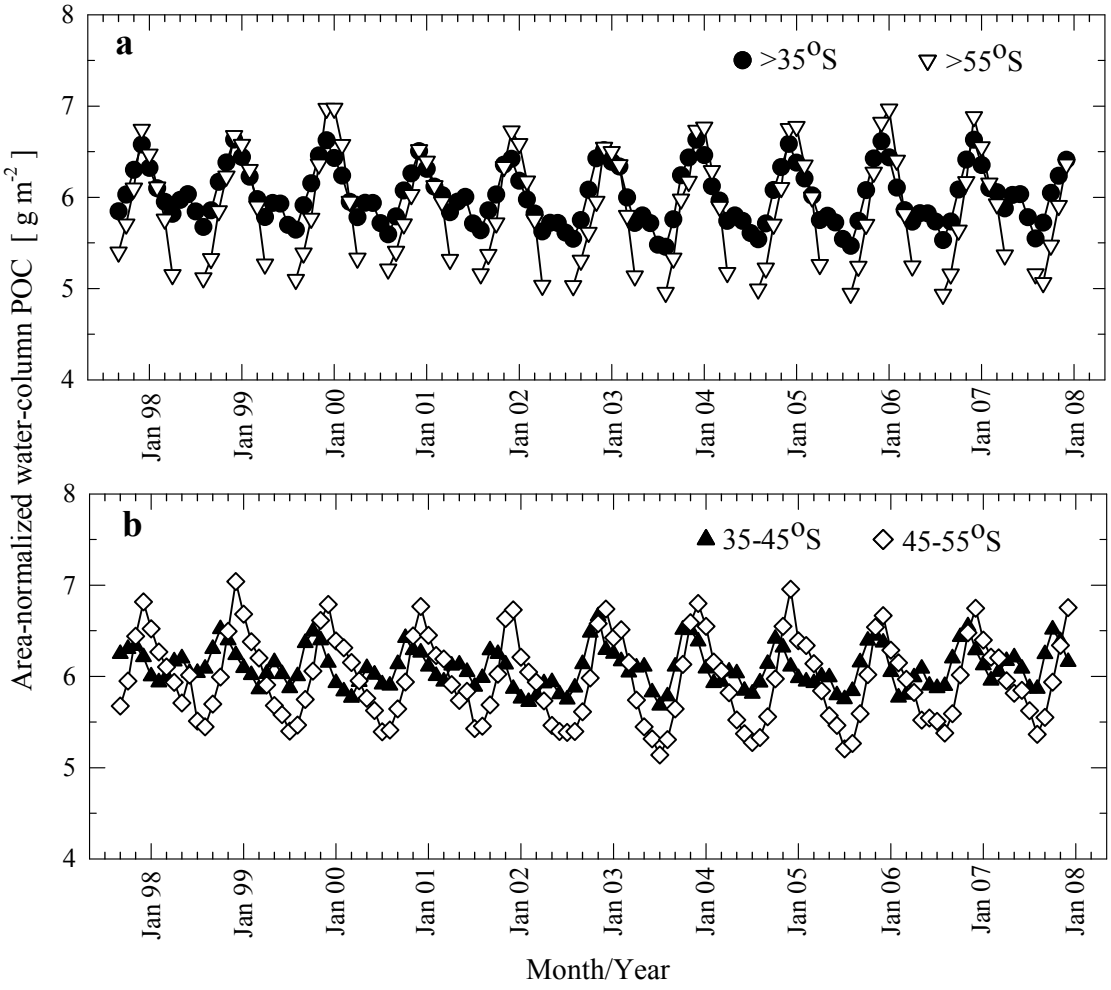

Figure 3.10. Time-series of monthly mean values of area-normalized stock of POC within the 100 m upper water column within the entire Southern Ocean (> 35°S) and the three major regions 35°-45°S, 45°-55°S, and south of 55°S. There is no data at latitudes > 55°S for May, June, and July.

3.7. Tables

Table 3.1. The monthly mean values (in units of Pg of carbon) of the area-integrated stock of POC within the top 100 m of the ocean derived from satellite observations of ocean color. These results were calculated by averaging data from a 10-year period from October 1997 through September 2007. The percent values in parenthesis represent the coefficient of variation due to interannual variability. The results are shown for the entire basin of the Southern Ocean and the three regions within the Southern Ocean. The presented values of the area-integrated stock of POC correspond to the entire ocean area within each region, and were calculated by scaling up the calculations based on the so-called "applied" ocean area (see text for details of the methods).

Month	*Southern Ocean >35°S*	*35 - 45°S*	*45 - 55°S*	*> 55°S*
January	0.591 (1.3%)	0.195 (2.2%)	0.181 (3.5%)	0.215 (3.1%)
February	0.571 (1.6%)	0.192 (2.2%)	0.176 (3.0%))	0.203 (2.3%)
March	0.553 (1.2%)	0.191 (1.8%)	0.172 (2.0%)	0.190 (1.5%)
April	0.530 (1.2%)	0.196 (1.4%)	0.165 (2.3%)	0.169 (2.0%)
May	0.544 (1.7%)	0.197 (1.4%)	0.158 (2.8%)	no data
June	0.543 (2.3%)	0.192 (1.9%)	0.157 (4.2%)	no data
July	0.525 (2.0%)	0.189 (1.7%)	0.152 (3.0%)	no data
August	0.505 (1.3%)	0.191 (1.5%)	0.151 (1.1%)	0.163 (2.0%)
September	0.528 (1.2%)	0.201 (1.4%)	0.157 (1.2%)	0.170 (2.1%)
October	0.561 (1.1%)	0.208 (1.4%)	0.168 (0.9%)	0.185 (1.9%)
November	0.588 (1.0%)	0.207 (2.3%)	0.182 (2.9%)	0.199 (2.1%)
December	0.607 (1.1%)	0.201 (2.4%)	0.189 (1.7%)	0.217 (2.0%)

3.8. References

Aristegui, J., M. Denis, J. Alumnia, and M. F. Montero (2002), Water-column remineralization in the Indian sector of the Southern Ocean during early spring, *Deep-Sea Res., Part II, 49*, 1707-1720.

Arrigo, K. R., and C. R. McClain (1994), Spring phytoplankton production in the western Ross Sea, *Science, 266*, 261-263.

Arrigo, K. R., and G. L. van Dijken (2003), Phytoplankton dynamics within 37 Antarctic coastal polynya systems, *J. Geophys. Res., 108(C8)*, 3271, doi:10.1029/2002JC001739.

Arrigo, K. R., G. L. van Dijken, and S. Bushinsky (2008), Primary production in the Southern Ocean, 1997-2006, *J. Geophys. Res., 113*, C08004, doi:10.1029/2007JC004551.

Arrigo, K. R., D. Worthen, A. Schnell, and M. P. Lizotte (1998), Primary production in Southern Ocean waters, *J. Geophys. Res., 103*, 15587-15600.

Banse, K. (1996), Low seasonality of low concentrations of surface chlorophyll in the subantarctic water ring: underwater irradiance, iron or grazing?, *Prog. Oceanogr., 37*, 241-291.

Bates, N. R., D. A. Hansell, and C. A. Carlson (1998), Distribution of CO_2 species, estimates f net community production, and air-sea CO_2 exchange in the Ross Sea polynya, *J. Geophys, Res., 103*, 2883-2896.

Belkin, I. M., and A. L. Gordon (1996), Southern Ocean fronts from the Greenwich meridian to Tasmania, *J. Geophys. Res., 101*, 3675-3696.

Buesseler, K. O., L. Ball, J. Andrews, J. K. Cochran, D. J. Hirschberg, M. P. Bacon, A. Fleer, and M. Brzezinski (2001), Upper ocean export of particulate organic carbon and biogenic silica in the Southern Ocean along 170^{o}W, *Deep-Sea Res., Part II, 48*, 4275-4297.

Carlson, C. A., H. W. Ducklow, and A. F. Michaels (1994), Annual flux of dissolved organic carbon from the euphotic zone in the Northwestern Sargasso Sea, *Nature, 371*, 405-408.

Carlson, C. A., D. A. Hansell, E. T. Peltzer, and W. O. Smith Jr (2000), Stocks and dynamics of dissolved and particulate organic matter in the southern Ross Sea, *Deep-Sea Res., Part II, 47*, 3201-3225.

Comiso, J. C., C. R. McClain, C. W. Sullivan, J. P. Ryan, and C. L. Leonard (1993), Coastal Zone Color Scanner pigment concentrations in the Southern Ocean and relationships to geophysical surface features, *J. Geophys. Res.*, *98*, 2419-2451.

Constable, A. J., S. Nicol, and P. G. Strutton (2003), Southern Ocean productivity in relation to spatial and temporal variation in the physical environment, *J. Geophys. Res., 108(C4)*, 8079, doi:10.1029/2001JC001270.

Deacon, G. E. R. (1982), Physical and biological zonation in the Southern Ocean, *Deep-Sea Res., 29*, 1-15.

Dickson, M.-L., and J. Orchardo (2001), Oxygen production and respiration in the Antarctic Polar Front region during the austral spring and summer, *Deep-Sea Res., Part II*, 4101-4126.

Duursma, E. K. (1963), The production of dissolved organic matter in the sea as related to the primary gross production of organic matter, *Neth. J. Sea Res., 2*, 85-94.

Eppley, R. W. (1989), New production: History, methods, problems, in *Productivity of the Ocean: Present and Past*, edited by W. H. Bergeret et al., pp. 85-97, John Wiley, New York.

Gardner, W. D., A. V. Mishonov, and M. J. Richardson (2006), Global POC concentrations from *in situ* and satellite data, *Deep-Sea Res., Part II, 53*, 718-740.

Gardner, W. D., M. J. Richardson, and W. O. Smith, Jr. (2000), Seasonal patterns of water column particulate organic carbon and fluxes in the Ross Sea, Antarctica, *Deep-Sea Res., Part II, 47*, 3423-3449.

Gille, S. T. (1994), Mean sea surface height of the Antarctic Circumpolar Current from Geosat data: Method and application, *J. Geophys. Res.*, *99*, 18255-18273.

Gille, S. T., and K. A. Kelly (1996), Scales of spatial and temporal variability in the Southern Ocean, *J. Geophys. Res.*, *101*, 8759-8773.

Hansell, D. A., and C. A. Carlson (1998), Net community production of dissolved organic carbon, *Global Biogeochem. Cycles, 12*, 443-453.

Hansell, D. A., C. A. Carlson, and Y. Suzuki (2002), Dissolved organic carbon export with North Pacific Intermediate Water formation, *Global Biogeochem. Cycles, 16, 1007*, doi: 10.1029/2000GB001361

Honjo, S., R. Francois, S. Manganini, J. Dymond, and R. Collier (2000), Particle fluxes to the interior of the Southern Ocean in the western Pacific sector along 170°W, *Deep-Sea Res., Part II, 47*, 3521-3548.

Kishino, M., M. Takahashi, N. Okami, and S. Ichimura (1985), Estimation of the spectral absorption coefficients of phytoplankton in the sea, *Bull. Mar. Sci., 37*, 634-642.

Knap, A., A. Michaels, A. Close, H. Ducklow, and A. Dickson, Eds. (1996), Protocols for the Joint Global Ocean Flux Study (JGOFS) Core Measurements, JGOFS Report Nr. 19 (Reprint of the IOC Manuals and Guides No. 29, UNESCO, Paris, 1994), 170 pp.

Knox, F., and M. B. McElroy (1984), Changes in atmospheric CO_2 - influence of the marine biota at high-latitude, *J. Geophys. Res., 89*, 4629-4637.

Le Quéré, C., et al. (2007), Saturation of the Southern Ocean CO_2 sink due to recent climate change, *Science, 316*, 1735-1738.

Loisel, H., E. Bosc, D. Stramski, K. Oubelkheir, and P.-Y. Deschamps (2001), Seasonal variability of the backscattering coefficient in the Mediterranean Sea based on satellite SeaWiFS imagery, *Geophys. Res. Lett.*, *28*, 4203-4206.

Longhurst, A. R. (1998), *Ecological Geography of the Sea*, 398 pp., Academic Press, San Diego, Calif.

Longhurst, A. R., and W. G. Harrison (1989), The biological pump: Profiles of plankton production and consumption in the upper ocean, *Prog. Oceanogr., 22*, 47-122.

MacCready, P., and P. Quay (2001), Biological export flux in the Southern Ocean estimated from a climatological nitrate budget, *Deep-Sea Res.*, *Part II*, *48*, 4299-4322.

Martin, J. H., S. E. Fitzwater, and R. M. Gordon (1991), Iron deficiency limits phytoplankton growth in Antarctic waters, *Global Biogeochem. Cycles, 4*, 5-12.

McClain, C. R., G. C. Feldman, and S. B. Hooker (2004), An overview of the SeaWiFS project and strategies for producing a climate research quality global ocean bio-optical time series, *Deep-Sea Res., Part II, 51*, 5-42.

McNeil, B. I., N. Metzl, R. M. Key, R. J. Matear, and A. Corbiere (2007), An empirical estimate of the Southern Ocean air-sea CO2 flux, *Global Biogeochem. Cycles, 21*, GB3011, doi:10.1029/2007GB002991.

Metzl, N., B. Tilbrook, and A. Poisson (1999), The annual fCO_2 cycle and the air-sea CO_2 flux in the sub-Antarctic Ocean, *Tellus, Ser. B, 51*, 849-861.

Mitchell, B. G., E. A. Brody, O. Holm-Hansen, C. McClain, and J. Bishop (1991), Light limitation of phytoplankton biomass and macronutrient utilization in the Soutehrn Ocean, *Limnol. Oceanogr*., 36, 1662-1677.

Mishonov, A. V., W. D. Gardner, and M. J. Richardson (2003), Remote sensing and surface POC concentration in the South Atlantic, *Deep Sea Res., Part II, 50*, 2997–3015.

Mobley, C. D. (1994), *Light and Water: Radiative Transfer in Natural Waters*, 592 pp., Academic Press, San Diego, Calif.

Moore, J. K. and M. R. Abbott (2000), Phytoplankton chlorophyll distributions and primary production in the Southern Ocean, *J. Geophys. Res., 105*, 28709-28722.

Moore, J. K., M. R. Abbott, and J. G. Richman (1999), Location and dynamics of the Antarctic Polar Front from satellite sea surface temperature data, *J. Geophys. Res.*, *104*, 3059-3073.

Mueller, J. L., G. S. Fargion, and C. R. McClain, Eds. (2003), Ocean Optics Protocols for Satellite Ocean Color Sensor Validation, Revision 4, Volume III: Radiometric Measurements and Data Analysis Protocols, *NASA/TM-2003-211621/Rev4-Vol. III*, 78 pp., NASA Goddard Space Flight Center, Greenbelt, Maryland.

O'Reilly, J. E, S. Maritorena, B. G. Mitchell, D. A. Siegel, K. L. Carder, S. A. Garver, M. Kahru, and C. R. McClain (1998), Ocean color chlorophyll algorithms for SeaWiFS, *J. Geophys. Res., 103*, 24937 - 24953.

O'Reilly, J. E., S. Maritorena, D. A. Siegel, M. C. O'Brien, D. Toole, B. G. Mitchell, M. Kahru, F. P. Chavez, P. Strutton, G. F. Cota, S. B. Hooker, C. R. McClain, K. L. Carder, F. Müller-Karger, L. Harding, A. Magnuson, D. Phinney, G. F. Moore, J. Aiken, K. R. Arrigo, R. Letelier, and M. Culver (2000), Ocean color chlorophyll *a* algorithms for SeaWiFS, OC2 and OC4: Version 4, *NASA Tech. Memo*, *2000-206892, vol. 11*, 9-27.

Orsi, A. H., T. Whitworth III, and W. D. Nowlin, Jr. (1995), On the meridional extent and fronts of the Antarctic Circumpolar Current, *Deep-Sea Res*. *I*, *42*, 641-673.

Pabi, S., and K. R. Arrigo (2006), Satellite estimation of marine particulate carbon in waters dominated by different phytoplankton taxa, *J. Geophys. Res., 110*, C10018, doi:10.1029/ 2005JC003137.

Parkinson, C. L. (2004), Southern Ocean sea ice and its wider linkages: insights revealed from models and observations, *Antarct. Sci., 16*, 387-400.

Parsons, T. R., Y. Maita, and C. M. Lalli (1984), *A Manual of Chemical and Biological Methods for Seawater Analysis*, 173 pp., Pergamon Press, Oxford, UK.

Patterson, S. L. (1985), Surface circulation and kinetic energy distributions in the Southern Hemisphere oceans from FGGE drifting buoys, *J. Phys. Oceanogr., 15*, 865-884.

Pollard, R. T., M. I. Lucas, and J. F. Read (2002), Physical controls on biogeochemical zonation in the Southern Ocean, *Deep-Sea Res., Part II, 49*, 3289-3305.

Pope, R. M. and E. S. Fry (1997), Absorption spectrum (380-700 nm) of pure water. II. Integrating cavity measurements, *Appl. Opt., 36*, 8710-8723.

Sabine, C. L., R. A. Feely, G. C. Johnson, P. G. Strutton, M. F. Lamb, and K. E. McTaggart (2004), A mixed layer carbon budget for the GasEx-2001 experiment, *J. Geophys. Res., 109*, C08S05, doi:10.1029/2002JC001747.

Sarmiento, J. L., et al. (2004), Response of ocean ecosystems to climate warming, *Global Biogeochem. Cycles, 18*, GB3003, doi:10.1029/2003GB002134.

Sarmiento, J. L., and J. C. Orr (1991), Three-dimensional simulations of the impact of Southern Ocean nutrient depletion on atmospheric CO_2 and chemistry, *Limnol. Oceanogr., 36*, 1928-1950.

Sarmiento, J. L., and J. R. Toggweiler (1984), A new model for the role of the oceans in determining atmospheric pCO_2, *Nature, 308*, 621–624.

Schlitzer, R. (2002), Carbon export fluxes in the Southern Ocean: results from inverse modeling and comparisons with satellite based estimates, *Deep-Sea Res., Part II, 49*, 1623-1644.

Siegenthaler, U., and T. Wenk (1984), Rapid atmospheric CO_2 variations and ocean circulation, *Nature*, *308*, 624–626.

Son, Y. B., W. D. Gardner, A. V. Mishonov, M. J. Richardson (2009), Multispectral remote-sensing algorithms for particulate organic carbon (POC): The Gulf of Mexico, *Remote Sens. Environ., 113*, 50-61.

Stramska, M., and D. Stramski (2005), Variability of particulate carbon concentration in the north polar Atlantic based on ocean color observations with Sea-viewing Wide Field-of-view Sensor (SeaWiFS), *J. Geophys. Res*., *110*, C10018, doi:10.1029/2004JC002762.

Stramski, D., R. A. Reynolds, M. Babin, S. Kaczmarek, M. R. Lewis, R. Röttgers, A. Sciandra, M. Stramska, M. S. Twardowski, B. A. Franz, and H. Claustre (2008), Relationships between the surface concentration of particulate organic carbon and optical properties in the eastern South Pacific and eastern Atlantic Oceans, *Biogeosciences*, *5*, 171-201.

Stramski, D., R. A. Reynolds, M. Kahru, and B. G. Mitchell (1999), Estimation of particulate organic carbon in the ocean from satellite remote sensing, *Science, 285*, 239-242.

Sullivan, C. W., K. R. Arrigo, C. R. McClain, J. C. Comiso, and J. Firestone (1993), Distributions of phytoplankton blooms in the Southern Ocean, *Science, 262*, 1832-1837.

Sweeney, C., D. A. Hansell, C. A. Carlson, L. A. Codispoti, L. I. Gordon, J. Marra, F. J. Millero, W. O. Smith, and T. Takahashi (2000), Biogeochemical regimes, net community production and carbon export in the Ross Sea, Antarctica, *Deep-Sea Res., Part II, 47*, 3369-3394.

Takahashi, T., S. G. Sutherland, C. Sweeney, A. P. Poisson, N. Metzl, B. Tilbrook, N. R. Bates, R. Wanninkhof, R. A. Feely, C. L. Sabine, J. Olafsson, and Y. Nojiri (2002), Global air-sea CO_2 fluxes based on climatological surface ocean pCO_2 and seasonal biological and temperature effects, *Deep-Sea Res., Part II*, *49*, 1601-1622.

Thuillier, G., M. Herse, P. C. Simon, D. Labs, H. Mandel, D. Gillotay, and T. Foujols (2003), The solar spectral irradiance from 200 to 2400 nm as measured by the SOLSPEC spectrometer from the ATLAS 1-2-3 and EURECA missions, *Sol. Phys*, *214*, 1–22.

Tréquer, P., and G. Jacques (1992), Dynamics of nutrients and phytoplankton, and fluxes of carbon, nitrogen, and silicon in the Antarctic ocean, *Polar Biol*., *12*, 149-162.

Trull, T.W, S. G. Bray, S. J. Manganini, S. Honjo, and R. Francois (2001), Moored sediment trap measurements of carbon export in the Subantarctic and Polar Frontal Zones of the Southern Ocean, south of Australia, *J. Geophys. Res., 106*, 31489-31509.

Volk, T., and M. I. Hoffert (1985), Ocean carbon pumps: Analysis of relative strengths and efficiencies in ocean-driven atmospheric CO_2 changes, in *The Carbon Cycle and Atmospheric CO_2: Natural Variations Archean to Present*, *Geophys. Monogr. Ser.*, vol. 32, edited by E. T. Sundquist and W. S. Broecker, pp. 99–110, AGU, Washington, D. C.